Distribution Agreement

In presenting this thesis or dissertation as a partial fulfillment of the requirements for an advanced degree from Emory University, I hereby grant to Emory University and its agents the non-exclusive license to archive, make accessible, and display my thesis or dissertation in whole or in part in all forms of media, now or hereafter known, including display on the world wide web. I understand that I may select some access restrictions as part of the online submission of this thesis or dissertation. I retain all ownership rights to the copyright of the thesis or dissertation. I also retain the right to use in future works (such as articles or books) all or part of this thesis or dissertation.

Signature:

_____ _____

Duong T. Nguyen Date

# Self-assemblies of electrostatically self-complementary peptides derived from different structural motifs

By

Duong T. Nguyen
Doctor of Philosophy

Chemistry

_____

Dr. Vincent P. Conticello
Advisor

_____

Dr. David Lynn
Committee Member

_____

Dr. Yonggang Ke
Committee Member

Accepted:

_____

Kimberly Jacob Arriola
Dean of the James T. Laney School of Graduate Studies

_____

Date

# Self-assemblies of electrostatically self-complementary peptides derived from different structural motifs

By

Duong T. Nguyen

B.A., Mount Holyoke College, 2018

Advisor: Vincent Conticello, Ph.D.

An abstract of a dissertation submitted to the

Faculty of the James T. Laney School of Graduate Studies of Emory University

In partial fulfillment of the requirements for the degree of

Doctor of Philosophy

In Chemistry

2024

# Self-assemblies of electrostatically self-complementary peptides derived from different structural motifs

By Duong T. Nguyen

## Abstract

Supramolecular self-assembly from peptides is a powerful bottom-up approach for the fabrication of bio-nanomaterials. Peptides are advantageous among the sequence-programmable oligomers because of their sequence-specificity and chemical diversity, hence offering a great opportunity to introduce functional complexity across length-scales. However, it is currently still challenging to achieve controlled fabrication of structurally and dimensionally defined assemblies. This dissertation presents our effort in the fabrication of one- and two-dimensional nanomaterials from the self-assemblies of peptide sequences that are electrostatically self-complementary. The general construct of the peptides consists of two end blocks with oppositely charged residues and a midblock that is neutral. The peptide sequences are designed based on two structural motifs, collagen triple helices and $\beta$-sheets. The collagen-mimetic peptides (CMPs) fold into triple helices, which subsequently self-assemble into two-dimensional crystalline nanosheets via electrostatic interaction. In this work, we utilize CMPs for the construction of multicomponent nanosheets with tunable properties. Even though our study of the $\beta$-strand mimetic peptides (BMPs) is still at its infancy, preliminary results indicate that the charge-complementary sequence design in combination with D-amino acid substitution promote very robust growth of BMPs into one-dimensional nanotubes. Our current findings suggest that the relatively simple design of electrostatically self-complementary peptides works across multiple structural motifs and may present a promising strategy for controlled fabrication of peptide-based nanomaterials.

# Self-assemblies of electrostatically self-complementary peptides derived from different structural motifs

By

Duong T. Nguyen

B.A., Mount Holyoke College, 2018

Advisor: Vincent Conticello, Ph.D.

A dissertation submitted to the

Faculty of the James T. Laney School of Graduate Studies of Emory University

In partial fulfillment of the requirements for the degree of

Doctor of Philosophy

In Chemistry

2024

# Acknowledgements

First I must express my sincere gratitude towards my advisor, Dr. Vince Conticello. Thank you for giving me a chance to start my research in a completely different area and for your patience when my progress is slowed down. I also want to thank my committee members, Dr. David Lynn and Dr. Yonggang Ke for your thought-provoking questions during my annual exams. They were challenging but at the same time very valuable for broadening my research perspectives.

Thank you to every single member of the Conticello Lab over the years that I'm at Emory. Dr. Andrea Merg is definitely my favorite mentor because of his helpful guidance and his enthusiasm for science. Thank you to Dr. Ordy Gnewou, Dr. Jessalyn Miller, and George Cheng for being wonderful colleagues and friends. Thanks to Dr. Spencer Hughes, Dr. Shengyuan Wang, Gavin Touponse, Ayda Gonzalez, Breana Laguera, Andres Gonzalez Socorro, Kenneth Wingate Jr., Abhinaba Das.

For the people outside of our lab that also helped me a lot with my research, thanks to Dr. Alisina Bazrafshan, Dr. Yuesong Hu, Dr. David Dunlap, Dr. Ricardo Guerrero-Ferreira, Dr. Ravi Koripella, Dr. Eric van Genderen, Dr. Xiaobing Zuo.

Thank you to my best friends since high school and college, who are not physically close to me but always emotionally available on a daily basis. Our long-lasting friendship is one of my most valuable assets.

Last but not least, thank you to my family for their unconditional support no matter where I choose to go in life!

# Table of Contents

# Table of Figures

# Chapter 1. A straightforward strategy for fabrication of multicomponent nanosheets from collagen-mimetic peptides

*Acknowledgement:*

*This research used resources of the Advanced Photon Source, a U.S. Department of Energy (DOE) Office of Science user facility operated for the DOE Office of Science by Argonne National Laboratory under Contract No. DE-AC02-06CH11357.*

## 1.1. Introduction

Two-dimensional (2D) nanomaterials possess an ultrathin, planar geometry where the lateral dimensions are one or several orders of magnitude larger than the thickness.[4] A well-known example is graphene, which is a single-layer of graphite with a close-packed conjugated hexagonal carbon lattice.[5] Graphene nanosheets have excellent properties such as large specific area, good mechanical strength, electronic and thermal conductivities, high intrinsic mobility, so it is widely applied in electronic devices, sensors, and other fields.[4, 6] Inspired by the discovery of graphene, numerous 2D nanomaterials, especially soft materials, such as 2D polymers,[7, 8] covalent organic frameworks,[9-11] 2D supramolecular nanostructures,[12, 13] have also been studied. These materials are advantageous because they are light-weight, flexible, and can be fabricated using various methods.[4] These merits offer 2D nanomaterials a wide range of potential applications, such as in energy storage and conversion, as membrane, as catalytic scaffold, as sensing elements, as biotechnological interfaces.[4] Synthetic approaches for fabrication of 2D nanomaterials include both top-down and bottom-up. However, at the nanoscale, bottom-up approaches are more

promising because they are higher-throughput, allow for molecular-level resolution, are cheaper and generate less waste.

Supramolecular self-assembly is a powerful bottom-up approach to synthesize 2D nanomaterials. This strategy employs sequence-programmable oligomers such as block copolymers,[7, 14] peptides,[1-3, 15-20] peptoids,[21-23] nucleic acids[24, 25], and nucleic acid – peptide conjugates[26]. Of these, peptides are advantageous because of their sequence-specificity and chemical diversity, hence offering a great opportunity to introduce functional complexity across length-scales. Research effort in constructing nanosheets has employed the self-assembly of various structural motifs including $\beta$-sheets,[15, 16] collagen-mimetics,[1-3, 17] straight alpha-helices,[18] short synthetic peptides.[19, 20] Even though multiple strategies have been employed, it is currently still challenging to achieve controlled fabrication of structurally and dimensionally defined assemblies.

Our lab has addressed this challenge using collagen-mimetic peptides (CMPs). Natural collagen is the most abundant protein in mammals and represents a great potential biomaterial because of its biocompatibility and ability to mimic the endogenous extracellular matrix.[27] The defining feature of native collagen is the three polyproline-II-type single strands that wrap around each other to form a right-handed triple helix.[28] Its sequence consists of tripeptide repeats Xaa-Yaa-Gly, where Xaa and Yaa are commonly proline and (4R)-hydroxyproline (Hyp), respectively.[28] The triple helix is held together by inter-strand hydrogen bonds between neighboring Gly and Pro.[28] Research on collagen model peptides containing non-natural proline derivatives in place of Pro and Hyp has demonstrated the ability to tune the thermal stability of collagen triple helices in acidic and basic environments.[29, 30]

In our CMP design, the sequences consist of three sequential blocks of positively charged, neutral, and negatively charged triads (Figure 1A). The peptides then fold into triple helices, which can be considered "rigid helical rods." Those serve as building blocks and can self-assemble into 2D lattice via Coulombic attraction between oppositely charged residues of adjacent triple helices. Based on previous synchrotron small-angle/wide-angle X-ray scattering (SAXS/WAXS) and cryogenic transmission electron microscopy (Cryo-TEM) data, we proposed a general model for the nanosheets where the triple helices are packed into a tetragonal lattice and perpendicular to the sheet surface (Figure 1B). Peak (1) and (2) constitute the triple helix packing parameters, where (1) corresponds to distance between (010) planes and (2) marks the distance between (111) planes. The *d*-spacings for peak (1) is approximately $\sqrt{2}$ × peak (2), agreeing with a tetragonal arrangement.

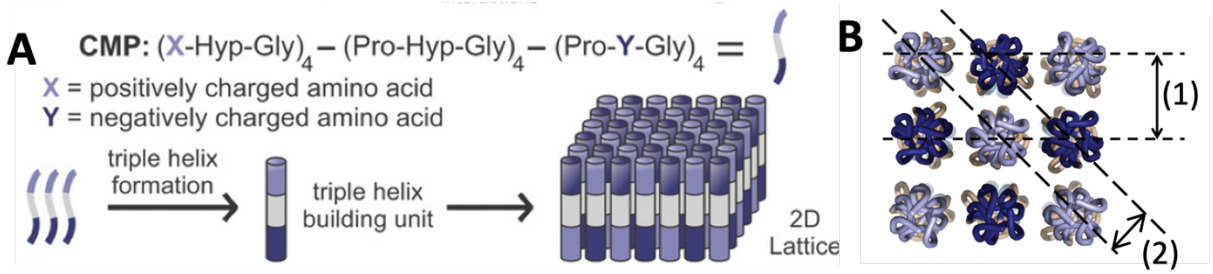


**Figure 1**. (A) Sequences of CMPs comprise positively, neutral, and negatively charged triads. Their folding into triple helices gives rise to triple helix building blocks, which subsequently pack into a 2D lattice with antiparallel orientation due to complementary charge interactions. (B) Model for packing of the collagen triple helices into a tetragonal lattice, with *d*-spacings for peak (1) being approximately $\sqrt{2}$ × peak (2). Adapted from Merg et al.[1]

Our recent projects have been employing (2S, 4S)-4-aminoproline or (2S,4R)-4-aminoproline as the positively charged residue and glutamic acid as the negative one. An example

is the $4S(X)_{444}$ peptide with (2S, 4S)-4-aminoproline residue in the Xaa position. $4S(X)_{444}$ assembles into nanosheets that are single layer and uniform in size (Figure 2).

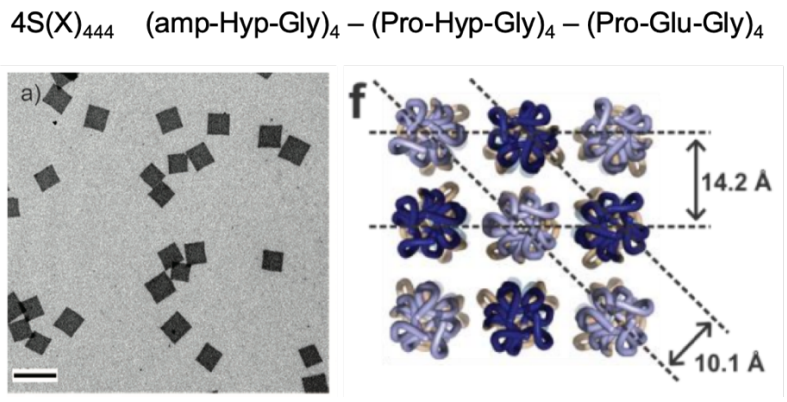


**Figure 2**. Sequence of the $4S(X)_{444}$ peptide (amp = (2S, 4S)-aminoproline) that self-assembles into uniform nanosheets (left, scale bar = 1 $\mu$m) and its assembly model with measured *d*-spacings (right). Adapted from Jiang et al.[2] and Merg et al.[1]

We demonstrated the ability to achieve hierarchical control across length-scales over the formation of nanosheets from 4S(X) peptide series. By varying the number of Pro-Hyp-Gly triads comprising the central block, we were able to tune the resultant nanosheets both at the meso- and nanoscale (Figure 3). Specifically, CMPs with longer neutral block yield nanosheets of smaller lateral dimensions, higher thermal stability, and more contracted lattice.

A

$4S(X)_{434}$ $(amp\text{-}Hyp\text{-}Gly)_4 – (Pro\text{-}Hyp\text{-}Gly)_3 – (Pro\text{-}Glu\text{-}Gly)_4$
$4S(X)_{444}$ $(amp\text{-}Hyp\text{-}Gly)_4 – (Pro\text{-}Hyp\text{-}Gly)_4 – (Pro\text{-}Glu\text{-}Gly)_4$
$4S(X)_{454}$ $(amp\text{-}Hyp\text{-}Gly)_4 – (Pro\text{-}Hyp\text{-}Gly)_5 – (Pro\text{-}Glu\text{-}Gly)_4$
$4R(X)_{464}$ $(amp\text{-}Hyp\text{-}Gly)_4 – (Pro\text{-}Hyp\text{-}Gly)_6 – (Pro\text{-}Glu\text{-}Gly)_4$
$4S(X)_{474}$ $(amp\text{-}Hyp\text{-}Gly)_4 – (Pro\text{-}Hyp\text{-}Gly)_7 – (Pro\text{-}Glu\text{-}Gly)_4$

B

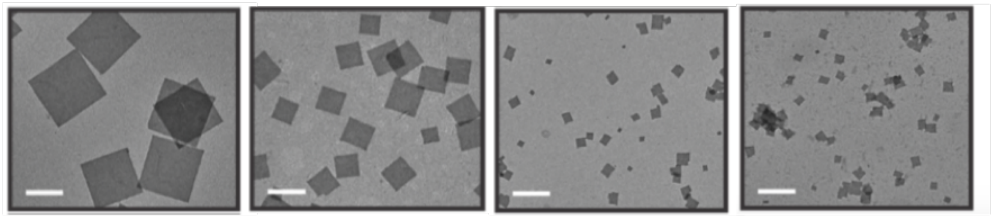

$4S(X)_{444}$ $T_M = 34\ ^oC$ | $4S(X)_{454}$ $T_M = 50\ ^oC$ | $4S(X)_{464}$ $T_M = 44\ ^oC$ | $4S(X)_{474}$ $T_M = 49\ ^oC$

C

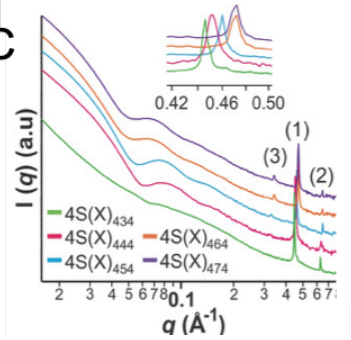


| Peak Number | $4S(X)_{434}$ | $4S(X)_{444}$ | $4S(X)_{454}$ | $4S(X)_{464}$ | $4S(X)_{474}$ |
|---|---|---|---|---|---|
| (1) | 14.1 | 13.9 | 13.7 | 13.4 | 13.3 |
| (2) | 10.0 | 9.9 | 9.7 | 9.7 | 9.7 |
| (3) | – | – | 19.2 | 18.5 | 18.5 |

**Figure 3.** Hierarchical structural control of nanosheets achieved by modifying the number of neutral triads in 4S(X) peptide series. (A) CMP sequences that differ by the number of triads in the central block, (B) TEM images showing nanosheets with decreasing lateral dimensions (scale bars = 500 nm) and their corresponding melting temperatures, and (C) Synchrotron SAXS scattering profiles and corresponding calculated *d*-spacings of Bragg peaks. Adapted from Merg et al.[1]

Moving from single-component assemblies, we also addressed the construction of multicomponent, sectored nanosheets. Pre-formed nanosheets from $4R(X)_{444}$ peptide (with (2S,4R)-4-aminoproline in the Xaa position) was used as templates for the homoepitaxial growth of $4S(X)_{444}$ around them. The resultant nanosheets have distinguishable core and shell regions (Figure 4).

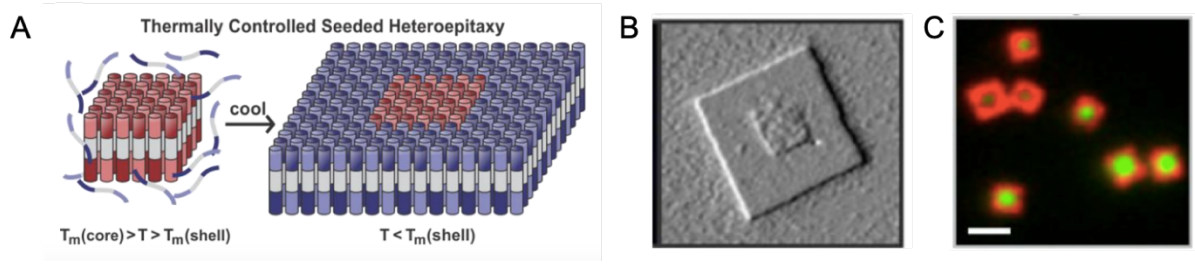


**Figure 4**. Construction of sectored, core-shell assembly. (A) General scheme, (B) AFM amplitude image of a core-shell nanosheet, and (C) fluorescent image of core-shell nanosheets where each sector is functionalized with a different fluorophore. Adapted from Merg et al.[3]

It should be noted that in our core-shell assemblies, each component maintains its own internal structure, even though there are some lattice distortions at the core-shell interface. Consequently, it is not possible to achieve a systematic control over the dimensions and structure of the resultant nanosheets like what was shown with single-component systems. The great advantage of multicomponent nanosheets, however, is that they will allow for possible multifunctionality, where each individual component is functionalized. As a proof-of-concept experiment, we successfully showed with our core-shell structures that each domain could be functionalized with one fluorophore (Figure 4C). Therefore, we are motivated to develop another strategy for the construction of multicomponent nanosheets while also being able to achieve hierarchical control over their formation.

We hypothesize that by mixing two different CMP solutions and annealing their solution mixture, it is possible to construct multicomponent "blended" nanosheets where the two CMPs are homogenously mixed and randomly distributed across the structure. The general scheme is presented in Figure 5. Mixing of CMPs with distinctive characteristics (i.e., peptide sequence length and component, thermodynamic stability, lattice packing parameters) and annealing them together will facilitate random association of the triple-helical building blocks, resulting in mixed

nanosheets with properties such as dimensions, thermal stability, and internal structure that are intermediate between the pure ones. In addition, we expect that varying the mixing ratios between the two CMPs will allow for fine-tuning of the nanosheet properties.

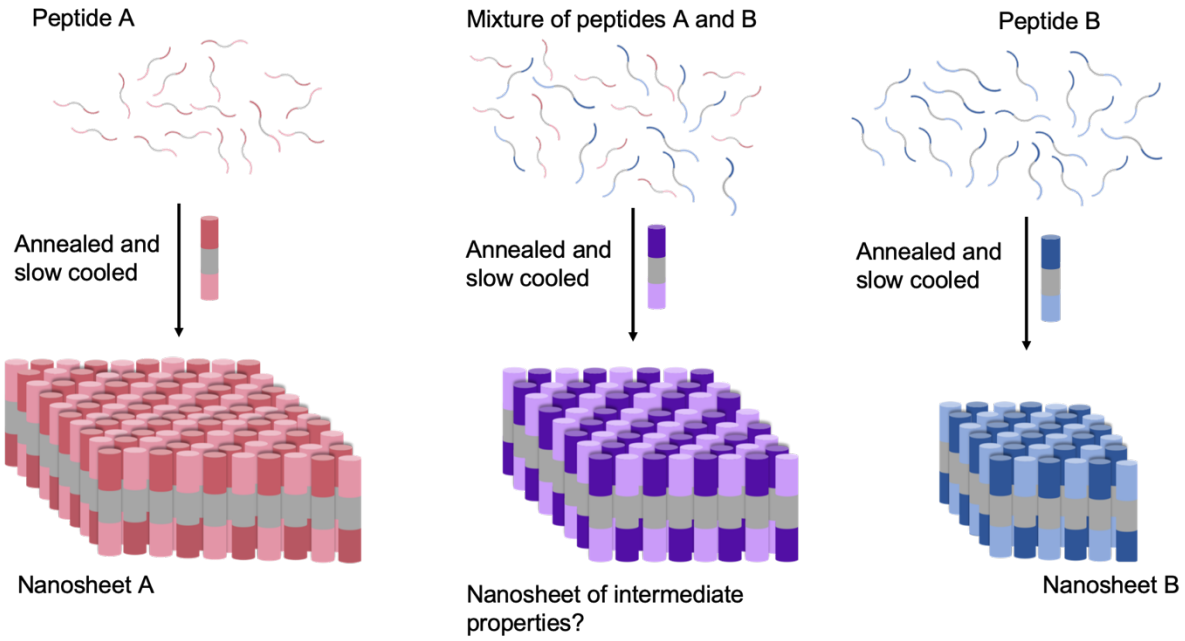


**Figure 5**. General scheme for fabrication of two-component nanosheets. Two different classes of CMPs (A and B) fold into distinct triple helices (A-red cylinder, B-blue cylinder) and consequently pack into nanosheets of different properties. By annealing a solution mixture of A and B, the peptides/triple helices will be able to randomly associate and assemble into nanosheets with properties such as lateral dimensions, thickness, thermal stability, or internal structure that are intermediate between pure nanosheets A and B.

### 1.2. CMP candidates for mixed assemblies

The CMP pairs chosen for mixing should form pure nanosheets that are differentiable in dimensions and thermal stabilities. This will help the characterization process of the mixed assemblies become more straight-forward. In addition, the lattice spacings of those nanosheets should also be considered as we speculate that they will dictate whether the two peptides are compatible for mixing. Even though all CMP nanosheets are expected to share the same underlying tetragonal lattice, a large lattice mismatch may result in crystal defects and have a significant impact on the properties of the resultant nanosheets. The heteroepitaxy of polymers, which is comparable to our core-shell assembly, allows a benchmark limit of 15% lattice mismatch for successful growth.[31] It would be interesting to find out what would be the accepted lattice mismatch for our mixed assemblies.

As a proof-of-principle experiment, four different CMPs have been chosen and their sequences are shown below.

$4S(X)_{535}$ $(amp\text{-}Hyp\text{-}Gly)_5 – (Pro\text{-}Hyp\text{-}Gly)_3 – (Pro\text{-}Glu\text{-}Gly)_5$
$4S(X)_{545}$ $(amp\text{-}Hyp\text{-}Gly)_5 – (Pro\text{-}Hyp\text{-}Gly)_4 – (Pro\text{-}Glu\text{-}Gly)_5$
$4R(X)_{444}$ $(Amp\text{-}Hyp\text{-}Gly)_4 – (Pro\text{-}Hyp\text{-}Gly)_4 – (Pro\text{-}Glu\text{-}Gly)_4$
$4S(Y)_{444}$ $(Pro\text{-}amp\text{-}Gly)_4 – (Pro\text{-}Hyp\text{-}Gly)_4 – (Glu\text{-}Hyp\text{-}Gly)_4$

The peptides vary in the number of triads (3, 4, or 5) and in the identity of the positively charged residue ((2S,4S)-4-aminoproline (amp) or (2S,4R)-4-aminoproline (Amp)). As a result, they assemble into nanosheets that are significantly different in size and thermal stability (Figure 6 and Table 1).

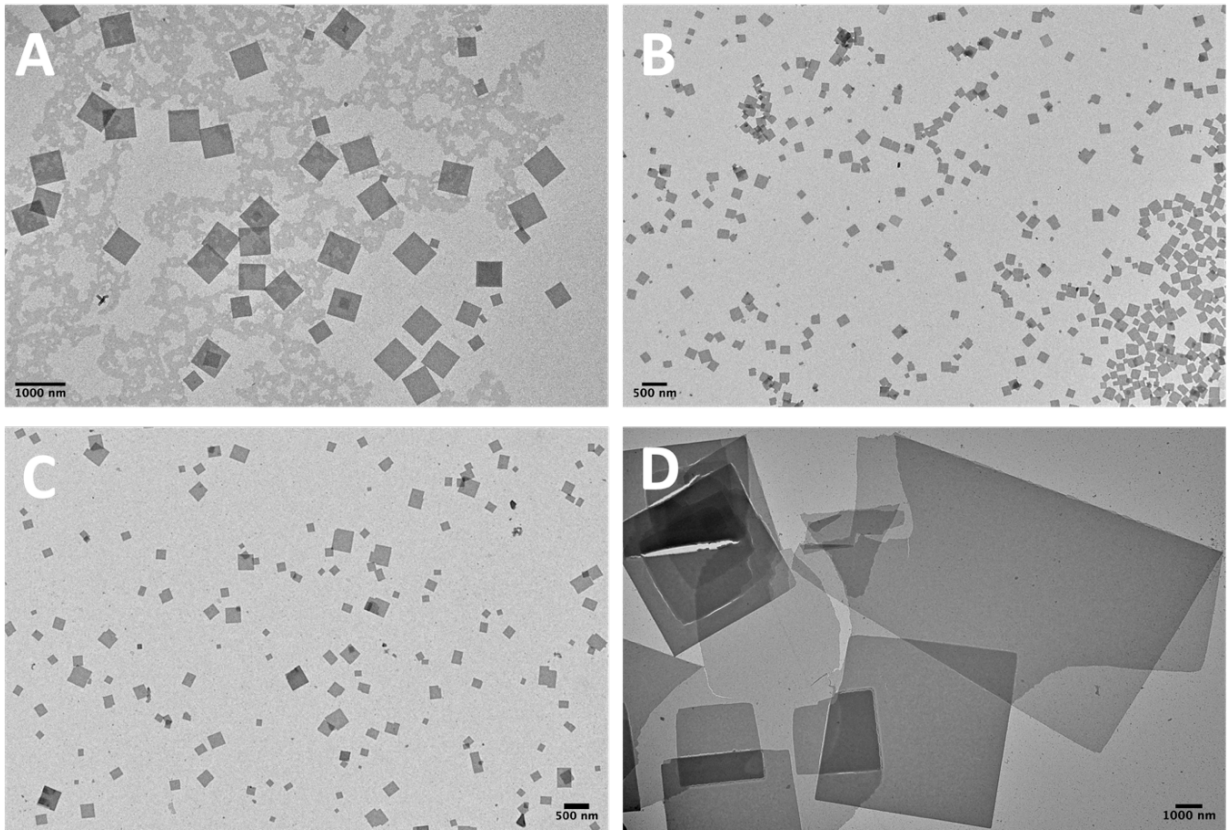


**Figure 6**. Resultant nanosheets from different CMP candidates. (A) $4S(X)_{535}$ (scale bar = 1 $\mu$m), (B) $4S(X)_{545}$ (scale bar = 500 nm), (C) $4R(X)_{444}$ (scale bar = 500 nm), and (D) $4S(Y)_{444}$ (scale bar = 11 $\mu$m).

All CMPs, except $4S(Y)_{444}$, assemble into nanosheets displaying a relatively narrow size distribution (Figure 6). The nanosheets' diagonal lengths ($L_d$) and melting temperatures ($T_m$) are summarized in Table 1. In addition, the *d*-spacings corresponding to the (010) planes (Figure 1B), which are the most prominent peaks in the SAXS profiles, are also presented.

**Table 1.** Properties of CMP candidates

| Peptide name | Diagonal length of nanosheets (nm) | Melting temperature (℃) | *d*-spacing from highest Bragg peak in SAXS profile (Å) |
|---|---|---|---|
| $4S(X)_{535}$ | 697±196 | 37.9 | 14.2 |
| $4S(X)_{545}$ | 154±67 | 31.7 | 14.1 |
| $4R(X)_{444}$ | 222±86 | 54.1 | 13.5 |
| $4S(Y)_{444}$ | Too polydisperse | 64.4 | 15.1 |

For our construction of multicomponent nanosheets, $4S(X)_{535}$ – $4S(X)_{545}$ will be a pair for mixing, and $4R(X)_{444}$ – $4S(Y)_{444}$ are the other pair. The two CMPs in a pair satisfy our requirements for forming pure nanosheets with significant difference in size and thermal stability. In addition, the lattice mismatch between $4S(X)_{535}$ – $4S(X)_{545}$ is less than 1% while between $4R(X)_{444}$ – $4S(Y)_{444}$ is approximately 9%. It would be interesting to discover how differently these two systems would behave.

The assembling conditions for each CMP are presented in table 2. Both pure CMPs in a pair assemble under the same conditions, so their mixture assemblies would follow the same protocol.

**Table 2**. Different pairs of CMPs utilized for fabrication of multicomponent nanosheets and proposed assembling conditions.

| System | CMP A | Assembling conditions of A | CMP B | Assembling conditions of B | Assembling conditions of mixed systems |
|---|---|---|---|---|---|
| 1 | $4S(X)_{535}$ | 4 mg/mL, incubated at 4 ℃ for 2 weeks | $4S(X)_{545}$ | 4 mg/mL, incubated at 4 ℃ for 2 weeks | 4 mg/mL, incubated at 4 ℃ for 2 weeks |
| 2 | $4R(X)_{444}$ | 1 mg/mL, incubated at RT for 1 week | $4S(Y)_{444}$ | 1 mg/mL, incubated at RT for 1 week | 1 mg/mL, incubated at RT for 1 week |

### 1.3. Mixing and characterization of $4S(X)_{535}$ and $4S(X)_{545}$ nanosheets

The two CMPs serve as ideal candidates for our proof-of-principle experiment, as they assemble under the same conditions but $4S(X)_{535}$ forms nanosheets that are significantly larger and have higher melting temperature than $4S(X)_{545}$. Their lattice structures are similar (lattice mismatch is less than 1%), and $4S(X)_{545}$ is only longer by one triad so even when randomly associating the two peptides would still maintain sufficient electrostatic interaction to promote cohesion between triple helices. To assemble the mixed systems, different peptide mixtures with ratios ranging from 90% $4S(X)_{535}$ - 10% $4S(X)_{545}$, down to 75% $4S(X)_{535}$, 50% $4S(X)_{535}$, 25% $4S(X)_{535}$, and 10% $4S(X)_{535}$ were prepared to a final concentration of 4 mg/mL, thermally annealed at 90 ℃ for 15 minutes, slow cooled by 1 ℃/5 minutes, and incubated at 4 ℃ for two weeks prior to characterization.

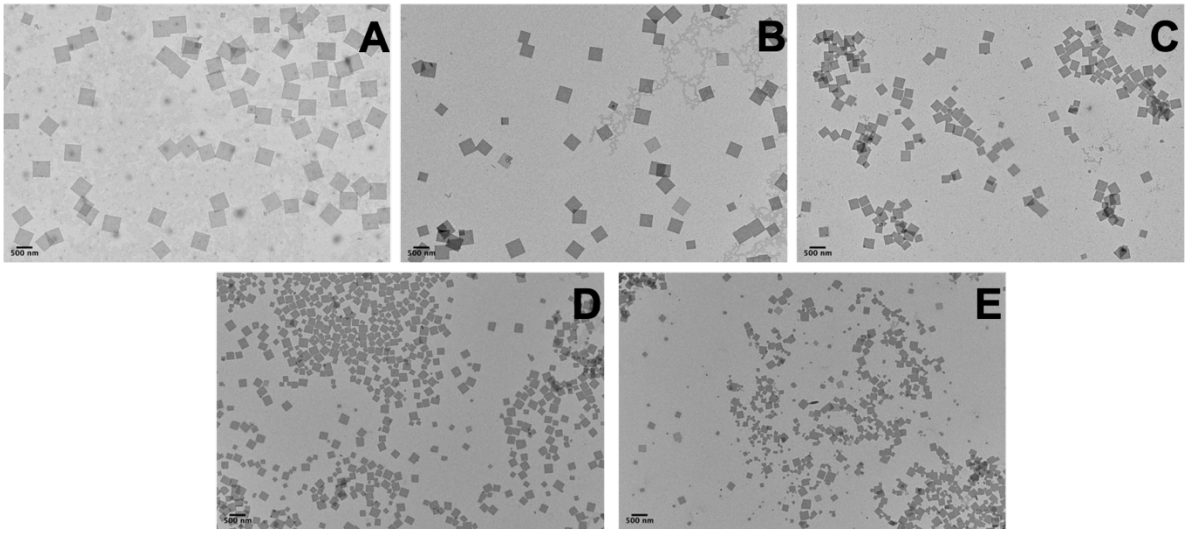


**Figure 7.** Resultant nanosheets from mixing of $4S(X)_{535}$ and $4S(X)_{545}$ peptides (scale bars = 500 nm). (A) 90% $4S(X)_{535}$ - 10% $4S(X)_{545}$, (B) 75% $4S(X)_{535}$ - 25% $4S(X)_{545}$, (C) 50% $4S(X)_{535}$ - 50% $4S(X)_{545}$, (D) 25% $4S(X)_{535}$ - 75% $4S(X)_{545}$, and (E) 10% $4S(X)_{535}$ - 90% $4S(X)_{545}$. Assembled at 4 mg/mL in MOPS buffer (20 mM, pH 7) and incubated for 2 weeks.

Visual inspection of the TEM images reveal that all ratios studied see the formation of nanosheets that are monolayer, monodisperse in size, and smaller in lateral dimensions as lower percentage of $4S(X)_{535}$ is present (Figure 7).

### 1.3.1. Size distribution

Among the mixed assemblies, no nanosheet as large as pure $4S(X)_{535}$ is observed (Figure 7, Table 3). It is also visible that with lower percentage of $4S(X)_{535}$ present, the resultant nanosheets decrease in lateral dimensions. This is confirmed by measuring the diagonal length of the nanosheets (Table 3). The left-shift in the histograms (Figure 8A) also demonstrates this trend. In addition, dynamic light scattering (DLS) was also employed for obtaining size distribution. Even though the Stokes-Einstein relationship is not valid for 2D assemblies, the population of

nanosheets could still be fit to a single curve that is consistent with a uniform size distribution of self-assembled species (Figure 8B). DLS measurements agree with the overall decreasing trend in size of the nanosheets down to 25% $4S(X)_{535}$ - 75% $4S(X)_{545}$. The large numbers obtained for 10% $4S(X)_{535}$ - 90% $4S(X)_{545}$ and 100% $4S(X)_{545}$ are more likely due to too concentrated samples resulting in aggregation of the nanosheets.

**Table 3**. Characterization of $4S(X)_{535}$ – $4S(X)_{545}$ mixed nanosheets

| %$4S(X)_{535}$ : %$4S(X)_{545}$ | Diagonal length from TEM (nm) | Diameter from DLS (nm) | Melting temperature (℃) |
|---|---|---|---|
| 100:0 | $697 \pm 196$ | 335 | 37.9 |
| 90:10 | $616 \pm 159$ | 305 | 37.8 |
| 75:25 | $501 \pm 108$ | 245 | 35.3 |
| 50:50 | $298 \pm 112$ | 183 | 34.7 |
| 25:75 | $240 \pm 77$ | 154 | 33.1 |
| 10:90 | $174 \pm 79$ | 211 | 32.8 |
| 0:100 | $154 \pm 67$ | 186 | 31.7 |

### 1.3.2. Thermal stability

The first derivatives of the melting curves for the mixed assemblies are presented in Figure 8C. All melting curves show a single melting transition, which implies the presence of only one population of nanosheets. This supports the hypothesis that those nanosheets are indeed mixed. The value of each peak corresponding to the melting temperature of the nanosheets is provided in Table 3. The melting points of the mixed nanosheets lie in between those of pure $4S(X)_{535}$ and

$4S(X)_{545}$ ones. In addition, the thermal stability also decreases with decreasing amount of $4S(X)_{535}$ peptides.

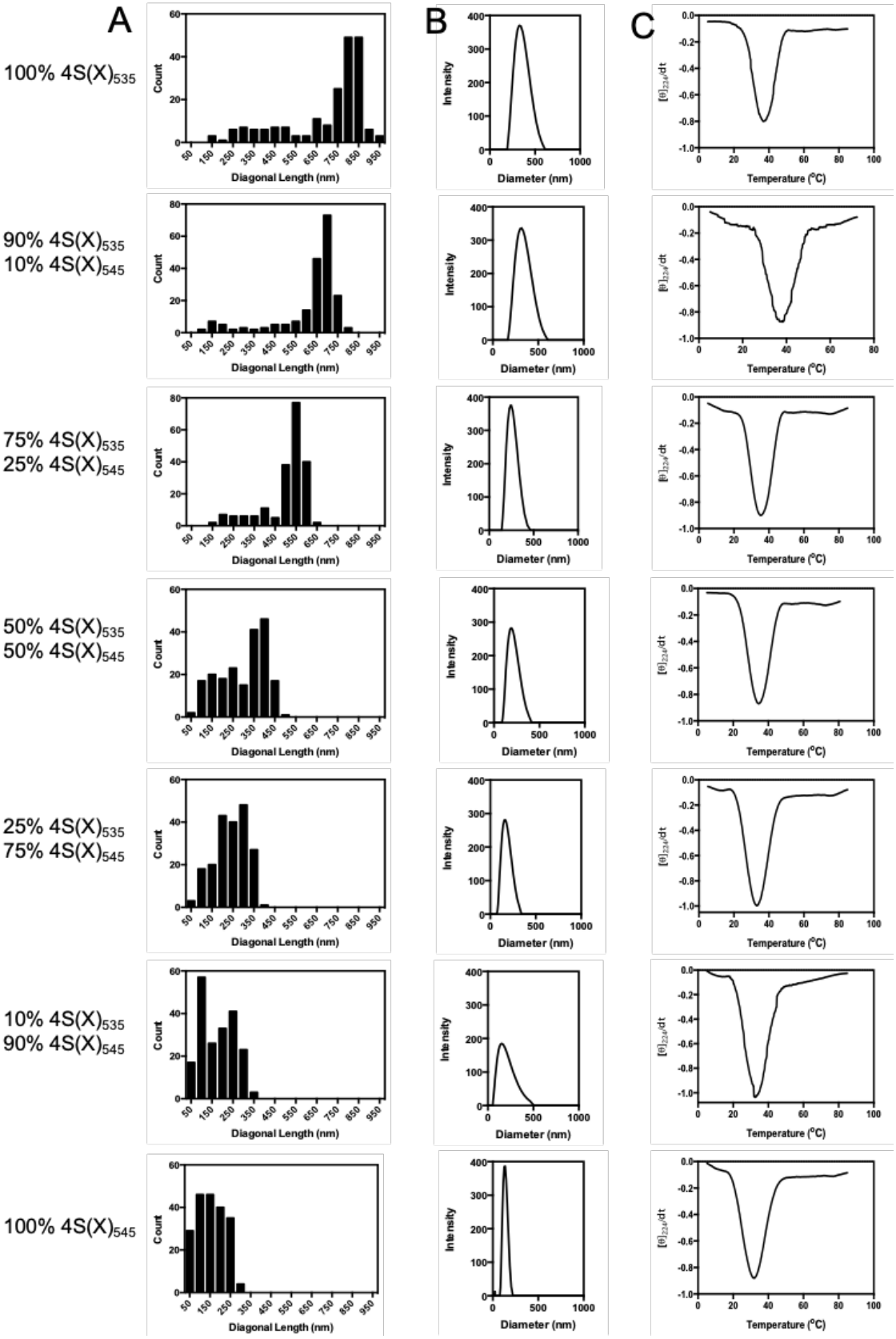
A
B
C
100% 4S(X)535
90% 4S(X)535
10% 4S(X)545
75% 4S(X)535
25% 4S(X)545
50% 4S(X)535
50% 4S(X)545
25% 4S(X)535
75% 4S(X)545
10% 4S(X)535
90% 4S(X)545
100% 4S(X)545
Count
Diagonal Length (nm)
Intensity
Diameter (nm)
[θ]224/dt
Temperature (°C)

**Figure 8.** Characterization of $4S(X)_{535}$ – $4S(X)_{545}$ mixed nanosheets (A) Diagonal length distribution based on TEM (200 counts), (B) DLS spectra, (C) First derivative of the CD signal at 224 nm as a function of temperature.

### 1.3.3. Fluorescent imaging

Previously with the core-shell assemblies, we performed dual-functionalization experiment on the surface of a single nanosheet (Figure 4C) and visualized using fluorescence imaging. In addition to serving as a proof-of-concept experiment for surface functionalization, this fluorescent scheme can also be applied to determine the colocalization of the two CMPs on the same nanosheet.

The general scheme (Figure 9) is that a solution of $4S(X)_{535,}$ $4S(X)_{545}$, N-terminal-modified biotin and azido CMP derivatives (b-$4S(X)_{535}$ and $N_3$-$4S(X)_{545}$) will be annealed altogether to form mixed nanosheets. Subsequently, the nanosheets will be incubated with DBCO-tagged Cy3B and biotin-tagged GFP. We speculate that the peptides indeed mix, and that their triple helices randomly associate across the structure. If that is the case, their resultant nanosheets would have biotin and azido groups evenly distributed on the surface, hence imaging under both green and red emission wavelengths would give overlapping signal. However, in case the triple helix building blocks do not mix but instead forming single-component domains, it would result in sectored nanosheets. Two possible scenarios could be either a core-shell or a “patchy” construct. Consequently, the two fluorophores would be present on separate areas of the nanosheets.

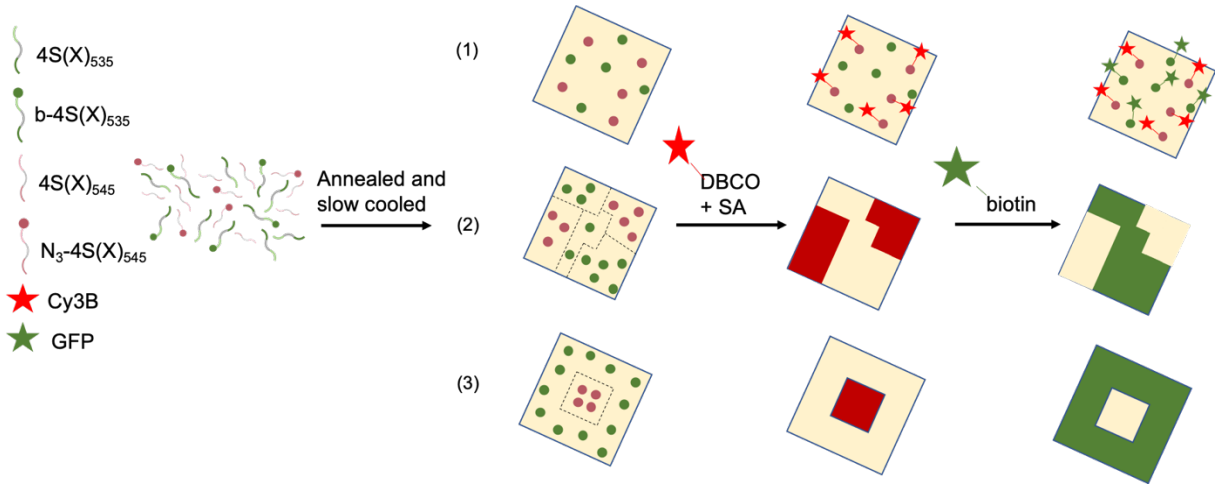


**Figure 9.** Fluorescence imaging experimental scheme and possible outcomes. Scheme detailing the site-specific attachment of DBCO-Cy3B and biotin-GFP on $4S(X)_{535}$ – $4S(X)_{545}$ mixed nanosheets. Possible scenarios for distribution of the fluorophores on the surface include (1) surface with evenly distributed fluorophores, implying homogenous mixing of the two peptides to form a "blended" nanosheet, (2) a sectored nanosheet where the two fluorophores are present on distinct regions of the surface, suggesting a "patchy" assembly with differentiable single-component domains, (3) core-shell pattern, indicating another type of sectored nanosheet.

The limitation of fluorescence imaging, however, is its diffraction limit. Even though the chosen 90% $4S(X)_{535}$ - 10% $4S(X)_{545}$ nanosheets are the biggest among their mixed series, their diagonal length is still only 478 $\pm$ 58 nm on average (Figure 10E). This is barely larger than the diffraction limit and making it impossible to identify the proper square-shaped nanosheets. As expected, only small dots are spotted in fluorescent micrographs (Figure 10A and 10B). Line profiles through those dots give band widths of around 500 nm, which agrees with the size of the nanosheets. Shown in Figure 10C and 10D are the line profiles through some nanosheets in the green channel and their corresponding ones in the red channel. The overlapping of the peaks (Figure 10F) confirms the colocalization of Cy3B and GFP on the same surface, hence implying

mixing of the two CMPs. However, because of the limitation in the image resolution, it is not possible to determine how the fluorophores are distributed on the surface.

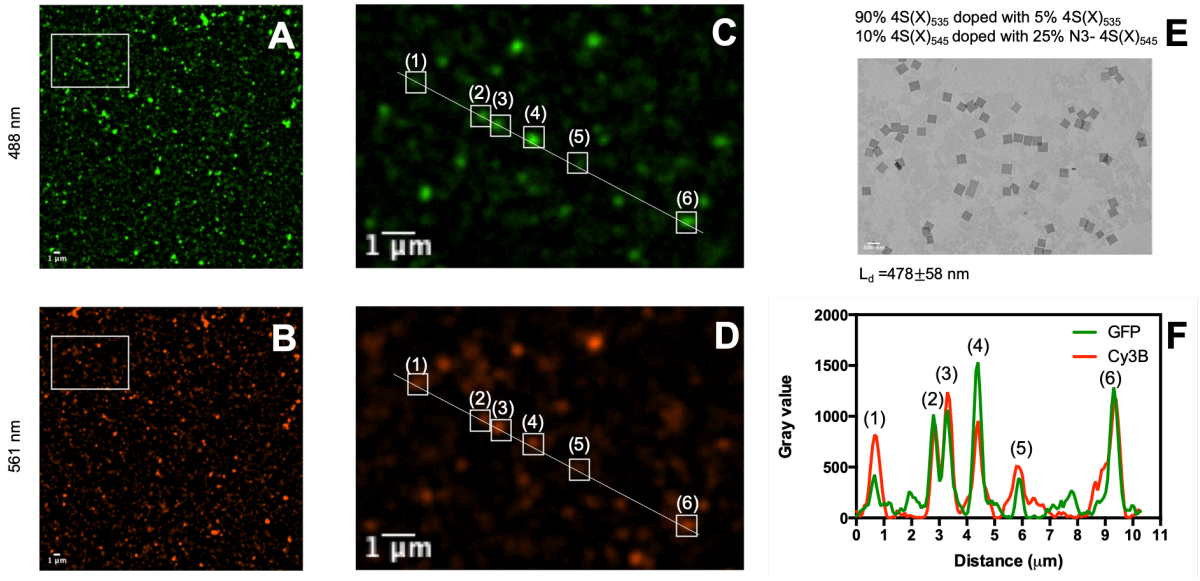


**Figure 10.** Fluorescent experiment on 90% $4S(X)_{535}$ - 10% $4S(X)_{545}$ nanosheets, (A) imaged under green emission wavelength, (B) imaged under red emission wavelength, (C) enlarged image of the boxed section in the green channel and (D) its corresponding section in the red channel, (E) TEM image of the assembly, and (F) graph showing colocalization of GFP and Cy3B signals for the six nanosheets in (C) and (D).

### 1.3.4. Additional thermal denaturation study to prove successful mixing of the two peptides

Another scheme to prove that the nanosheets are actually mixed is to pre-assemble the pure nanosheets, then mix the matured nanosheet solutions together and perform a melt immediately after. This should result in a melting curve with two melting transitions as there are two populations of sheets in the mixture. Subsequently, that mixture solution will be re-annealed. At high temperature, the nanosheets will dissociate into peptide monomers. Those peptides can now freely

associate to form nanosheets. If thermal denaturation study of this new assembly shows only one single melting transition, it is certain that mixing of the CMP nanosheets does happen.

As a proof-of-concept experiment, we only conducted this on the 50% $4S(X)_{535}$ – 50% $4S(X)_{545}$ assembly. Prior to annealing, it is visible that there are two populations of nanosheets in the TEM image (Figure 11A), which is no longer present after annealing (Figure 11B). This is consistent with what we have expected.

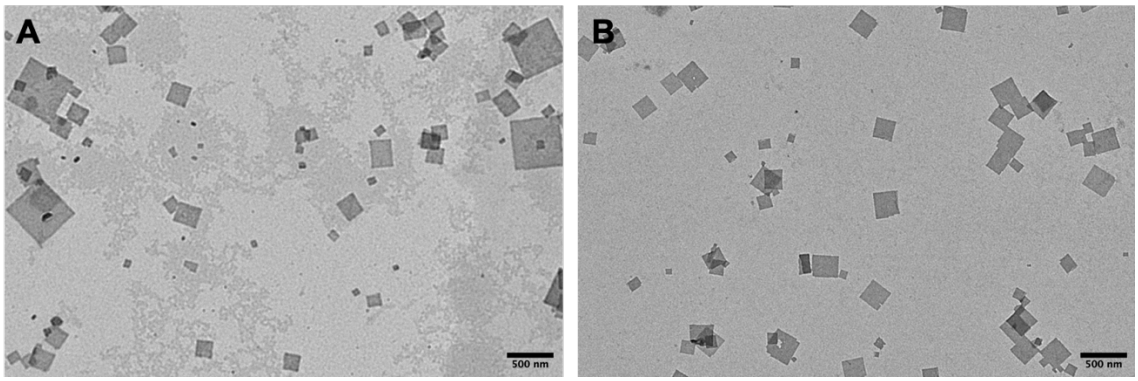


**Figure 11**. TEM images of (A) mixture of matured $4S(X)_{535}$ and $4S(X)_{545}$ nanosheets without subsequent annealing, and (B) resultant nanosheets after mixing $4S(X)_{535}$ and $4S(X)_{545}$ nanosheets in 50:50 ratio and annealing them together (scale bars = 500 nm).

Thermal denaturation study (Figure 12) also agrees with our speculation, where the unannealed sample right after mixing shows two melting transitions, one at 32.1 ℃ (corresponding to $4S(X)_{545}$) and the other at 37.1 ℃ (corresponding to $4S(X)_{535}$). The annealed sample, however, has only one transition at 33.5 ℃.

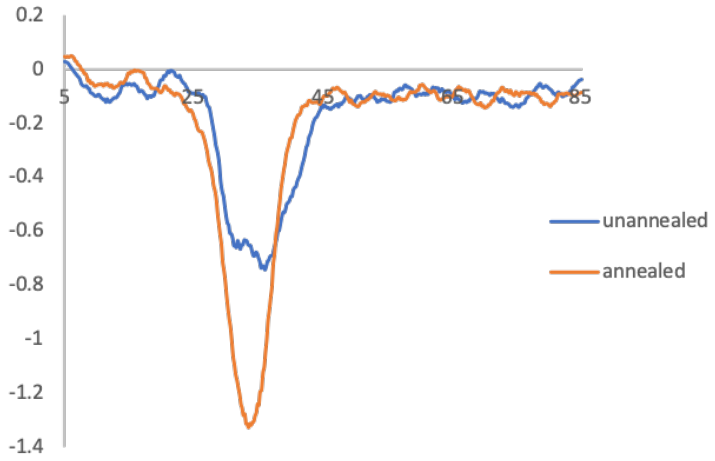


**Figure 12.** First derivatives of the CD signals at 224 nm as a function of temperature.

### 1.3.5. Summary on the mixing of $4S(X)_{535}$ and $4S(X)_{545}$ peptides

The mixing of these two peptides facilitates the formation of mixed nanosheets with intermediate properties. Pure $4S(X)_{545}$ assembles into nanosheets that are smaller than $4S(X)_{535}$ does, so an increasing amount of $4S(X)_{545}$ in the peptide mixture results in decreasing size of the mixed nanosheets. Thermal denaturation study shows a single melting transition for each assembly suggesting the presence of only one population of nanosheets, hence also implying successful mixing. The mixed assemblies possess thermal stability that is intermediate between the two single-component systems. Data from fluorescent imaging experiment indicates the colocalization of the two fluorophores on the same surface, thus reinforcing the argument on formation of mixed nanosheets. However, it remains unclear how the two peptides are distributed in a single nanosheet and whether we create a sectored or a perfectly “blended” structure.

### 1.4. Mixing and characterization of $4R(X)_{444}$ and $4S(Y)_{444}$ nanosheets

The most interesting feature of this system is the quite different lattice spacings between the two peptides, with a lattice mismatch of approximately 9%. Therefore, with this CMP pair, we would be able to see whether such a difference in internal structure would still facilitate the mixing of the two and the tuning of their properties. Since $4R(X)_{444}$ and $4S(Y)_{444}$ assemble under the same set of conditions, the assembling conditions of the mixed system can follow that of the pure components. The mixed assemblies were prepared to a final concentration of 1 mg/mL, thermally annealed at 90 ℃ for 15 minutes, slow cooled by 1 ℃/5 minutes, and incubated at room temperature for one week.

Initially, $4R(X)_{444}$ and $4S(Y)_{444}$ were mixed and assembled at the same ratios as the $4S(X)_{535}$ - $4S(X)_{545}$ system and the assemblies look homogenous until the 50:50 ratio (Figure 13C) However, as the percentage of $4R(X)_{444}$ lowers to 25%, significantly fewer nanosheets and higher level of polydispersity are observed (Figure 13D). The problem worsens at 10% $4R(X)_{444}$ – 90% $4S(Y)_{444}$, as the peptides mostly do not assemble (Figure 13E).

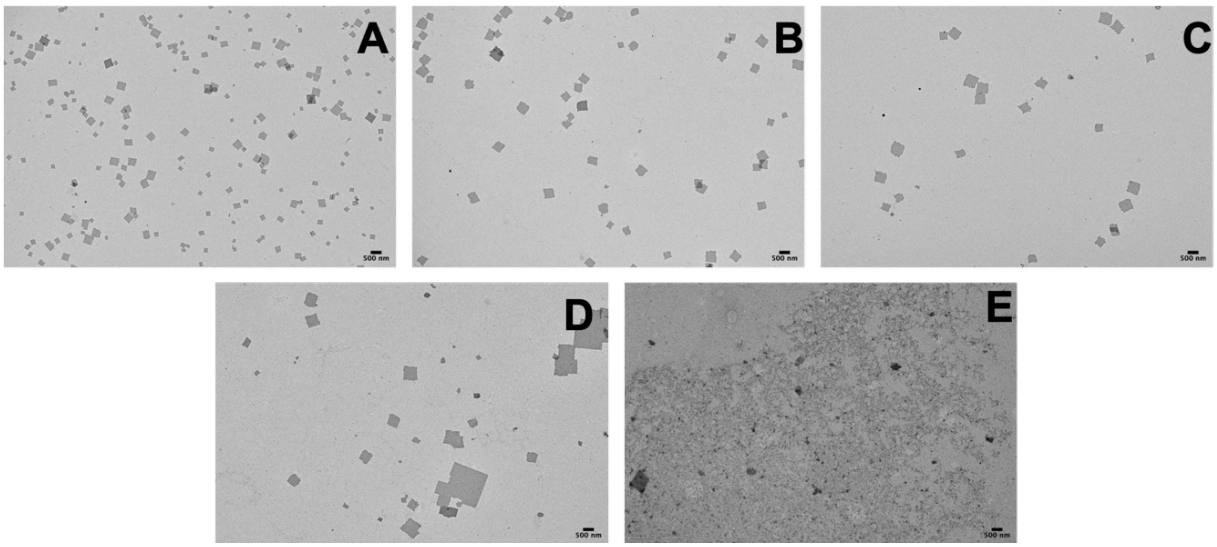

**Figure 13.** Resultant nanosheets from mixing of $4R(X)_{444}$ and $4S(Y)_{444}$ peptides (scale bar = 500 nm). (A) 90% $4R(X)_{444}$ - 10% $4S(Y)_{444}$, (B) 75% $4R(X)_{444}$ - 25% $4S(Y)_{444}$, (C) 50% $4R(X)_{444}$ - 50% $4S(Y)_{444}$, (D) 25% $4R(X)_{444}$ - 75% $4S(Y)_{444}$, and (E) 10% $4R(X)_{444}$ - 90% $4S(Y)_{444}$. Assembled at 1 mg/mL in MOPS buffer (20 mM, pH 7) and incubated at RT for a week.

Additional experiments on varying the ratios of the two peptides identified 40% $4R(X)_{444}$ – 60% $4S(Y)_{444}$ as a threshold concentration in which the nanosheet population remained nearly homogenous in lateral dimensions. Therefore, subsequent characterization was done only for mixed assemblies ranging from 90% $4R(X)_{444}$ down to 40% $4R(X)_{444}$ (Figure 14).

As $4S(Y)_{444}$ nanosheets are significantly larger than $4R(X)_{444}$ ones, increasing the percentage of $4S(Y)_{444}$ when mixing results in formation of larger nanosheets, which are noticeable by visual examination of TEM images (Figure 14). In addition, as more $4S(Y)_{444}$ is doped in, the edges of the nanosheets become more jagged. This could be a consequence of incompatible lattice packing between $4R(X)_{444}$ and $4S(Y)_{444}$.

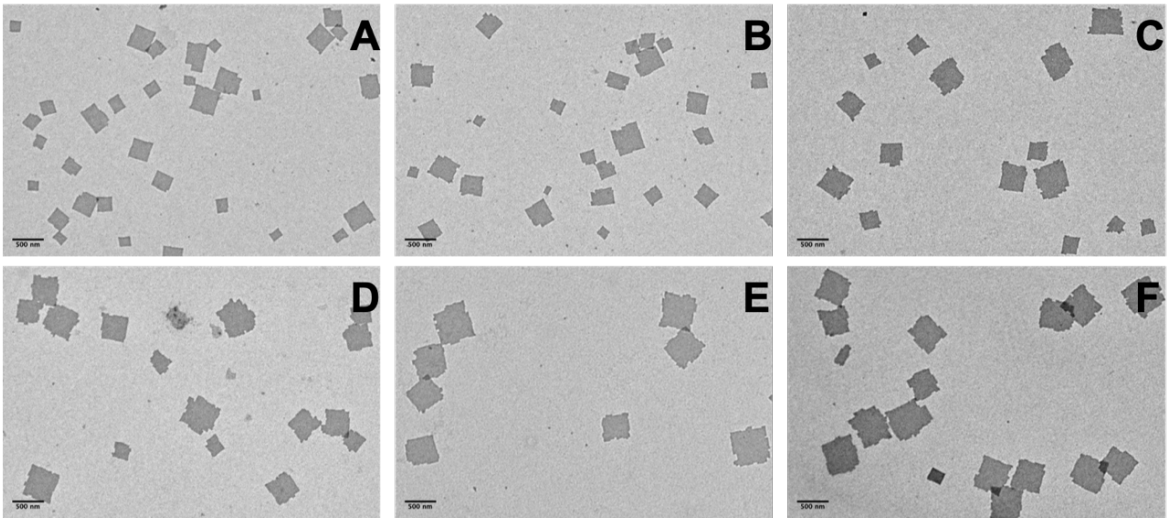


**Figure 14.** Resultant nanosheets from mixing of $4R(X)_{444}$ and $4S(Y)_{444}$ peptides (scale bar = 500 nm). (A) 90% $4R(X)_{444}$ - 10% $4S(Y)_{444}$, (B) 80% $4R(X)_{444}$ - 20% $4S(Y)_{444}$, (C) 70% $4R(X)_{444}$ -

30% 4S(Y)$_{444}$, (D) 60% 4R(X)$_{444}$ - 40% 4S(Y)$_{444}$, (E) 50% 4R(X)$_{444}$ - 50% 4S(Y)$_{444}$, and (F) 40% 4R(X)$_{444}$ - 60% 4S(Y)$_{444}$. Assembled at 1 mg/mL in MOPS buffer (20 mM, pH 7) and incubated at RT for a week.

### 1.4.1. Size distribution

As 4S(Y)$_{444}$ nanosheets are much larger than 4R(X)$_{444}$, when the percentage of 4S(Y)$_{444}$ peptide increases, the averaged diagonal length of the resultant nanosheets also increases (Figure 15 and Table 4). DLS measurements also help to confirm this change in size.

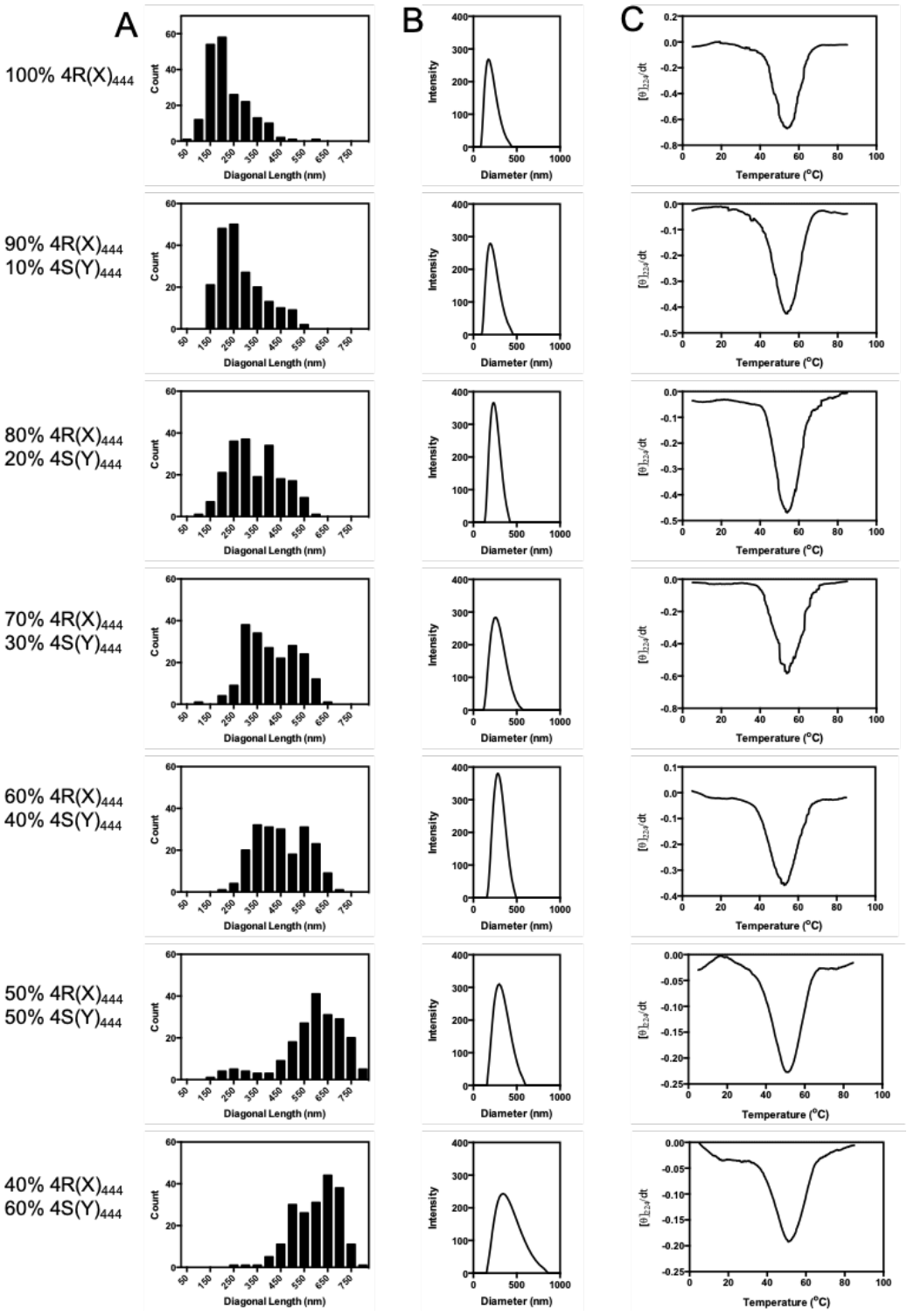
A
B
C
100% 4R(X)444
90% 4R(X)444
10% 4S(Y)444
80% 4R(X)444
20% 4S(Y)444
70% 4R(X)444
30% 4S(Y)444
60% 4R(X)444
40% 4S(Y)444
50% 4R(X)444
50% 4S(Y)444
40% 4R(X)444
60% 4S(Y)444
Count
Diagonal Length (nm)
Intensity
Diameter (nm)
[θ]222/dt
Temperature (°C)

**Figure 15.** Characterization of $4R(X)_{444}$ – $4S(Y)_{44}$ mixed nanosheets (A) Diagonal length distribution based on TEM (200 counts), (B) DLS spectra, (C) First derivative of the CD signal at 224 nm as a function of temperature.

### 1.4.2. Thermal stability

The first derivative of each circular dichroism (CD) melting curve shows only one melting transition (Figure 15C), again suggesting a single population of nanosheets. Interestingly, the melting temperatures of those mixed assemblies are lower than both pure $4R(X)_{444}$ or $4S(Y)_{444}$ nanosheets (Table 4). This destabilizing effect can be attributed to incompatible lattice packing between $4R(X)_{444}$ and $4S(Y)_{444}$ peptides. Their large lattice mismatch leads to the formation of more defective, and hence less thermally stable crystals.

**Table 4**. Characterization of $4R(X)_{444}$ – $4S(Y)_{444}$ mixed nanosheets

| %$4R(X)_{444}$ : %$4S(Y)_{444}$ | Diagonal length from TEM (nm) | Diameter from DLS (nm) | Melting temperature (℃) |
|---|---|---|---|
| 100:0 | $222 \pm 86$ | 180 | 54.1 |
| 90:10 | $277 \pm 95$ | 199 | 54.1 |
| 80:20 | $339 \pm 109$ | 228 | 53.9 |
| 70:30 | $411 \pm 106$ | 247 | 53.7 |
| 60:40 | $455 \pm 108$ | 272 | 52.9 |
| 50:50 | $588 \pm 134$ | 294 | 51.7 |
| 40:60 | $601 \pm 96$ | 341 | 51.3 |
| 0:100 | N/A | N/A | 64.4 |

### 1.4.3. Atomic force microscopy (AFM) height measurement

Because these $4R(X)_{444}$ - $4S(Y)_{444}$ nanosheets are also very small for fluorescence imaging, we decided on another strategy utilizing AFM to examine whether the nanosheets are multicomponent. $4R(X)_{444}$ and $4S(Y)_{444}$ are theoretically the same in length, so to differentiate them we need to employ streptavidin addition to raise the height of one peptide component. Specifically, 5% of biotinylated $4R(X)_{444}$ was doped into the 70% $4R(X)_{444}$ – 30% $4S(Y)_{444}$ mixture prior to annealing. For the AFM measurements, two samples were prepared, one without streptavidin addition (control) and the other with streptavidin. The region where streptavidin is present should be approximately 4 nm taller.

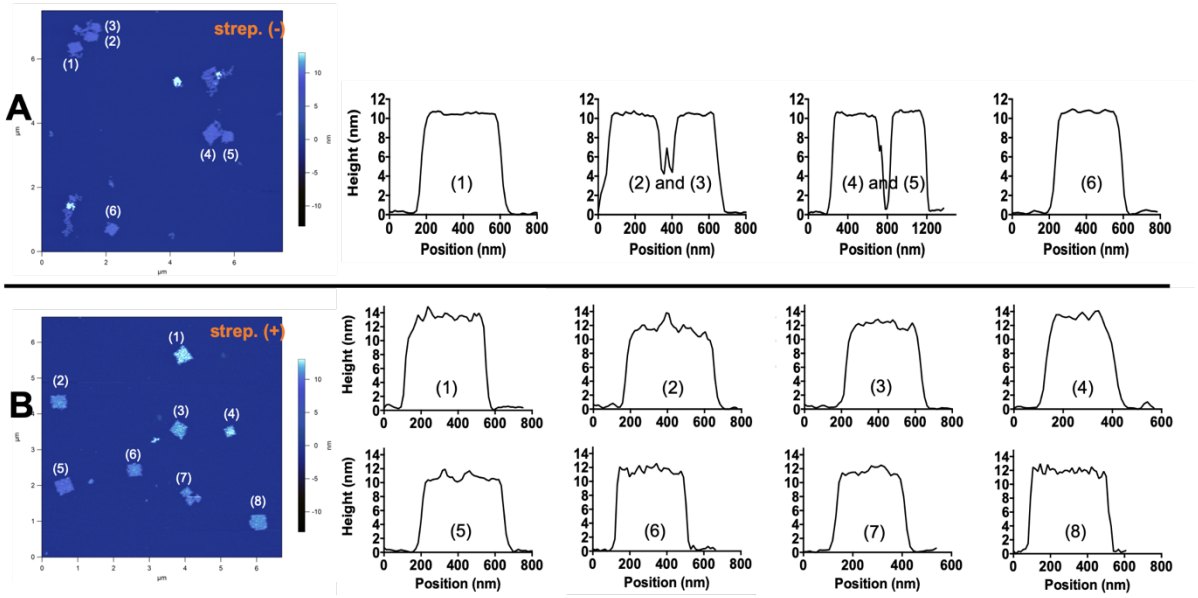


**Figure 16.** AFM analysis on 70% 4R(X)$_{444}$ – 30% 4S(Y)$_{444}$ resultant nanosheets. (A) control sample without streptavidin and height profiles of six nanosheets present, and (B) sample with streptavidin addition and height profiles of eight nanosheets present.

Nanosheets in the control sample have smooth surfaces (Figure 16A). Their heights are all approximately 10 nm, which agrees with the theoretical thickness of 10.3 nm for monolayer nanosheets (0.286 nm rise/residue for collagen triple helices).[32]

In the sample with streptavidin addition, the nanosheets are higher overall (Figure 16B). The height profiles indicate that their surface is bumpier, with peak heights ranging from approximately 12 to 14 nm. In general, thickness of the nanosheets does increase with addition of streptavidin, implying that biotinylated peptides are present on all of those assemblies, hence suggesting that they are multicomponent.

### 1.4.4. SAXS/WAXS scattering profiles

As mentioned earlier, $4R(X)_{444}$ and $4S(Y)_{444}$ have different lattice spacings, so a SAXS/WAXS experiment on the mixed assemblies would give more insight into their underlying structure. Samples were prepared at 4 mg/mL in MOPS buffer (20 mM, pH 7). Shown in Figure 15A are the scattering profiles for the mixed nanosheets along with the pure ones. The presence of the Bragg diffraction peaks in the wide-angle region of the curves dictate a high degree of crystallinity within the assemblies. The peaks labelled (1) and (1') are the highest peaks for $4R(X)_{444}$ and $4S(Y)_{444}$, respectively, and they correspond to the (010) plane distance in the proposed model (Figure 17B). As the percentage of $4R(X)_{444}$ lowers, peak (1) broadens and very slightly shifts to the left (Figure 17C). The (1') peak representing $4S(Y)_{444}$ starts to emerge at 70% $4R(X)_{444}$ – 30% $4S(Y)_{444}$ and becomes more noticeable as the amount of $4S(Y)_{444}$ increases. The *d*-spacings calculated from those peaks of the mixed assemblies (Table 5) are the same as pure ones. This indicates two possibilities, either there is no mixing, or in a single nanosheet there are different single-component domains.

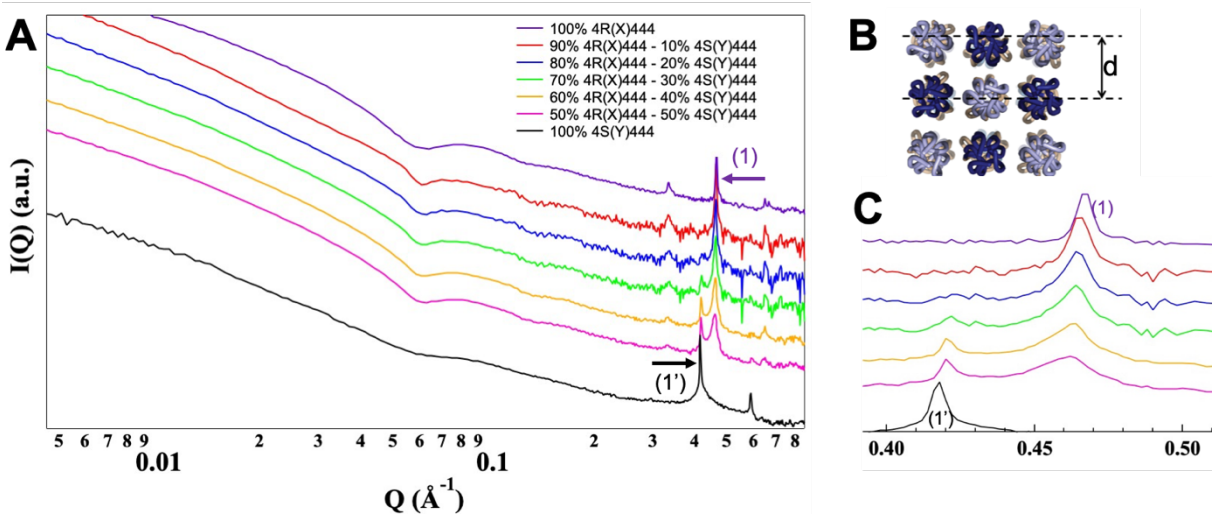

**Figure 17.** Synchrotron SAXS/WAXS analysis on $4R(X)_{444}$ – $4S(Y)_{444}$ system. (A) Scattering profiles, (B) (010) plane distance in the proposed model that correspond to the labelled (1) and (1') peaks, and (C) enlarged diffraction peaks (1) and (1').

**Table 5.** Calculated *d*-spacings of Bragg peaks (1) and (1') from SAXS

| **%$4R(X)_{444}$ : % $4S(Y)_{444}$** | ***d*-spacing from peak 1 (Å)** | ***d*-spacing from peak 1' (Å)** |
|---|---|---|
| 100:0 | 13.4 | -- |
| 90:10 | 13.5 | -- |
| 80:20 | 13.5 | -- |
| 70:30 | 13.5 | 14.9 |
| 60:40 | 13.5 | 15.0 |
| 50:50 | 13.6 | 15.0 |
| 0:100 | -- | 15.0 |

One point that makes this result questionable is the fact that we used more concentrated samples for SAXS experiment (4 mg/mL), whereas for all other experiments the samples were only prepared at 1 mg/mL. At the concentration of 1 mg/mL, TEM samples show an increasing trend in size (Figure 14), which is not observed for 4 mg/mL samples (Figure 18). The larger, stacked nanosheets (Figure 18) are commonly observed for $4R(X)_{444}$ when assembled at concentrations higher than 1 mg/mL, so it is possible that the concentration of 4 mg/mL is too high that it favors the formation of single component nanosheets. Additionally, nanosheets at 1mg/mL have more jagged edges (Figure 19), while at 4 mg/mL there are also nanosheets with smooth,

well-defined edges that resemble pure systems (Figure 6E, F). The melting curves of the 70% 4R(X)$_{444}$ – 30% 4S(Y)$_{444}$ assembly at 4 mg/mL (Figure 19), for example, has a shoulder which is not detected with 1 mg/mL sample. All together this indicates that 4 mg/mL and 1 mg/mL samples are incomparable.

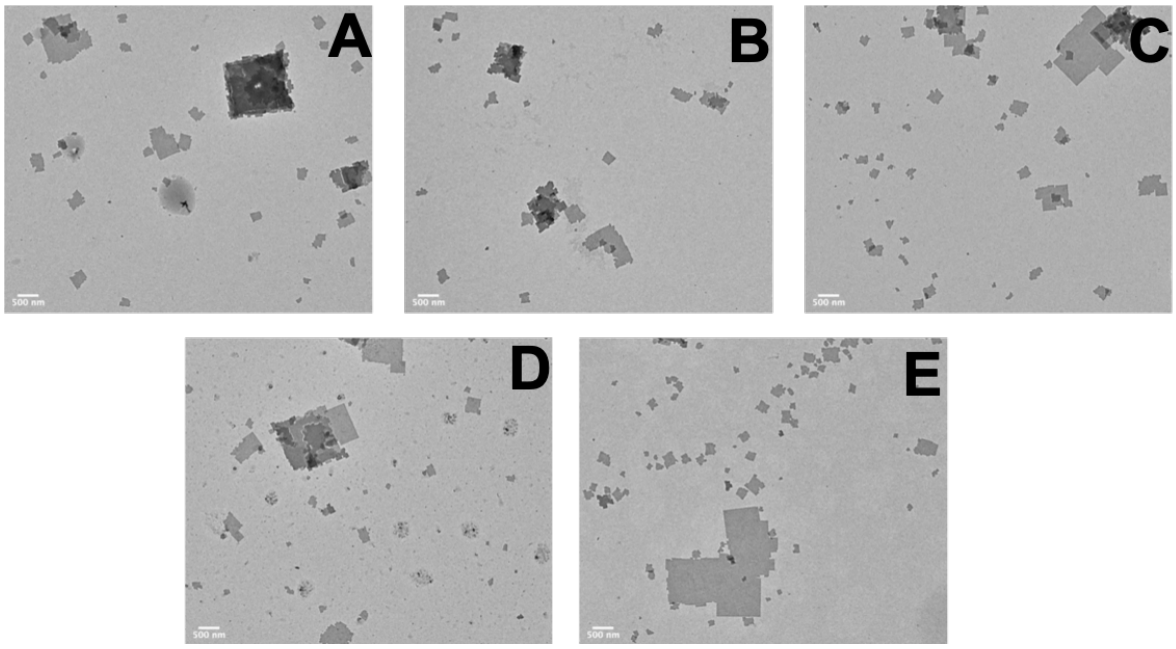


**Figure 18.** Resultant nanosheets from mixing of 4R(X)$_{444}$ and 4S(Y)$_{444}$ peptides at 4 mg/mL (scale bars = 500 nm). (A) 90% 4R(X)$_{444}$ - 10% 4S(Y)$_{444}$, (B) 80% 4R(X)$_{444}$ - 20% 4S(Y)$_{444}$, (C) 70% 4R(X)$_{444}$ - 30% 4S(Y)$_{444}$, (D) 60% 4R(X)$_{444}$ - 40% 4S(Y)$_{444}$, and (E) 50% 4R(X)$_{444}$ - 50% 4S(Y)$_{444}$.

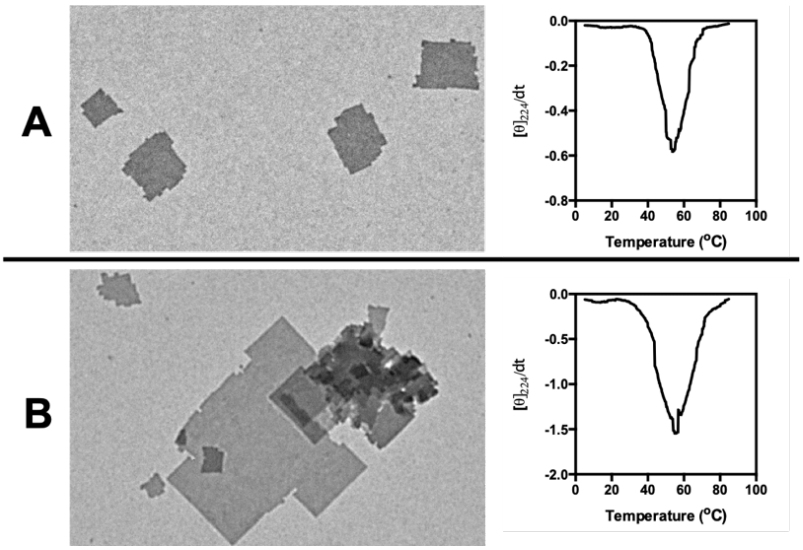


**Figure 19**. TEM images and melting curves of resultant nanosheets from 70% 4R(X)$_{444}$ - 30% 4S(Y)$_{444}$ assembled at (A) 1 mg/mL, and (B) 4 mg/mL.

### 1.4.5. Summary on the mixing of 4R(X)$_{444}$ and 4S(Y)$_{444}$ peptides

Since 4S(Y)$_{444}$ forms larger pure nanosheets than 4R(X)$_{444}$, the nanosheets from their mixed assemblies appear larger in size with higher percentage of 4S(Y)$_{444}$ in presence. Similar to the 4S(X)$_{535}$ – 4S(X)$_{545}$ series, only a single melting transition is observed for each mixed assembly. However, it is interesting that their melting temperatures are lower than those of pure 4R(X)$_{444}$ and 4S(Y)$_{444}$ nanosheets, possibly due to lattice mismatch leading to less stable packing. Results from AFM measurements also provide evidence that there are two different types of CMPs on the same surface. The presence of both 4R(X)$_{444}$ and 4S(Y)$_{444}$ peaks in SAXS scattering profiles suggests two possibilities, either there is no mixing, or in a nanosheet there are separate single-component domains. However, the data from SAXS/WAXS experiment is still questionable due to the assembling concentration that is different from that of all other experiments.

## 1.5. Conclusion

In conclusion, our results from TEM, DLS, CD thermal denaturation, fluorescence imaging, and AFM all support the hypothesis that it is possible to construct multicomponent nanosheets by co-annealing a mixture of different peptide components. However, the lattice mismatch between CMPs should be taken into consideration, as it can result in incompatible packing. $4R(X)_{444}$ and $4S(Y)_{444}$ have a lattice mismatch of approximately 9% and their mixing does not happen after the amount of $4S(Y)_{444}$ peptide reaches a certain point. This implies that our scheme for construction of multicomponent nanosheets may have a lower tolerance for lattice mismatch as compared to the core-shell nanosheets, which employ a heteroepitaxial growth scheme.

In addition to the successful formation of mixed nanosheets with intermediate properties, it is also possible to fine-tune the lateral dimensions and thermal stability of the resultant assemblies by varying the mixing ratios. Our eventual goal is to construct multicomponent "blended" nanosheets with tunable properties. So far, we have been able to accomplish multicomponent and tunability. However, it is still ambiguous whether the two CMPs are randomly distributed in a single nanosheet to form a so-called "blended" structure. In the next chapter, we will continue to address this question on the study of another mixed system, $4S(X)_{444}$ – $4S(X)_{454}$.

## 1.6. Experimental methods

### Peptide synthesis and purification

Peptides were prepared using microwave-assisted synthesis on a CEM Liberty Blue automated microwave peptide synthesizer and Fmoc-Gly-HMP-Tentagel resin. Standard Fmoc protection chemistry was employed with coupling cycles based on DIC/Oxyma-mediated activation protocols and based-induced deprotection (20% piperidine in DMF) of the Fmoc group. For the biotinylated and azido-modified peptides, biotin-PEG2-acid and azido-PEG5-acid were used to cap the N-terminus of the peptide while it was stilled attached to the resin (no final deprotection step). After coupling, the DMF/resin mixture was filtered and rinsed with acetone and then air-dried. The crude peptides were cleaved for 3 hours with a cleavage solution consisting of 92.5% TFA/ 2.5% $H_2O$/ 2.5% DODT/ 2.5% TIS (TFA = trifluoroacetic acid, DODT = 3,6-Dioxa-1,8-octane-dithiol, TIS = Triisopropylsilane). After filtration, the crude peptide product in TFA was precipitated with cold ethanol and centrifuged at 4 ℃. The supernatants were discarded, and the pellets were dried under vacuum overnight.

Crude peptides were purified using a Shimadzu LC-20AP reverse-phase high-performance liquid chromatography (HPLC) instrument equipped with a preparative scale C18 column. Peptides were eluted with a linear gradient of water-acetonitrile with 0.1% TFA. The target fractions were collected and lyophilized. The lyophilized peptide was repurified via HPLC under the same protocol described above and lyophilized. Doubly pure peptides were dialyzed against HPLC-grade $H_2O$ to remove residual TFA (MWCO = 2000 Da). The resulting peptide solutions were lyophilized and stored at -30 ℃.

**Nanosheet assembly experiment**

Annealing experiments were conducted using a BioRad T-100 thermal cycler. The annealing protocol consisted of heating peptide solutions to 90 ℃ for 15 min, followed by slow cooling to either 25 or 4 ℃ (1 ℃/5 min rate). To assemble the nanosheets, each pure peptide was dissolved in 20 mM 3-(N-morpholino)propanesulfonic acid (MOPS) buffer (pH 7.0) to a final concentration of 4 mg/mL($4S(X)_{535}$ – $4S(X)_{545}$ series), or 1 mg/mL ($4R(X)_{444}$ – $4S(Y)_{444}$ series). Single component nanosheets were assembled by annealing each pure peptide solution separately. The mixed assemblies were conducted by mixing the two peptide solutions in designated volume ratios such that the final mixture concentration remained the same.

**Transmission electron microscopy**

TEM specimens were prepared by briefly mixing 2.5 $\mu$L of peptide nanosheet solution with 2.5 $\mu$L of aqueous uranyl acetate stain solution (1%) directly on a 200-mesh carbon coated copper grid from Electron Microscopy Services. After 30 s, the excess liquid was wicked away and the grids were air-dried. Electron micrographs were recorded on a Hitachi HT-7700 TEM with a tungsten filament and AMT CCD camera at an accelerating voltage of 80 kV.

**Circular dichroism spectropolarimetry**

CD measurements were conducted on a Jasco-1500 CD spectropolarimeter. These spectra were recorded and averaged from 260 to 190 nm at a scanning rate of 100 nm/min and a bandwidth of 2 nm. CD melting experiments were conducted with a 0.1 mm path length cuvette, in the temperature range from 5 to 85 ℃ at a heating rate of 20 ℃/h. The intensity of the CD signal at 224 nm was monitored as a function of temperature.

**Dynamic light scattering**

DLS data were collected with a NanoPlus DLS nano particle size analyzer instrument. Three DLS measurements were obtained and averaged on aqueous solutions of CMP nanosheets at 20 ℃.

**Atomic force microscopy**

AFM images were collected with an Asylum MFP-3D atomic force microscope using tapping mode. Images were obtained using ultrasharp AFM tips with a force constant of 5 N/m and a resonance frequency of 150 kHz (Budget Sensors, SHR-150). Images were collected at a scanning rate of 1 Hz. Samples were prepared by drop-casting 15 $\mu$L of peptide nanosheet solution onto freshly cleaved mica. After 5 min, the solution was wicked away and washed once with 30 $\mu$L of HPLC-grade $H_2O$.

**Fluorescence labelling of the nanosheets**

Peptide mixture was prepared from 85.5% $4S(X)_{535}$/ 4.5% b-$4S(X)_{535}$/ 7.5% $4S(X)_{545}$/2.5 % $N_3$-$4S(X)_{545}$. The sample was then annealed and incubated for two weeks at 4 ℃. Subsequently, Cy3B-DBCO (0.5 $\mu$L, 1 mg/mL solution in water) and streptavidin (1 $\mu$L, 1 mg/mL solution in water) were added to a 20 $\mu$L solution of nanosheets. The mixture was incubated for 1 h at room temperature in the dark and then biotin-GFP (1 $\mu$L, 1 mg/mL) was added. The solution was placed in the refrigerator overnight (4 ℃). The next day, the solution was centrifuged at 3000 g for 10 min. The supernatant was removed and replaced with fresh 20 mM MOPS buffer (pH 7.0), and the sample was vortex mixed.

**Fluorescence optical microscopy**

The Nikon Eclipse Ti microscope was equipped with an Intensilight epifluorescence source, a CFI Apo 100X NA 1.49 objective, and a TIRF launcher with three laser lines: 488 nm (10 mW), 561 nm (50 mW), and 638 nm (20 mW). All reported experiments were performed using the Quad Cube (cat. #97327) and TRITC (cat. # 96321) filter cube set supplied by Chroma.

Experiments were conducted using no. 1.5 glass slides (25 x 75 mm) that were cleaned by sonication in Milli-Q (18.2 MΩ/cm) water for 15 min, followed by a second sonication in 200 proof ethanol for 15 min, and then dried under a stream of $N_2$. The slides were etched with piranha solution (**Caution**: since Piranha solution ($H_2SO_4$/30% $H_2O_2$, 7:3) reacts violently with many organic compounds, extreme care must be taken when handling it) for 30 min to remove residual organic material and activate hydroxyl groups on the surface. The cleaned substrates were rinsed with Milli-Q water in a 200 mL beaker at least six times and further washed with ethanol three times. Slides were then transferred to a 200 mL beaker containing 2% (3-aminopropyl)triethoxysilane (APTES) in ethanol for 1 h and then washed with ethanol three times and thermally cured in an oven (~ 110 ℃) for 1- min, The APTES-functionalized slides were mounted to a custom-made 30-well microfluidic chamber fabricated from Delrin (McMasterCarr, cat. #8573K15). The nanosheet solution was added (10 $\mu$L) to the well and was immediately subjected to a wash (3 x 100 $\mu$L) with 20 mM MOPS buffer (pH 7.0). Assembly location was determined using RICM imaging. After focusing using RICM, wide-field epifluorescence micrographs were acquired.

**Small-angle/Wide-angle X-ray scattering measurements**.

Synchrotron SAXS/WAXS measurements were performed at the 12-ID-B beamline of the Advanced Photon Source at Argonne National Laboratory. The sample-to-detector distances were set such that the overall scattering momentum transfer, $q$, range was achieved from 0.005 to 0.9 $Å^{-1}$, where $q = 4\pi \sin \theta/\lambda$, with 2 $\theta$ denoting the scattering angle and $\lambda$ denoting the X-ray wavelength. The wavelength was set at 0.9322 Å during the measurements. Scattered X-ray intensities were measured using a Pilatus 2 M (DECTRIS Ltd.) detector. Measurements were conducted on aqueous solutions of CMP nanosheets at a concentration of 4 mg/mL in 20 mM MOPS buffer (pH 7.0) at 5 °C. A quartz capillary flow cell (1.5 mm diameter) was employed to prevent radiation damage. The 2D scattering images were converted to 1D scattering curves through azimuthal averaging after solid angle correction and then normalizing with the intensity of the transmitted X-ray beam using the software package at beamline 12-ID-B. The 1D curves of the samples were averaged and subtracted with the background measured from the corresponding buffers.

**1.7. References**

(1) Zhuang, X.; Mai, Y.; Wu, D.; Zhang, F.; Feng, X. Two-dimensional soft nanomaterials: a fascinating world of materials. *Adv Mater* **2015**, *27* (3), 403-427. DOI: 10.1002/adma.201401857.

(2) K. S. Novoselov, A. K. G.; S. V. Morozov, D. J.; Y. Zhang, S. V. D., I. V. Grigorieva, A. A. Firsov. Electric Field Effect in Atomically Thin Carbon Films. *Science* **2004**, *206*, 666-669.

(3) Liu, S.; Pan, X.; Liu, H. Two-Dimensional Nanomaterials for Photothermal Therapy. *Angew Chem Int Ed Engl* **2020**, *59* (15), 5890-5900. DOI: 10.1002/anie.201911477 From NLM Medline.

(4) Nazemi, A.; He, X.; MacFarlane, L. R.; Harniman, R. L.; Hsiao, M. S.; Winnik, M. A.; Faul, C. F.; Manners, I. Uniform "Patchy" Platelets by Seeded Heteroepitaxial Growth of Crystallizable Polymer Blends in Two Dimensions. *J Am Chem Soc* **2017**, *139* (12), 4409-4417. DOI: 10.1021/jacs.6b12503.

(5) He, X.; Hsiao, M. S.; Boott, C. E.; Harniman, R. L.; Nazemi, A.; Li, X.; Winnik, M. A.; Manners, I. Two-dimensional assemblies from crystallizable homopolymers with charged termini. *Nat Mater* **2017**, *16* (4), 481-488. DOI: 10.1038/nmat4837.

(6) Zhang, X.; Li, H.; Wang, J.; Peng, D.; Liu, J.; Zhang, Y. In-situ grown covalent organic framework nanosheets on graphene for membrane-based dye/salt separation. *Journal of Membrane Science* **2019**, *581*, 321-330. DOI: 10.1016/j.memsci.2019.03.070.

(7) Zhu, H. J.; Lu, M.; Wang, Y. R.; Yao, S. J.; Zhang, M.; Kan, Y. H.; Liu, J.; Chen, Y.; Li, S. L.; Lan, Y. Q. Efficient electron transmission in covalent organic framework nanosheets for highly active electrocatalytic carbon dioxide reduction. *Nat Commun* **2020**, *11* (1), 497. DOI: 10.1038/s41467-019-14237-4.

(8) Yao, H.; Yang, Y.; Pan, S.; Zhao, R.; Cai, Y.; Zhang, S.; Li, H. Covalent Organic Framework Nanosheets for Fluorescence Quantification of Peptide. *Anal Chem* **2023**, *95* (25), 9638-9645. DOI: 10.1021/acs.analchem.3c01381 From NLM Medline.

(9) Vybornyi, M.; Rudnev, A.; Häner, R. Assembly of Extra-Large Nanosheets by Supramolecular Polymerization of Amphiphilic Pyrene Oligomers in Aqueous Solution. *Chemistry of Materials* **2015**, *27* (4), 1426-1431. DOI: 10.1021/acs.chemmater.5b00047.

(10) Feng, X.; Kawabata, K.; Whang, D. M.; Osuji, C. O. Polymer Nanosheets from Supramolecular Assemblies of Conjugated Linoleic Acid-High Surface Area Adsorbents from Renewable Materials. *Langmuir* **2017**, *33* (40), 10690-10697. DOI: 10.1021/acs.langmuir.7b02467.

(11) Han, L.; Wang, M.; Jia, X.; Chen, W.; Qian, H.; He, F. Uniform two-dimensional square assemblies from conjugated block copolymers driven by pi-pi interactions with controllable sizes. *Nat Commun* **2018**, *9* (1), 865. DOI: 10.1038/s41467-018-03195-y.

(12) Dai, B.; Li, D.; Xi, W.; Luo, F.; Zhang, X.; Zou, M.; Cao, M.; Hu, J.; Wang, W.; Wei, G.; et al. Tunable assembly of amyloid-forming peptides into nanosheets as a retrovirus carrier. *Proc Natl Acad Sci U S A* **2015**, *112* (10), 2996-3001. DOI: 10.1073/pnas.1416690112.

(13) Lin, Y.; Thomas, M. R.; Gelmi, A.; Leonardo, V.; Pashuck, E. T.; Maynard, S. A.; Wang, Y.; Stevens, M. M. Self-Assembled 2D Free-Standing Janus Nanosheets with Single-Layer Thickness. *J Am Chem Soc* **2017**, *139* (39), 13592-13595. DOI: 10.1021/jacs.7b06591.

(14) Jiang, T.; Xu, C.; Zuo, X.; Conticello, V. P. Structurally homogeneous nanosheets from self-assembly of a collagen-mimetic peptide. *Angew Chem Int Ed Engl* **2014**, *53* (32), 8367-8371. DOI: 10.1002/anie.201403780.

(15) Jiang, T.; Vail, O. A.; Jiang, Z.; Zuo, X.; Conticello, V. P. Rational Design of Multilayer Collagen Nanosheets with Compositional and Structural Control. *J Am Chem Soc* **2015**, *137* (24), 7793-7802. DOI: 10.1021/jacs.5b03326.

(16) Merg, A. D.; Touponse, G.; van Genderen, E.; Zuo, X.; Bazrafshan, A.; Blum, T.; Hughes, S.; Salaita, K.; Abrahams, J. P.; Conticello, V. P. 2D Crystal Engineering of Nanosheets Assembled from Helical Peptide Building Blocks. *Angew Chem Int Ed Engl* **2019**, *58* (38), 13507-13512. DOI: 10.1002/anie.201906214.

(17) Merg, A. D.; van Genderen, E.; Bazrafshan, A.; Su, H.; Zuo, X.; Touponse, G.; Blum, T. B.; Salaita, K.; Abrahams, J. P.; Conticello, V. P. Seeded Heteroepitaxial Growth of Crystallizable Collagen Triple Helices: Engineering Multifunctional Two-Dimensional Core-Shell Nanostructures. *J Am Chem Soc* **2019**, *141* (51), 20107-20117. DOI: 10.1021/jacs.9b09335.

(18) Magnotti, E. L.; Hughes, S. A.; Dillard, R. S.; Wang, S.; Hough, L.; Karumbamkandathil, A.; Lian, T.; Wall, J. S.; Zuo, X.; Wright, E. R.; et al. Self-Assembly of an alpha-Helical Peptide into a Crystalline Two-Dimensional Nanoporous Framework. *J Am Chem Soc* **2016**, *138* (50), 16274-16282. DOI: 10.1021/jacs.6b06592.

(19) Lee, J.; Choe, I. R.; Kim, N. K.; Kim, W. J.; Jang, H. S.; Lee, Y. S.; Nam, K. T. Water-Floating Giant Nanosheets from Helical Peptide Pentamers. *ACS Nano* **2016**, *10* (9), 8263-8270. DOI: 10.1021/acsnano.6b00646.

(20) Insua, I.; Montenegro, J. 1D to 2D Self Assembly of Cyclic Peptides. *J Am Chem Soc* **2020**, *142* (1), 300-307. DOI: 10.1021/jacs.9b10582 From NLM Medline.

(21) Robertson, E. J.; Battigelli, A.; Proulx, C.; Mannige, R. V.; Haxton, T. K.; Yun, L.; Whitelam, S.; Zuckermann, R. N. Design, Synthesis, Assembly, and Engineering of Peptoid Nanosheets. *Acc Chem Res* **2016**, *49* (3), 379-389. DOI: 10.1021/acs.accounts.5b00439.

(22) Gao, H.; Wang, J.; Liu, J.; Ye, S.; Meng, X.; Song, S.; Wang, C.; Yu, X.; Zhu, L.; Wang, H.; et al. Peptoid Nanosheet-Based Sensing System for the Diagnosis and Surveillance of Amnestic Mild Cognitive Impairment and Alzheimer's Disease. *ACS Chem Neurosci* **2021**, *12* (22), 4257-4264. DOI: 10.1021/acschemneuro.1c00613 From NLM Medline.

(23) Song, Y.; Wang, M.; Akkineni, S.; Yang, W.; Hettige, J. J.; Jin, H.; Liao, Z.; Mu, P.; Yan, F.; Baer, M.; et al. Highly Bright and Photostable Two-Dimensional Nanomaterials Assembled from Sequence-Defined Peptoids. *ACS Materials Letters* **2021**, *3* (4), 420-427. DOI: 10.1021/acsmaterialslett.1c00110.

(24) Yu, H.; Alexander, D. T. L.; Aschauer, U.; Haner, R. Synthesis of Responsive Two-Dimensional Polymers via Self-Assembled DNA Networks. *Angew Chem Int Ed Engl* **2017**, *56* (18), 5040-5044. DOI: 10.1002/anie.201701342.

(25) Fard, P. T.; Albert, S. K.; Ko, J.; Lee, S.; Park, S.-J.; Kim, J. Spatial Organization of Photocatalysts and Enzymes on Janus-Type DNA Nanosheets for Efficient CO2 Conversion. *ACS Catalysis* **2022**, *12* (15), 9698-9705. DOI: 10.1021/acscatal.2c02911.

(26) Albert, S. K.; Lee, S.; Durai, P.; Hu, X.; Jeong, B.; Park, K.; Park, S. J. Janus Nanosheets with Face-Selective Molecular Recognition Properties from DNA-Peptide Conjugates. *Small* **2021**, *17* (12), e2006110. DOI: 10.1002/smll.202006110 From NLM Medline.

(27) Strauss, K.; Chmielewski, J. Advances in the design and higher-order assembly of collagen mimetic peptides for regenerative medicine. *Curr Opin Biotechnol* **2017**, *46*, 34-41. DOI: 10.1016/j.copbio.2016.10.013.

(28) Shoulders, M. D.; Raines, R. T. Collagen structure and stability. *Annu Rev Biochem* **2009**, *78*, 929-958. DOI: 10.1146/annurev.biochem.77.032207.120833.

(29) Egli, J.; Siebler, C.; Maryasin, B.; Erdmann, R. S.; Bergande, C.; Ochsenfeld, C.; Wennemers, H. pH-Responsive Aminoproline-Containing Collagen Triple Helices. *Chemistry* **2017**, *23* (33), 7938-7944. DOI: 10.1002/chem.201701134.

(30) Siebler, C.; Erdmann, R. S.; Wennemers, H. Switchable proline derivatives: tuning the conformational stability of the collagen triple helix by pH changes. *Angew Chem Int Ed Engl* **2014**, *53* (39), 10340-10344. DOI: 10.1002/anie.201404935.

(31) Wittmann, J. C.; Lotz, B. Epitaxial crystallization of polyethylene on organic substrates: A reappraisal of the mode of action of selected nucleating agents. *Journal of Polymer Science: Polymer Physics Edition* **2003**, *19* (12), 1837-1851. DOI: 10.1002/pol.1981.180191204.

(32) Okuyama, K. Revisiting the molecular structure of collagen. *Connect Tissue Res* **2008**, *49* (5), 299-310. DOI: 10.1080/03008200802325110.

# Chapter 2. Structurally and dimensionally defined multicomponent blended nanosheets from self-assembly of collagen-mimetic peptides

*Acknowledgement:*

*This research used resources of the Advanced Photon Source, a U.S. Department of Energy (DOE) Office of Science user facility operated for the DOE Office of Science by Argonne National Laboratory under Contract No. DE-AC02-06CH11357.*

## 2. 1. Introduction

In the previous chapter, we presented our work on the mixed assemblies of two CMP pairs, $4S(X)_{535}$ – $4S(X)_{545}$ and $4R(X)_{444}$ and $4S(Y)_{444}$. Our results support the hypothesis that by mixing and co-annealing two different CMPs, we are able to create multicomponent nanosheets of intermediate properties between the two single-component systems. Furthermore, varying the ratios between two peptides in the mixture solution will allow for fine-tuning the properties of the resultant nanosheets (i.e., lateral dimensions and thermal stability). However, the remaining question is whether the mixed nanosheet is "blended" such that the two CMPs are randomly distributed across the nanosheet structure. We previously tried to employ fluorescent microscopy and SAXS/WAXS experiments to gain more insight into the internal structures of the assemblies. However, both CMP pairs studied form mixed nanosheets that are too small for fluorescent imaging at a good resolution. Moreover, $4S(X)_{535}$ and $4S(X)_{545}$ are too similar in structure so they are indiscernible under SAXS/WAXS, while $4R(X)_{444}$ and $4S(Y)_{444}$ encounter a concentration

problem that makes the interpretation of SAXS data ambiguous. Therefore, our aim is to construct another series of mixed nanosheets that are (1) compatible in lattice packing parameters to avoid destabilization like in the case of $4R(X)_{444}$ - $4S(Y)_{444}$, and (2) larger in dimensions than $4S(X)_{535}$ – $4S(X)_{545}$ nanosheets and hence more suitable for fluorescent imaging. In addition, we plan to utilize high-resolution cryo-TEM imaging to probe the lattice structure in further details. Shown below are the two chosen CMPs and their sequences.

$4S(X)_{444}$ $(amp\text{-}Hyp\text{-}Gly)_4 – (Pro\text{-}Hyp\text{-}Gly)_4 – (Pro\text{-}Glu\text{-}Gly)_4$
$4S(X)_{454}$ $(amp\text{-}Hyp\text{-}Gly)_4 – (Pro\text{-}Hyp\text{-}Gly)_5 – (Pro\text{-}Glu\text{-}Gly)_4$

These two peptides meet our criteria as they are significantly different in size and melting temperature (Figure 1). $4S(X)_{454}$ is longer than $4S(X)_{444}$ by only one triad, so the electrostatic interaction between two CMP triple helices should still be sufficient to promote cohesion. Furthermore, a lattice mismatch of around 3% is expected to still be acceptable for compatible packing of the two CMPs. However, unlike the previous systems where the two CMPs in a pair assemble under the same temperature, pure $4S(X)_{444}$ is incubated at 4 ℃ while $4S(X)_{454}$ is at RT. Results from our previous paper[1] suggested that the assembly temperature could have a significant influence on the optimal conditions for nanosheet formation, probably due to its effect on triple helix stability. Therefore, in case of the $4S(X)_{444}$ – $4S(X)_{454}$ pair where each CMP assembles at a different temperature, it is critical to determine under which condition their mixtures would be the most well-behaved. Our ideal condition should facilitate the formation of a homogenous population of nanosheets with sharp and well-defined edges.

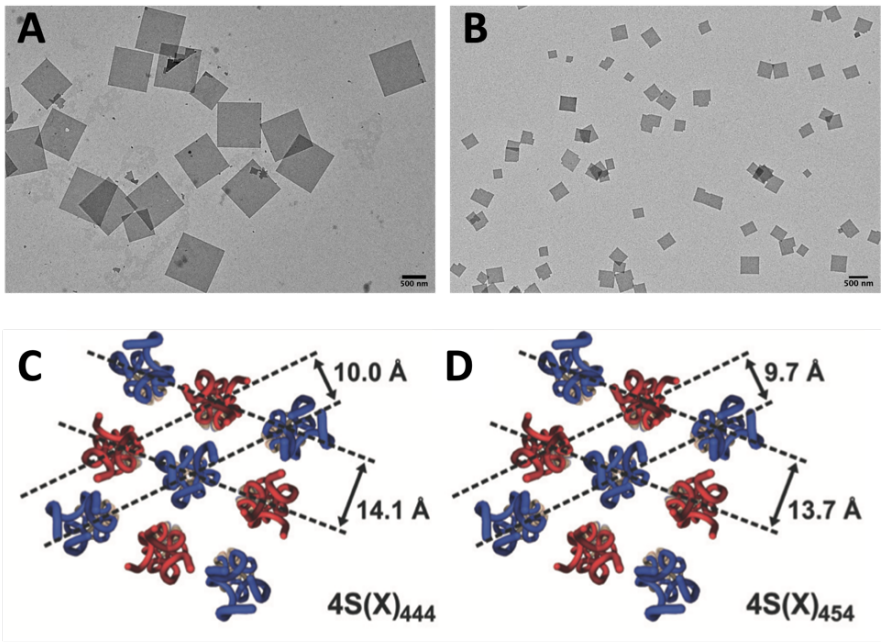


E

| Peptide | Diagonal length of nanosheets (nm) | Melting temperature (℃) |
|---|---|---|
| $4S(X)_{444}$ | $953 \pm 72$ | 34.0 |
| $4S(X)_{454}$ | $432 \pm 101$ | 50.0 |

**Figure 1.** Properties of pure $4S(X)_{444}$ and $4S(X)_{454}$ nanosheets. TEM images of (A) $4S(X)_{444}$ and (B) $4S(X)_{454}$ nanosheets (scale bar = 500 nm). Previously solved models for the assemblies of (C) $4S(X)_{444}$ and (D) $4S(X)_{454}$, adapted from Merg et al[1]. (E) Diagonal length and melting temperatures of pure $4S(X)_{444}$ and $4S(X)_{454}$ nanosheets.

### 2.2. Identifying a suitable temperature for incubating the mixed assemblies

The two peptides are mixed in three ratios: 75% $4S(X)_{444}$ – 25% $4S(X)_{454}$, 50% $4S(X)_{444}$ – 50% $4S(X)_{454}$, and 25% $4S(X)_{444}$ – 50% $4S(X)_{454}$ to a final concentration of 4 mg/mL. The mixture solutions are then thermally annealed at 90 ℃ for 15 minutes, slow cooled by 1 ℃/5 minutes, and incubated at 4 ℃, 15 ℃ or RT for two weeks prior to characterization. Since pure $4S(X)_{454}$ forms smaller nanosheets (Figure 1), the size of the mixed assemblies decreases with higher percentage

of $4S(X)_{454}$ in the solution mixture (Figure 2, Table S1). However, at 4 ℃, a fair number of the 75% $4S(X)_{444}$ – 25% $4S(X)_{454}$ nanosheets start to dissociate after two weeks. In addition, the mixture at 25% $4S(X)_{444}$ – 75% $4S(X)_{454}$ forms nanosheets with irregular edges. This effect is even more prominent at 10% $4S(X)_{444}$ – 90% $4S(X)_{454}$ (Figure S1). The reason could be that the nanosheets at these two ratios resemble the behavior of pure $4S(X)_{454}$, whose optimal temperature is RT. The rapid cooling to 4 ℃ probably misses the crystallization point, causing the triple helices not having enough time to pack into more ordered structures.

Adjusting the incubation temperature to RT indeed helps to regain the formation of well-defined nanosheets at 25% $4S(X)_{444}$ – 75% $4S(X)_{454}$ (Figure 2). However, the nanosheets at 75% $4S(X)_{444}$ – 25% $4S(X)_{454}$ now become more polydisperse in size (Table S1). This might have happened because at this temperature, the assembly nucleation rate is competitive with elongation rate and results in high polydispersity.

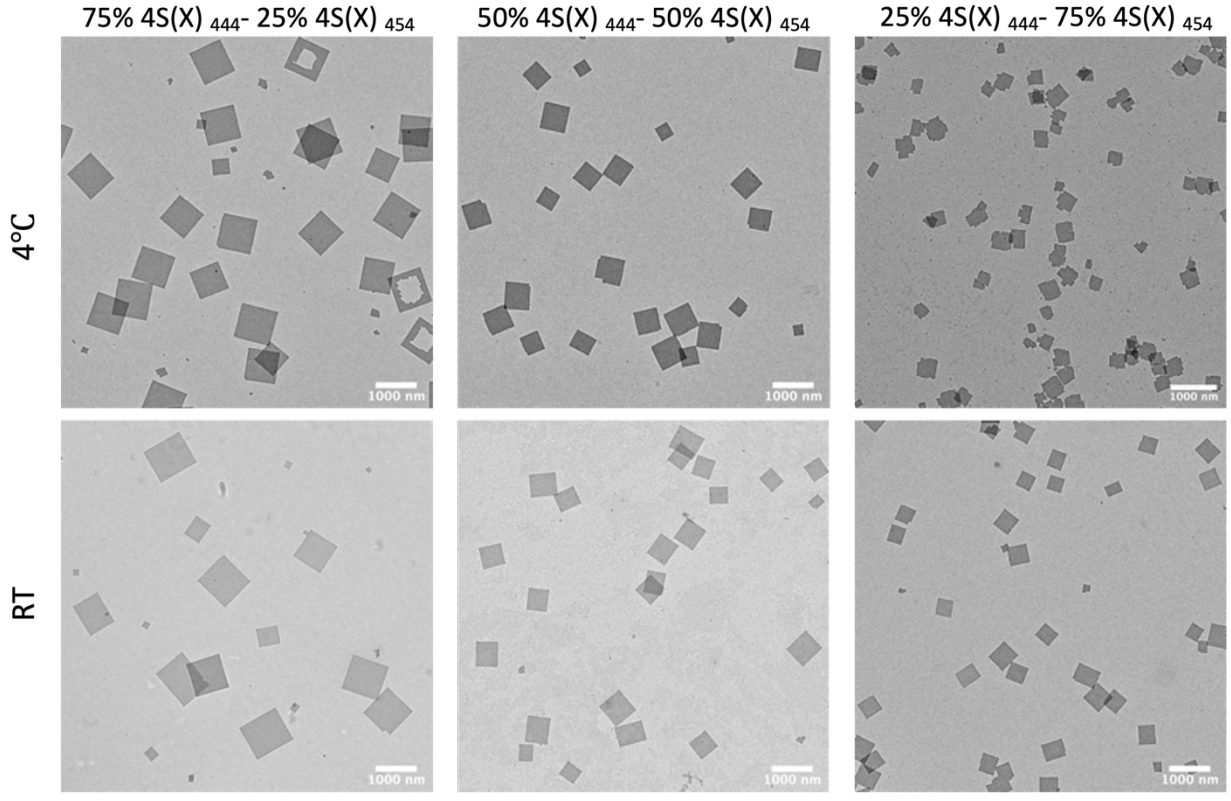

**Figure 2.** Mixed assemblies between $4S(X)_{444}$ and $4S(X)_{454}$ peptides when incubated at either 4 ℃ or RT (scale bars = 1 $\mu$m).

After testing out the mixed assemblies at 15 ℃, it turns out that this incubation temperature is optimal for the formation of mixed nanosheets that are more stable and homogenous in size (Figure 3). Therefore, our subsequent studies are carried out on assemblies at this condition.

### 2.3. Characterization of $4S(X)_{444}$ – $4S(X)_{454}$ blended nanosheets assembled at 15 ℃

It should be noted that at 15 ℃, pure $4S(X)_{454}$ still assembles into nanosheets with jagged edges (Figure S2), which is evidence of reduced crystallinity. We still performed thermal denaturation study (Figure S3) and SAXS/WAXS experiment on those nanosheets. However, their undefined edges interfere with size measurement and hence their diagonal length is not reported.

#### 2.3.1. Size distribution

The $4S(X)_{444}$ – $4S(X)_{454}$ peptide mixtures assemble into well-defined nanosheets of homogenous size at 15 ℃ (Figure 3, Table 1). It is interesting to note that even the pure $4S(X)_{444}$ peptide, previously found to assemble at 4 ℃, still assembles at 15 ℃. The nanosheets at 15 ℃ ($L_d$ = 1069 ± 175 nm) appear slightly larger and more variable in size than those at 4 ℃ ($L_d$ = 953 ± 72 nm). Despite the irregular shapes, pure $4S(X)_{454}$ nanosheets are still smaller than $4S(X)_{444}$ ones. Therefore, increasing the percentage of $4S(X)_{454}$ peptide in the mixture still results in a decrease in size of the assemblies (Figure 3A, B, Table 1).

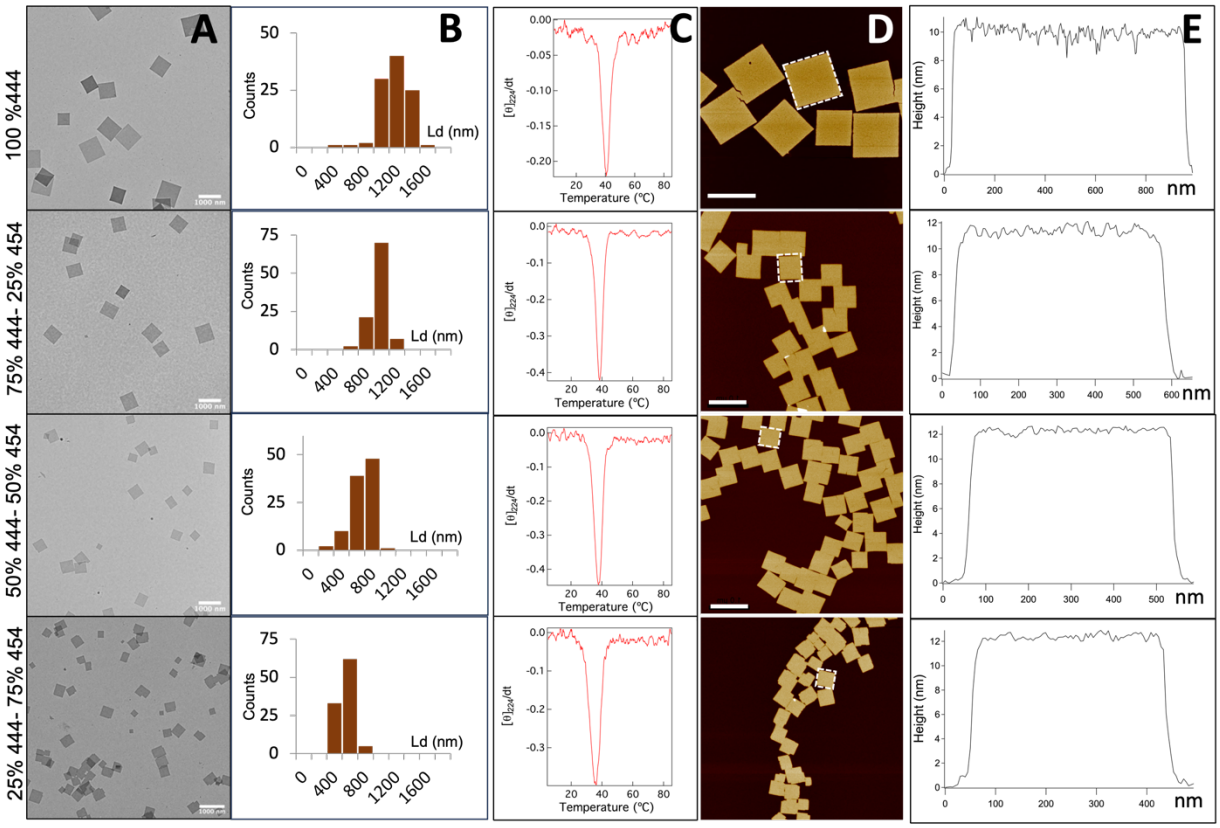


**Figure 3.** Characterization of the $4S(X)_{444} – 4S(X)_{454}$ pure and mixed nanosheets, assembled at 15 ℃. (A) TEM images (scale bar = 1 $\mu$m), (B) Diagonal length distribution of the nanosheets based on TEM (100 counts each), (C) First derivative of the CD signal at 224 nm as a function of temperature, (D) AFM images (scale bar = 1 $\mu$m), (E) Height profile across center of the boxed nanosheet in (D).

**Table 1**. Characterization of $4S(X)_{535}$ – $4S(X)_{545}$ mixed nanosheets. Size measurement for 100% $4S(X)_{545}$ nanosheets is not available due to their undefined edges. The sheet thickness of pure $4S(X)_{454}$ is measured from assembly at RT (Figure S4).

| %$4S(X)_{444}$ : %$4S(X)_{454}$ | Diagonal length from TEM (nm) | Melting temperature (℃) | Sheet thickness (nm) |
|---|---|---|---|
| 100:0 | $1069 \pm 175$ | 40.6 | $9.9 \pm 0.4$ |
| 75:25 | $865 \pm 107$ | 38.4 | $10.9 \pm 0.4$ |
| 50:50 | $581 \pm 145$ | 37.8 | $11.6 \pm 0.3$ |
| 25:75 | $447 \pm 104$ | 36.2 | $12.2 \pm 0.4$ |
| 0:100 | Undefined edges | 36.0 | $12.2 \pm 0.5$ |

In addition to measurement from TEM images, dynamic light scattering (DLS) was also employed for obtaining size distribution. Even though the Stokes-Einstein relationship is not valid for 2D assemblies, the population of nanosheets could still be fit to a single curve that is consistent with a uniform size distribution of self-assembled species. DLS measurements also agree with the overall decreasing trend in size of the nanosheets with more $4S(X)_{454}$ present (Figure S5).

### 2.3.2. Thermal stability

The first derivative of each melting curve shows a single melting transition (Figure 3C), suggesting the presence of only one population of nanosheets, hence implying formation of mixed nanosheets. As pure $4S(X)_{444}$ sheets at 15 ℃ are larger than at 4 ℃, they also melt at a higher

temperature ($T_m$ increases by approximately 6 ℃). In the case of pure $4S(X)_{454}$, the reduction in crystallinity results in less thermally stable assemblies than at RT ($T_m$ decreases by approximately 14 ℃). Nevertheless, the melting transitions of the mixed nanosheets still fall in the range between those of pure ones and gradually decrease with more $4S(X)_{454}$ present.

### 2.3.3. AFM height measurement

The theoretical thicknesses for monolayer nanosheets of $4S(X)_{444}$ and $4S(X)_{454}$ are 10.3 nm and 11.2 nm, respectively (0.286 nm rise/residue).[32] AFM analysis of the nanosheets reveal average sheet thicknesses that are in this range. Since the difference in height between $4S(X)_{454}$ and $4S(X)_{444}$ (approximately 0.9 nm) is not much larger than the standard deviations of the measurements, it is uncertain to say the spikes in the height traces represent areas where the taller $4S(X)_{454}$ is detected. Nevertheless, the fluctuations in the height profiles appear to be random rather than following a specific pattern, so there should be no large single-component domain present here like in the case of the core-shell assembly.

The average thickness of the nanosheets reveals a gradual increase with more $4S(X)_{454}$ mixed in (Table 1). This observation agrees with our SAXS data (Figure 5). These results imply that thickness of the nanosheet is another tunable property.

### 2.3.4. Fluorescent imaging

Due to the size limitation of fluorescent imaging, this experiment was only conducted on the 75% $4S(X)_{444}$ – 25% $4S(X)_{454}$ nanosheets. A solution mixture of $4S(X)_{444}$, $4S(X)_{454}$, N-terminal-modified azido and biotin derivatives ($N_3$-$4S(X)_{444}$ and b-$4S(X)_{454}$) is annealed to form mixed nanosheets. Subsequently, the assemblies were incubated with streptavidin-tagged Cy3B

and DBCO-tagged AF647. After removal of excess dye, fluorescent optical microscopy experiments confirm the colocalization of both fluorophores on a single nanosheet (Figure 4, Figure S6).

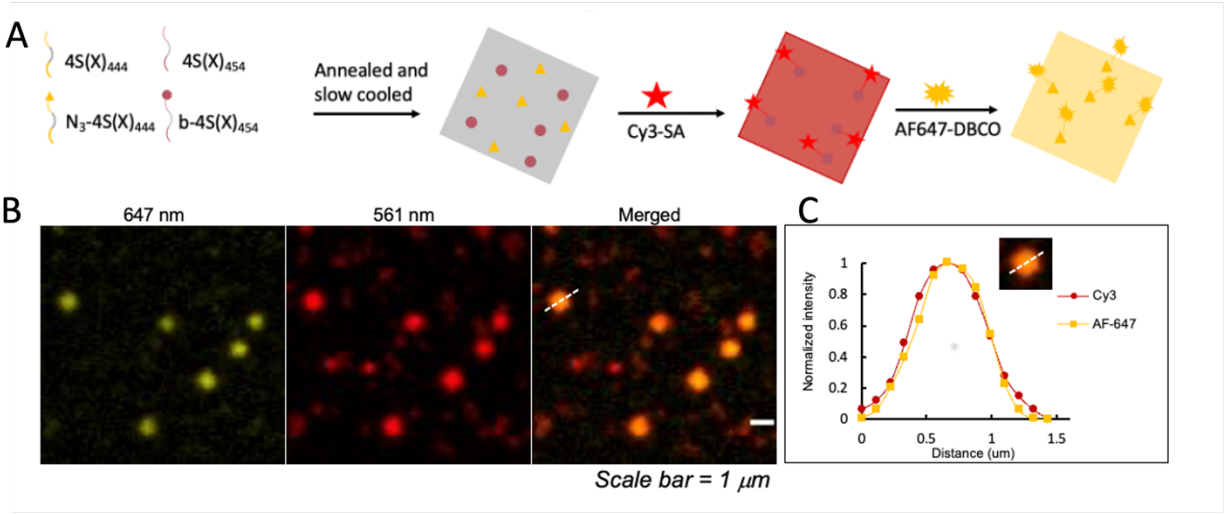


**Figure 4.** Fluorescent imaging experiment on 75% $4S(X)_{444}$ – 25% $4S(X)_{454}$ nanosheets. (A) Scheme detailing the site-specific attachment of Cy3B-SA and AF647-DBCO onto the nanosheets. (B) Fluorescence optical micrographs of 75% $4S(X)_{444}$ – 25% $4S(X)_{454}$ nanosheets labelled with AF647 and Cy3B at different emission wavelengths. The merged channel reveals the colocalization of the two fluorophores. (C) Overlapping of Cy3B and AF-647 signals across a single nanosheet.

The fluorescent micrographs show no segregation of the two fluorophores to different areas of the nanosheet. The overlapping signal of the two fluorophores (Figure 20C) implies that they are in close proximity. This observation, along with AFM results, implies that the nanosheets may be blended rather than sectored. However, due to the limited resolution, we are still unclear how close the two fluorophores, hence the two CMPs, are to each other.

### 2.3.5. SAXS/WAXS scattering profiles

The scattering curves of all assembly solutions verify a similar underlying structure (Figure 5A). Form-factor scattering intensities in the low-$q$ region ($q < 0.02$ Å$^{-1}$) roughly follow a $q^{-2}$ power law, indicating sheetlike morphology for all CMP nanosheets. Fitting the low-$q$ data using the Guinier equation for sheetlike forms returns average sheet thicknesses that are consistent with AFM and theoretical height calculations (Figure 5C, Figure S7). The calculated thickness also gradually increases with a higher percentage of 4S(X)$_{454}$ peptide in the mixture. The oscillations in the $q$ range of $\sim 0.04 - 0.2$ Å$^{-1}$ arise from the thickness of the nanosheets, and its attenuation reflects the variation in sheet thickness.[1-3]

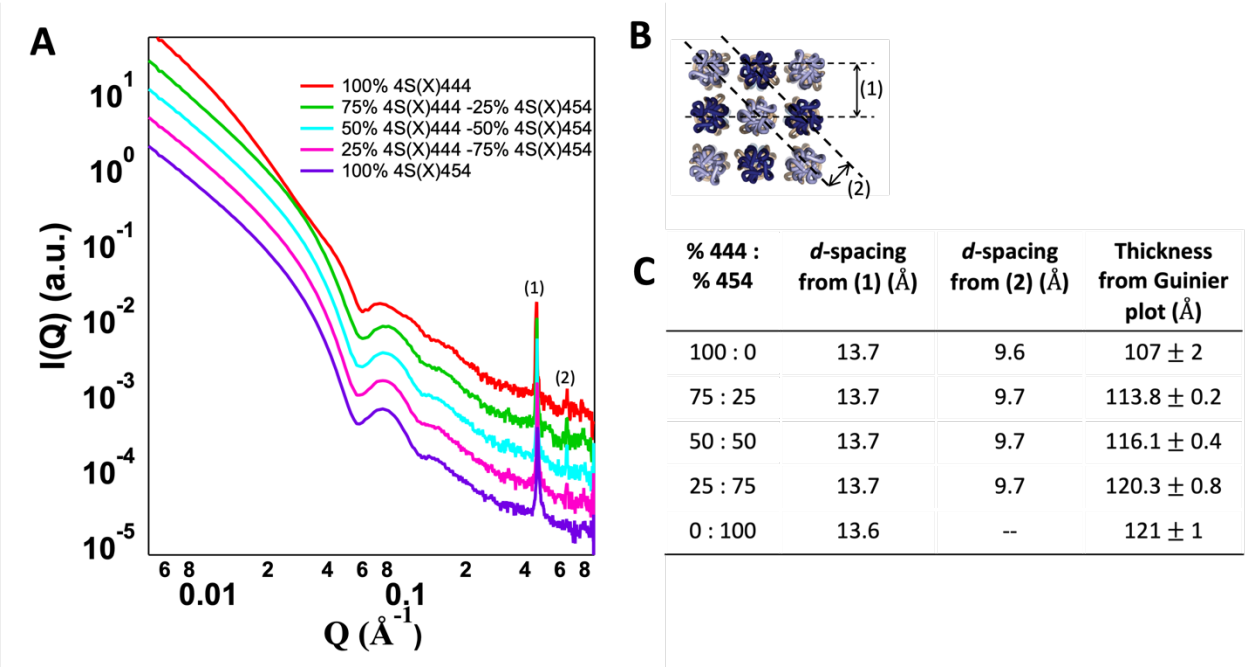


| % 444 : % 454 | *d*-spacing from (1) (Å) | *d*-spacing from (2) (Å) | Thickness from Guinier plot (Å) |
|---|---|---|---|
| 100 : 0 | 13.7 | 9.6 | $107 \pm 2$ |
| 75 : 25 | 13.7 | 9.7 | $113.8 \pm 0.2$ |
| 50 : 50 | 13.7 | 9.7 | $116.1 \pm 0.4$ |
| 25 : 75 | 13.7 | 9.7 | $120.3 \pm 0.8$ |
| 0 : 100 | 13.6 | -- | $121 \pm 1$ |

**Figure 5.** Synchrotron SAXS/WAXS analysis on 4S(X)$_{444}$ – 4S(X)$_{454}$ system. (A) Scattering profiles of 4S(X)$_{444}$, 4S(X)$_{454}$ and their mixed assemblies, (B) Assembly model of the nanosheets (C) Corresponding *d*-spacing values associated with peaks (1) and (2), and thickness of the assemblies generated from Guinier plots.

The presence of Bragg diffraction peaks in the high q region of the intensity plot indicate a high degree of crystallinity within the assemblies. All nanosheet samples have two Bragg peaks, except for the 100% $4S(X)_{454}$ with only one peak, again suggesting less ordered packing of $4S(X)_{454}$ at 15 ℃. For all ratios, the calculated *d*-spacing for peak (1) is roughly equal to $\sqrt{2}$ × peak (2), indicating that the tetragonal lattice is preserved in all assemblies. Interestingly, the *d*-spacings for 100% $4S(X)_{444}$ nanosheets obtained here are different from our previous results.[1] This can be attributed to the nanosheets now being assembled at 15℃ instead of at 4 ℃. Moreover, the calculated *d*-spacings are similar across all assemblies. In our earlier study on nanotubes, we found that SAXS measurement is limited in distinguishing heterogeneity that arises from the presence of closely related structural polymorphs[33] and that could also be the case here. Therefore, we will need to utilize cryo-TEM for a more reliable structural analysis.

### 2.3.6. High-resolution cryo-TEM analysis

Cryo-TEM with direct electron detection was employed on 50% $4S(X)_{444}$ – 50% $4S(X)_{454}$ nanosheets to study their internal structure in further details. High-resolution images confirm the ordered tetragonal packing of individual triple helices within the nanosheet assembly (Figure S8).

Previously in the construction of the multicomponent core-shell nanosheets, fast Fourier transform (FFT) analysis of cryo-TEM images confirmed the presence of two distinct crystal lattices as evidenced by two separate sets of Bragg spots (Figure S9). Selected area FFTs of the shell and core regions were analyzed and found that both the core and shell maintain their own intrinsic lattices (Figure 6).

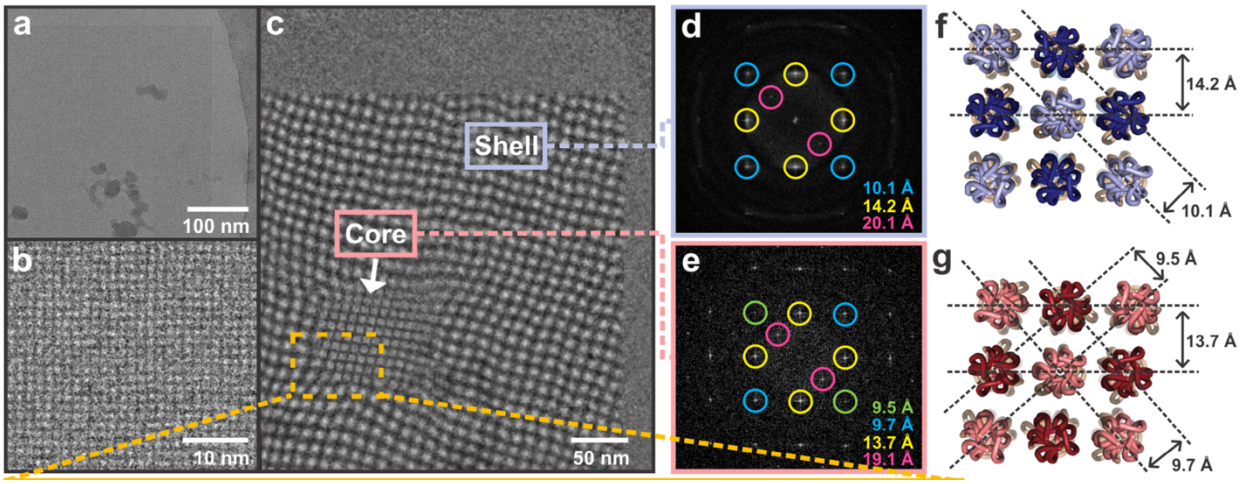


**Figure 6.** Cryo-TEM analysis of a core-shell nanosheet, adapted from Merg et al.[3] (a) Cryo-TEM image of a nanosheet with $4R(X)_{444}$ core and $4S(X)_{444}$ shell. (b) Enlarged image revealing tetragonal lattice packing. (c) Moiré evaluation applied to the nanosheet to visualize the core and shell sectors. FFT analysis of (d) $4S(X)_{444}$ shell and (e) $4R(X)_{444}$ core. Proposed packing model of (f) $4S(X)_{444}$ shell and (g) $4R(X)_{444}$ core.

Similar to the previous study of core-shell assembly, FFT analysis can also be employed to study the presence of 2D lattices in the mixed nanosheets (Figure 7). A 4-fold rotational symmetry confirms the tetragonal lattice of the assembly. FFT of the nanosheets yield bright spots that extend to a resolution of ~6.1 Å (Figure S10). This resolution is lower than those of single-component nanosheets,[1] implying that the mixed assemblies are less ordered.

FFT analysis of the 50% $4S(X)_{444}$ – 50% $4S(X)_{454}$ nanosheet returns double-peak pattern of the spots (Figure 7). The measured distances of 14.1 – 14.3 Å and 9.9 – 10 Å should correspond to (010) and (111) plane distances in the model, respectively. The ~20 Å spots are double of the 10 Å spots, so that could be another array of the triple helices in the direction of the (111) plane. Intriguingly, there is another set of spots at ~16 Å. The same phenomenon is observed when FFT is taken for a selected area on the nanosheet (Figure 7C).

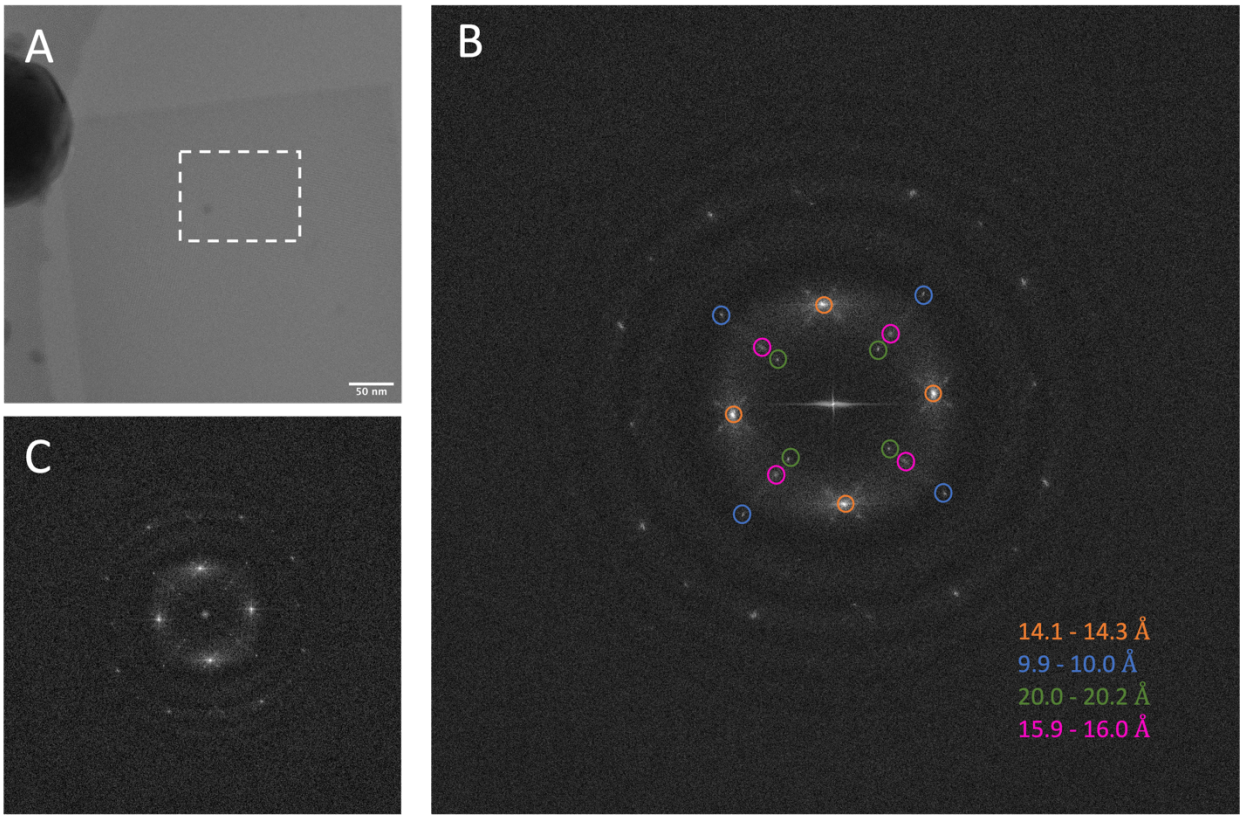


**Figure 7.** High-resolution cryo-TEM of a 50% $4S(X)_{444}$ – 50% $4S(X)_{454}$ and its corresponding FFT analysis. (A) Cryo-TEM image, (B) FFT of the whole nanosheet with measured *d*-spacings, (C) FFT of the boxed area in (A).

To determine whether the presence of double peaks in the FFT is consistent across the whole nanosheet, we utilized an in-house script to randomly sample patches of size 301 x 301 pixels (~ 33 x 33 nm) on the cryo-TEM micrographs (Figure 8). FFT was then computed for each patch. Subsequently, the distance from the center of the power spectrum to the peaks can be calculated. The angle between any two vectors from the center to a peak was also found. The angle and distance were later used by a tree-based classification method to classify the FFTs into different classes (Figure 8B, S11). A point to remember is that since classification was first done based on the angle then again on the distance, double classification of a single patch could have happened.

In other words, sometimes patches from two classes are not essentially different, considering how similar their average FFTs are to each other (Figure S11, class 2 and 3). Nevertheless, a clear double-peak pattern is again observed even at this small patch size. The resemblance between the FFT of ~33 nm x 33 nm patches and FFT of the whole nanosheet ($L_d = 581 \pm 145$ nm) indicates that the mixing pattern between two CMPs stays consistent down to ~ 33-nm scale. There is no large single-component patch detected, and the mixed nanosheets should be blended as expected by our hypothesis. Out of the 66 nanosheets analyzed, 82% displayed the a similar double-peak pattern in their corresponding FFTs (Figure S12, S32, S14).

Interestingly, the double-peak pattern only shows up in the 45° direction (Figure 8C). This implies that there could be some types of stress in the crystal structure that is only specific to that direction, which should correspond to the (111) plane distance in the assembly model (Figure 8D).

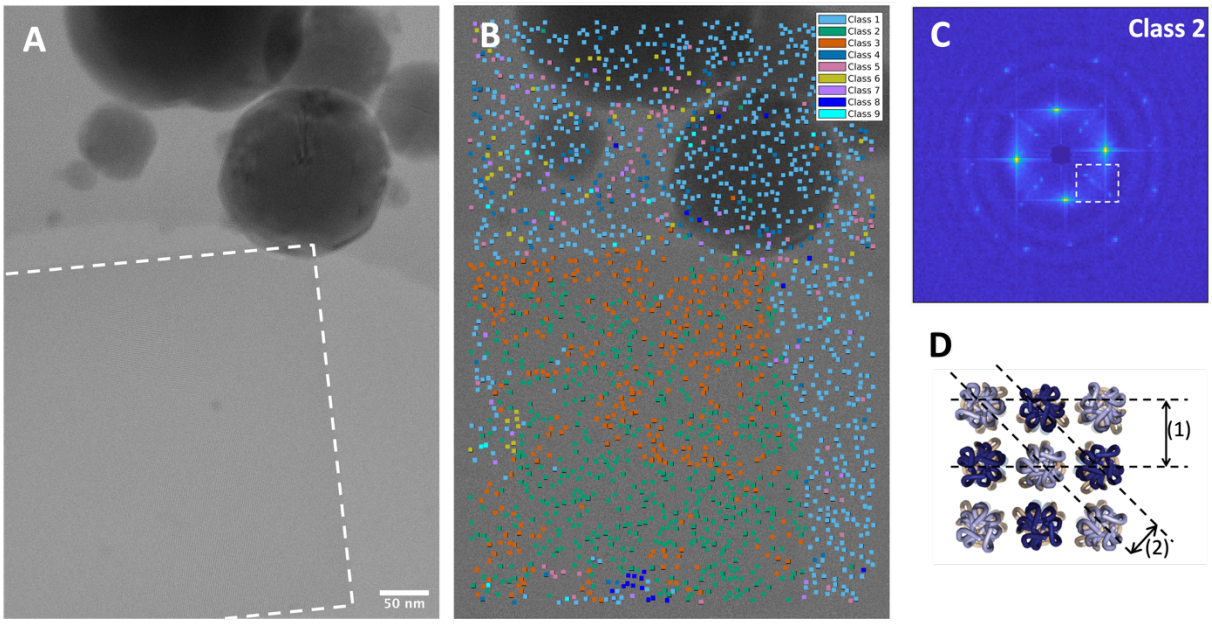


**Figure 8.** FFT analysis of patches sampled from a cryo-TEM micrograph. (A) Cryo-TEM image, where the boxed area marks the location of the nanosheet. (B) Patches that are classified into different classes. Class 2 and 3 are positioned on the nanosheet (C) Averaged patch FFT from class

2 showing double-peak pattern in the 45° direction, which corresponds to *d*-spacing (2) in the assembly model in (D).

Looking more closely at the arrangement of individual triple helices in a nanosheet, we can identify some stressed areas where the triple-helical rows are bending (Figure 9). Although it seems that these distortions are more common in one direction, because of the limited resolution of the image, it is uncertain whether that is the only direction where stress can be found.

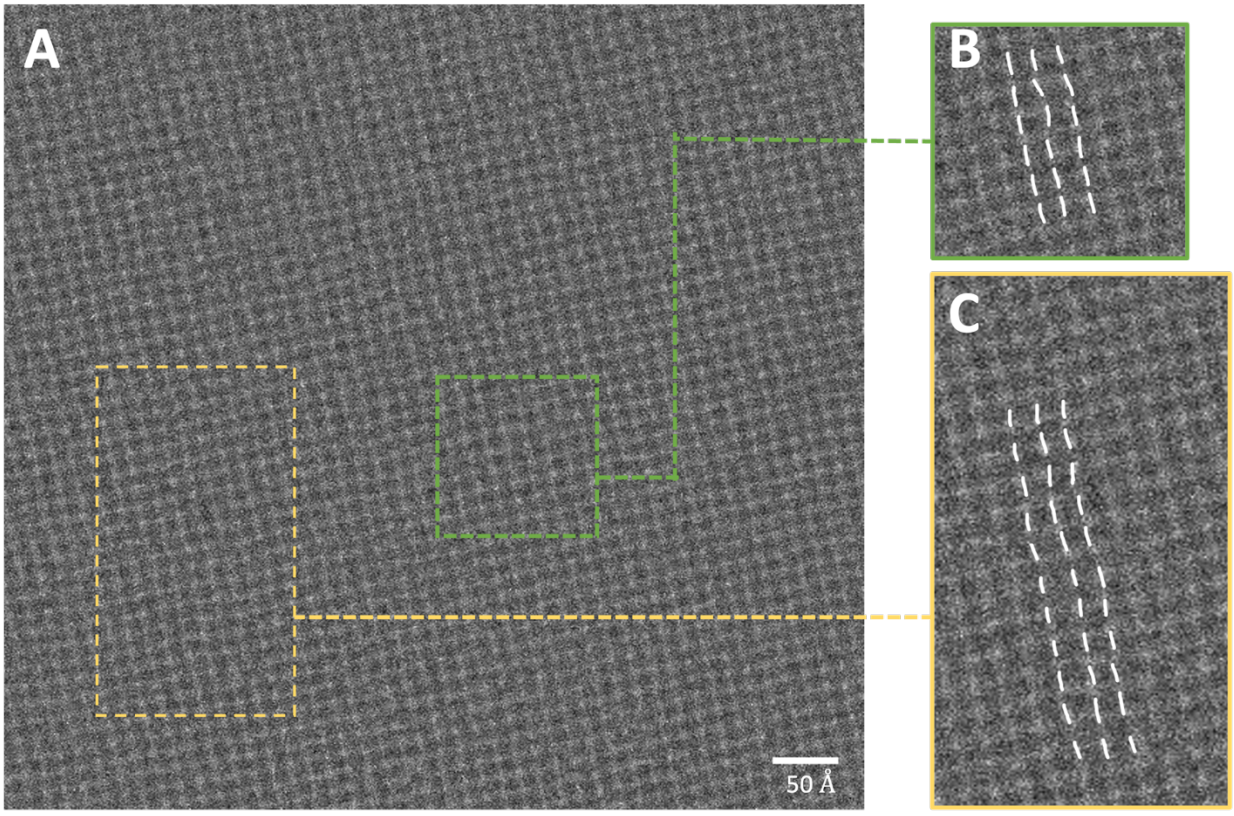


**Figure 9.** Stressed areas in the tetragonal lattice of CMP triple helices, as defined by the bending of the triple-helical rows. (A) Cryo-TEM image showing the arrangement of individual triple helices, dashed boxes indicate stressed areas. Enlarged image of (B) stress area marked by green box and (C) stressed area marked by yellow box.

In the previous study on core-shell structure, stress was also commonly observed at the core-shell interface to alleviate elastic strain associated with the lattice mismatch between two peptides. As a result, FFTs of the $4S(X)_{444}$ shell collected at positions bordering the $4R(X)_{444}$ core revealed a greater degree of disorder, as defined by a lack of sharpness of Bragg spots, as compared to FFTs of the shell region further away (Figure 10). However, these stresses did not give rise to an additional peak in the FFT like what is detected in the $4S(X)_{444}$ – $4S(X)_{454}$ mixed nanosheets.

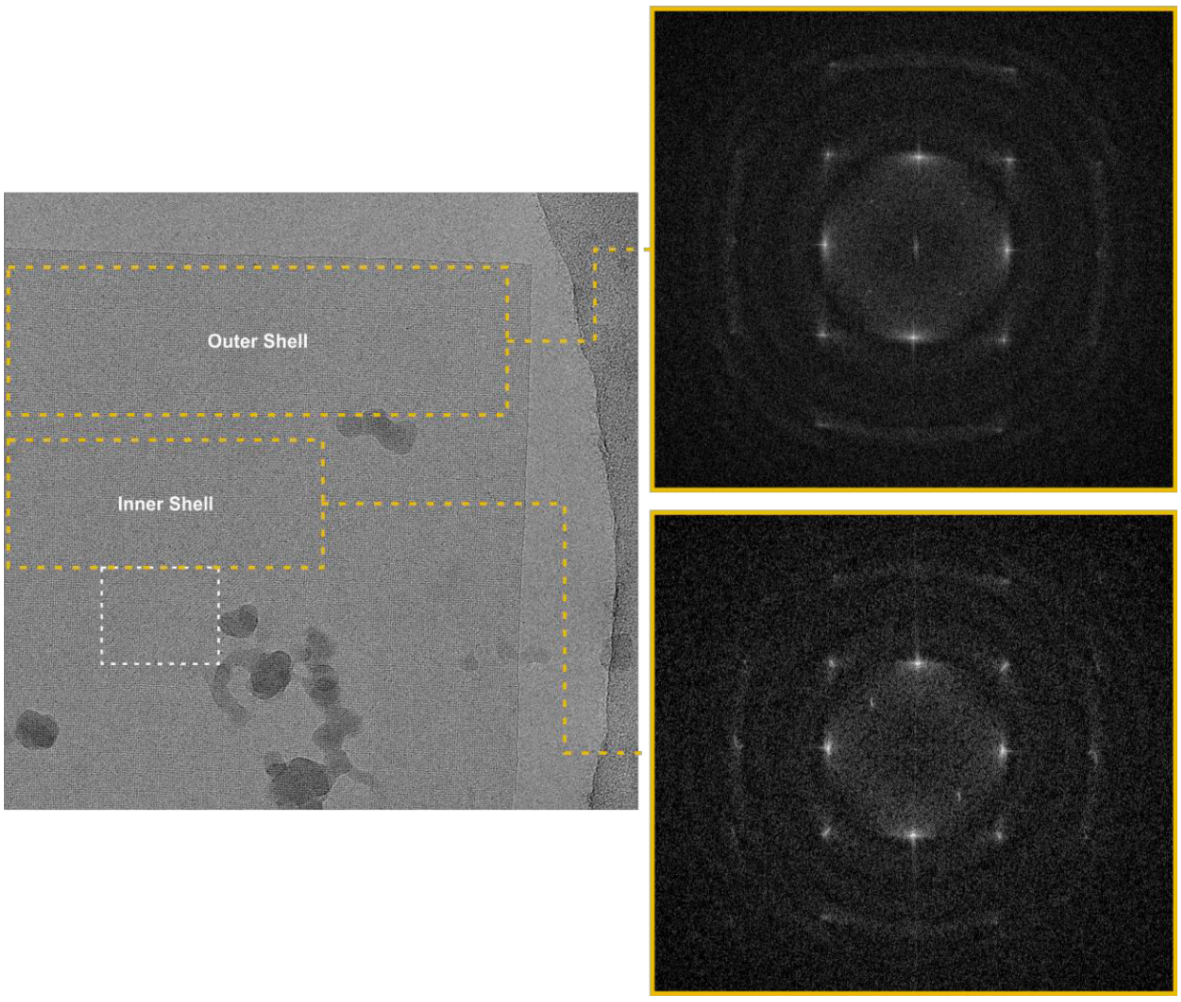


**Figure 10.** FFTs of different regions within the shell sector of the $4R(X)_{444}$@$4S(X)_{444}$ nanosheet. White dashed box indicates the location of the core sector. Adapted from Merg et al.[3]

In the core-shell structure, the $4R(X)_{444}$ core was pre-assembled and used as the template for heteroepitaxial growth of $4S(X)_{444}$ shell. On the other hand, our mixed assemblies involve the mixing of unassembled $4S(X)_{444}$ and $4S(X)_{454}$ peptide solutions and annealing them together. This should allow for random association of the two CMP triple helices to pack into the 2D tetragonal lattice. Since the lattice mismatch between $4S(X)_{444}$ and $4S(X)_{454}$ is ~3%, similar to the mismatch between $4R(X)_{444}$ and $4S(X)_{444}$, it is expected that there would also be defects in the $4S(X)_{444}$ - $4S(X)_{454}$ crystal to alleviate the elastic strain. In the cryo-TEM images of 50% $4S(X)_{444}$ – 50% $4S(X)_{454}$ mixed nanosheets, FFTs of such a small patch size of ~33 nm x 33 nm still exhibit the double-peak pattern. This implies that the stress in the lattice could have become a regular factor. Instead of maintaining their own internal structures like in the core-shell construct, the two CMP triple helices probably assemble into a slightly distorted tetragonal lattice that is different from the lattices of the individual CMPs. A possibility is that the distance between two adjacent triple helices stays consistent, but the spacing between every other triple helix in the (111) plane can vary (Figure 11).

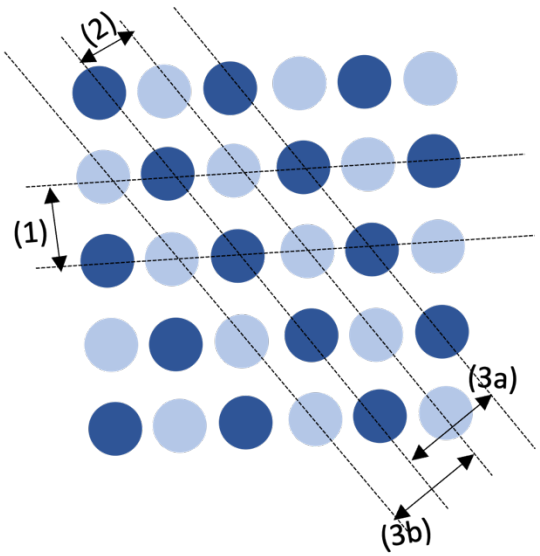

**Figure 11.** A possible model for the arrangement of CMP triple helices in the $4S(X)_{444} – 4S(X)_{454}$ mixed nanosheets. *d*-spacings (1) and (2) are consistent across the structure, but (3a) and (3b) can be different from each other.

## 2.4. Conclusion and outlook

In conclusion, we present a general strategy for the controlled fabrication of two-component 2D nanosheets, which comprises the simple mixing and co-annealing of two CMPs with compatible lattice parameters. The properties of the resultant nanosheets including lateral dimensions, thickness, and thermal stability are tunable by varying the mixing ratios between the two peptides. The underlying lattice for these mixed assemblies is different from what was observed for our previous multicomponent, core-shell nanosheets. Instead of forming single-component domains and maintaining their intrinsic lattices, the two CMPs are associating and randomly distributed across the whole structure. The lattice distortions arising from lattice mismatch between two CMPs seem to follow a specific pattern that is reflected in the FFT analysis.

A possible explanation for the presence of double-peak pattern in the FFTs is the formation of a slightly distorted tetragonal lattice that is distinct from the lattices of single-component systems. It would be helpful if we could improve the quality of cryo-TEM micrographs for better visualization of the stress in the crystal, hence confirming whether the lattice distortions indeed follow a pattern. Furthermore, it would be interesting to model different arrangements of the 2D lattice to see if the FFT pattern can be replicated. If the crystal defects are predictable and programmable, that would represent an advanced structural control of 2D assemblies.

## 2.5. Supplementary figures

**Table S1.** Diagonal length measured for $4S(X)_{444}$ – $4S(X)_{454}$ nanosheets assembled at 4 ℃ and at RT

| Diagonal length (nm) | 4 ℃ | | RT | |
|---|---|---|---|---|
| | 1 week | 2 weeks | 1 week | 2 weeks |
| 100% 444 | 1491±272 | Sheets broke | Not forming sheets | Not forming sheets |
| 75% 444 | 1034±135 | 1054±130 | 897±93 | 1066±333 |
| 50% 444 | 663±103 | 682±113 | 586±108 | 712±128 |
| 25% 444 | N/A | N/A | 508±101 | 566±93 |
| 100% 454 | N/A | N/A | 383±94 | 432±101 |

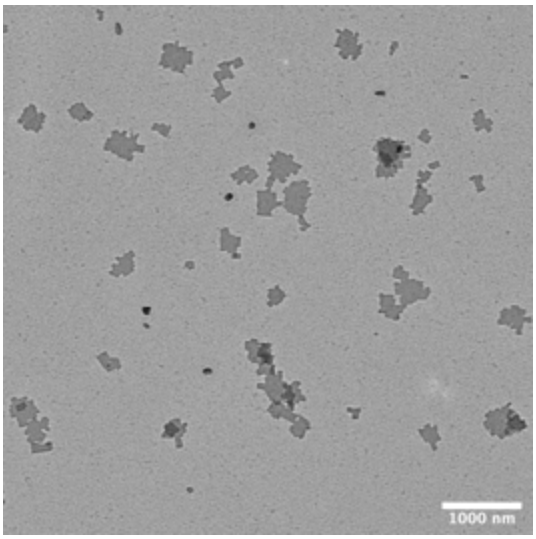


**Figure S1.** TEM image of 10% $4S(X)_{444}$ – 90% $4S(X)_{454}$ nanosheet assembled at 4 mg/mL, incubated at 4 ℃

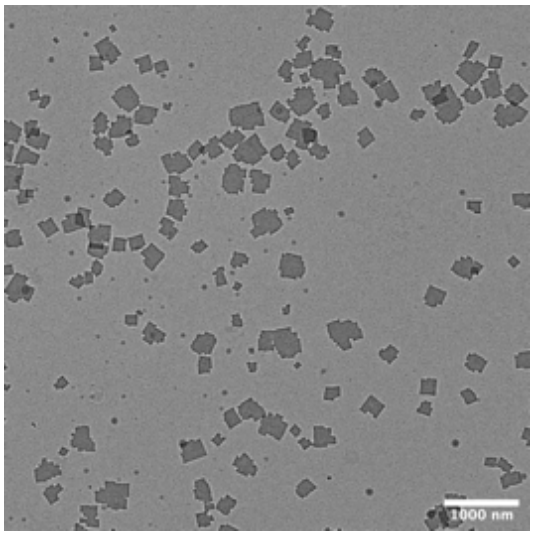


**Figure S2**.TEM image of pure $4S(X)_{454}$ nanosheets assembled at 4 mg/mL, incubated at 15 ℃.

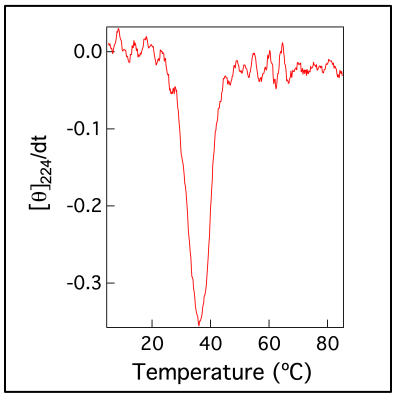


**Figure S3**. First derivative of the CD signal at 224 nm as a function of temperature for pure $4S(X)_{454}$ nanosheets assembled at 4 mg/mL, incubated at 15 ℃.

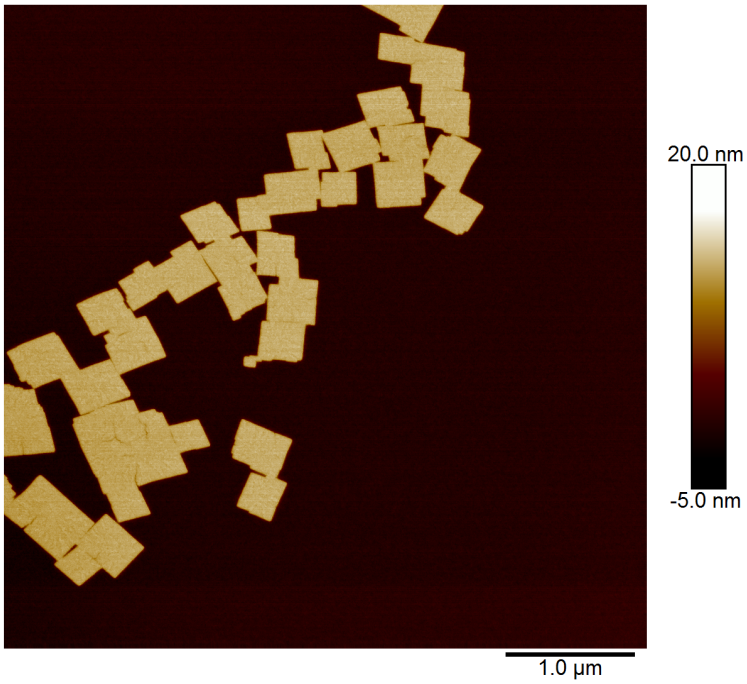


**Figure S4**. AFM image of $4S(X)_{454}$ nanosheets assembled at RT

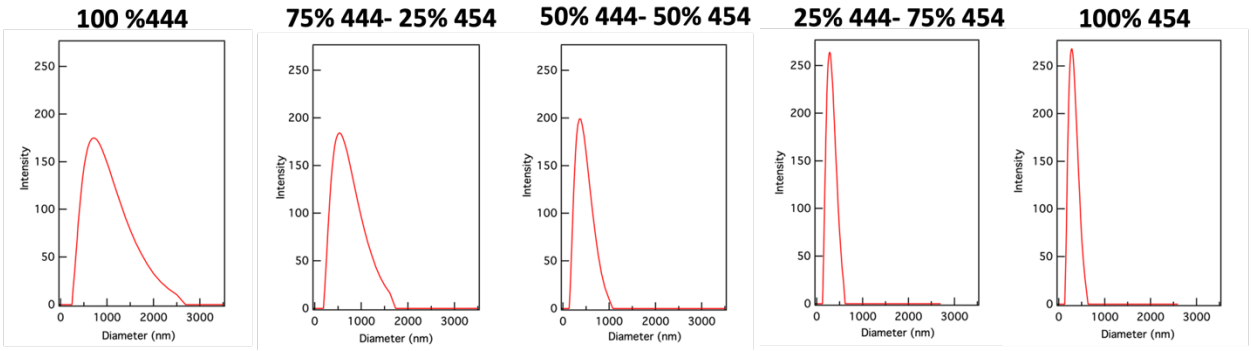


**Figure S5.** DLS measurements for $4S(X)_{444}$ – $4S(X)_{454}$ mixed assemblies assembled at 15 ℃. The average peak measured for 100% $4S(X)_{444}$ sheets is 697 nm, for 75% $4S(X)_{444}$ – 25% $4S(X)_{454}$ is 510 nm, for 50% $4S(X)_{444}$ – 50% $4S(X)_{454}$ is 327 nm, for 25% $4S(X)_{444}$ – 75% $4S(X)_{454}$ is 278 nm, and for 100% $4S(X)_{444}$ is 278 nm.

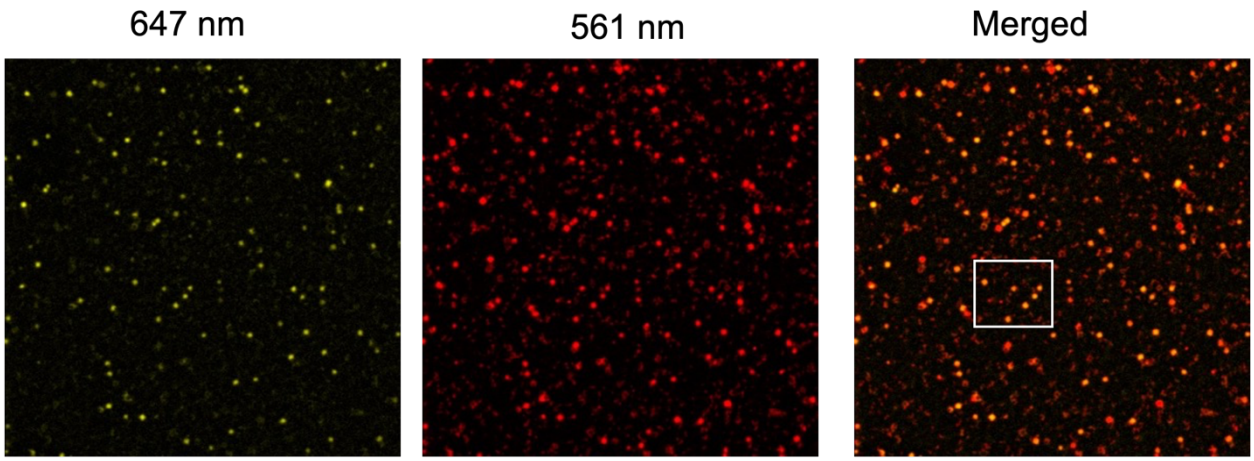


**Figure S6.** Fluorescence optical micrographs of 75% $4S(X)_{444}$ – 25% $4S(X)_{454}$ nanosheets labelled with AF647 and Cy3B at different emission wavelengths. The expanded view of the boxed section in the merged channel is presented in Figure 4.

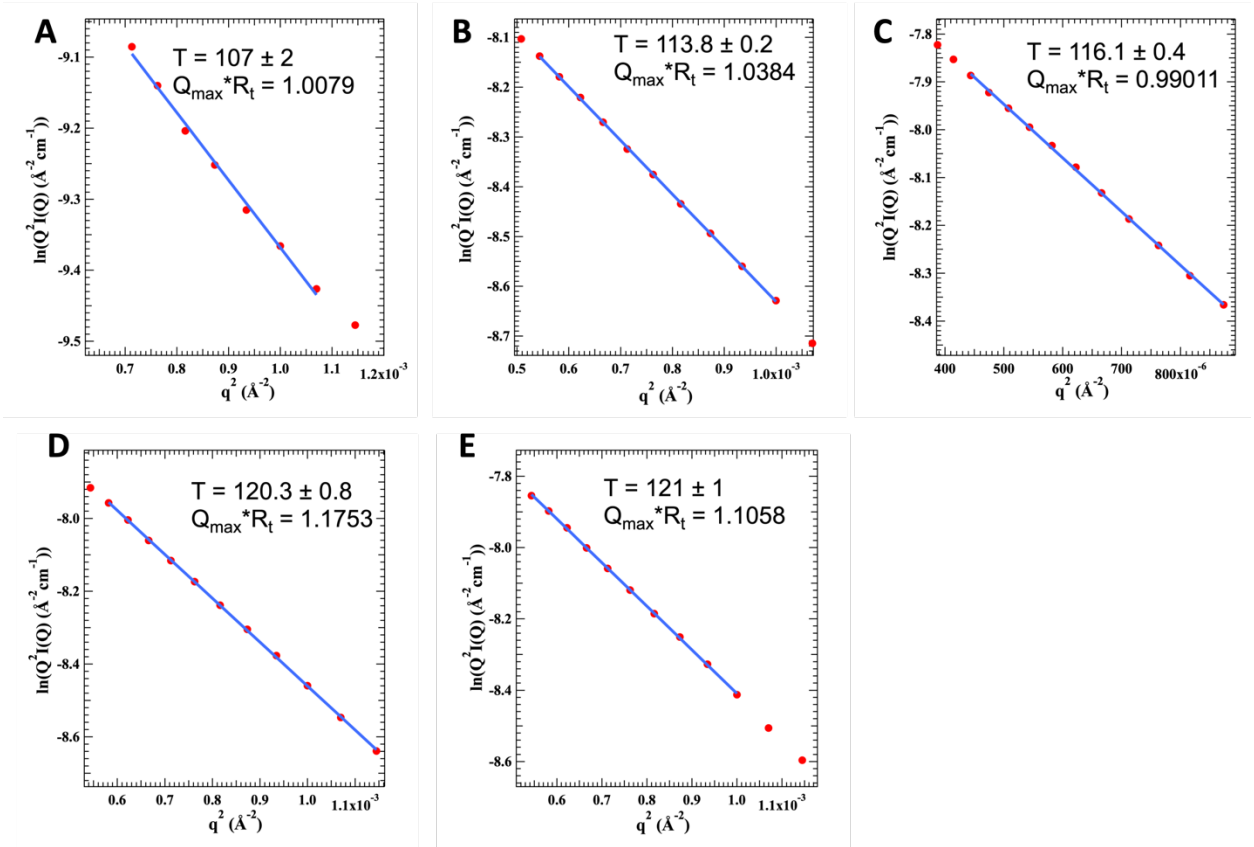

**Figure S7.** Modified Guinier plot with fit for sheet-like forms. Nanosheets are assembled from (A) 100% $4S(X)_{444}$, (B) 75% $4S(X)_{444}$ – 25% $4S(X)_{454}$, (C) 50% $4S(X)_{444}$ – 50% $4S(X)_{454}$, (D) 25% $4S(X)_{444}$ – 75% $4S(X)_{454}$, (E) 100% $4S(X)_{454}$

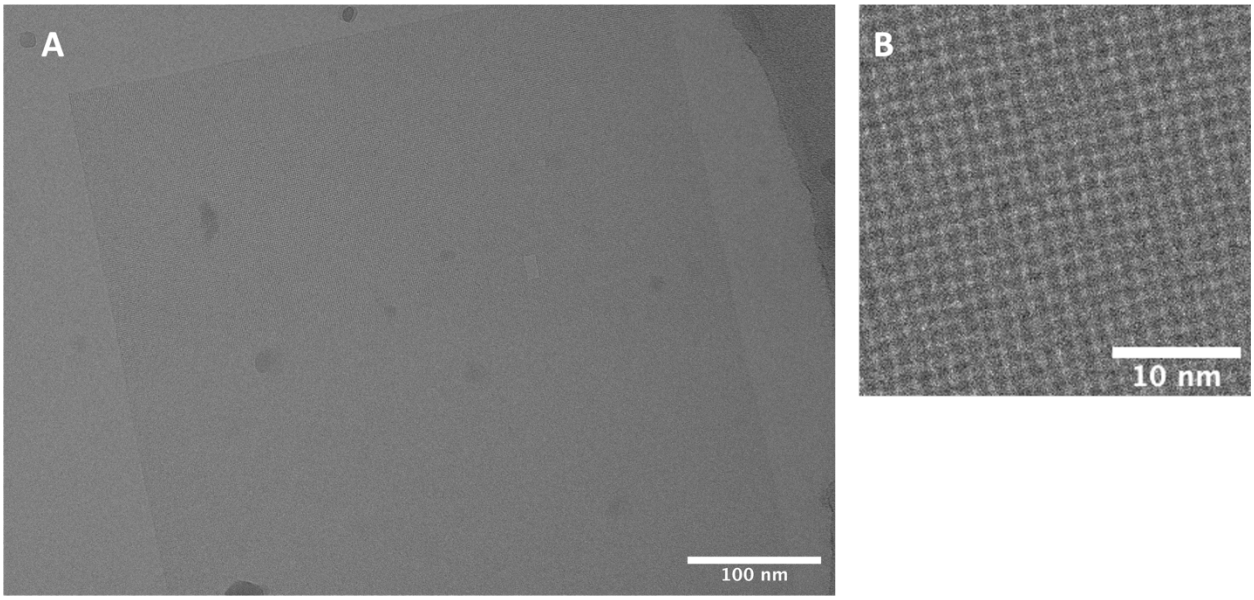


**Figure S8.** (A) Cryo-TEM image of a 50% $4S(X)_{444}$ – 50% $4S(X)_{454}$ nanosheet, (B) Enlarged image of the nanosheet reveals tetragonal arrangement of CMP triple helices

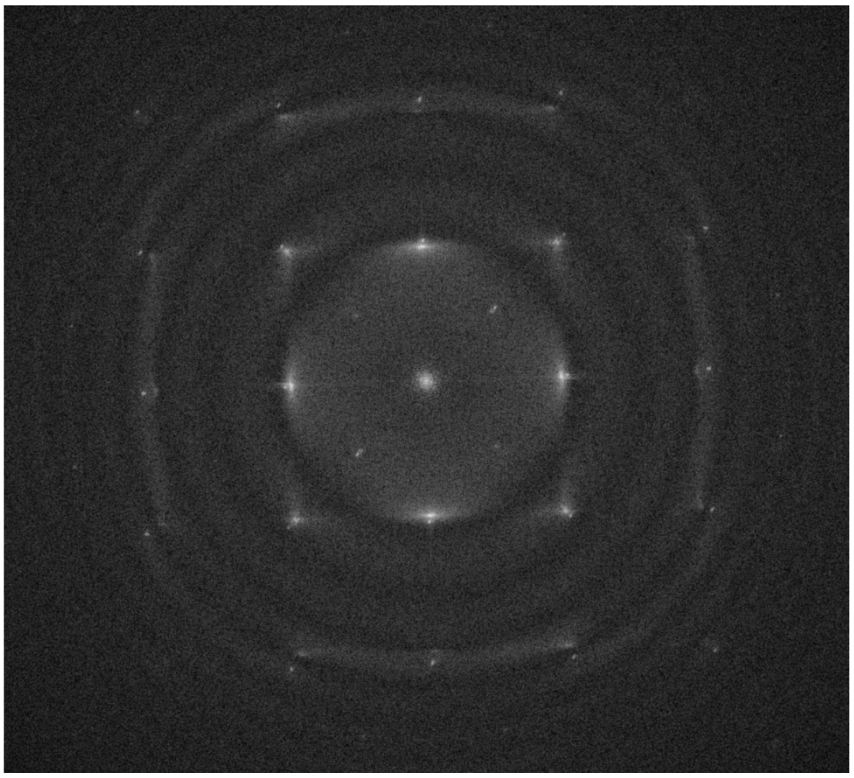

**Figure S9.** FFT of a multicomponent core-shell nanosheet. Two sets of Bragg spots are observed indicating the presence of two unique crystal lattices. Adapted from Merg et al.[3]

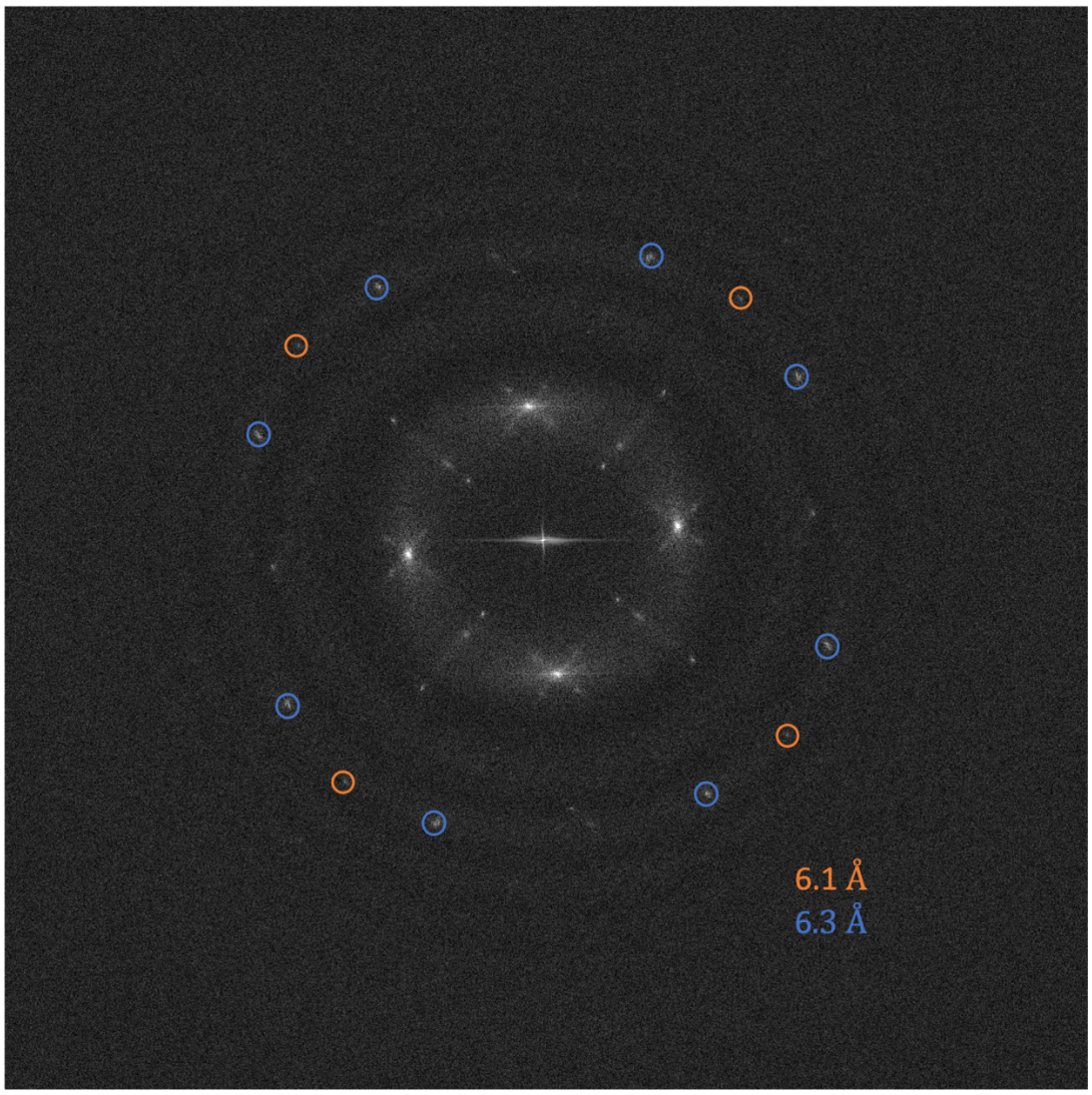


**Figure S10.** FFT of the nanosheet in Figure 23, with Bragg spots that extend to a resolution of 6.1 Å.

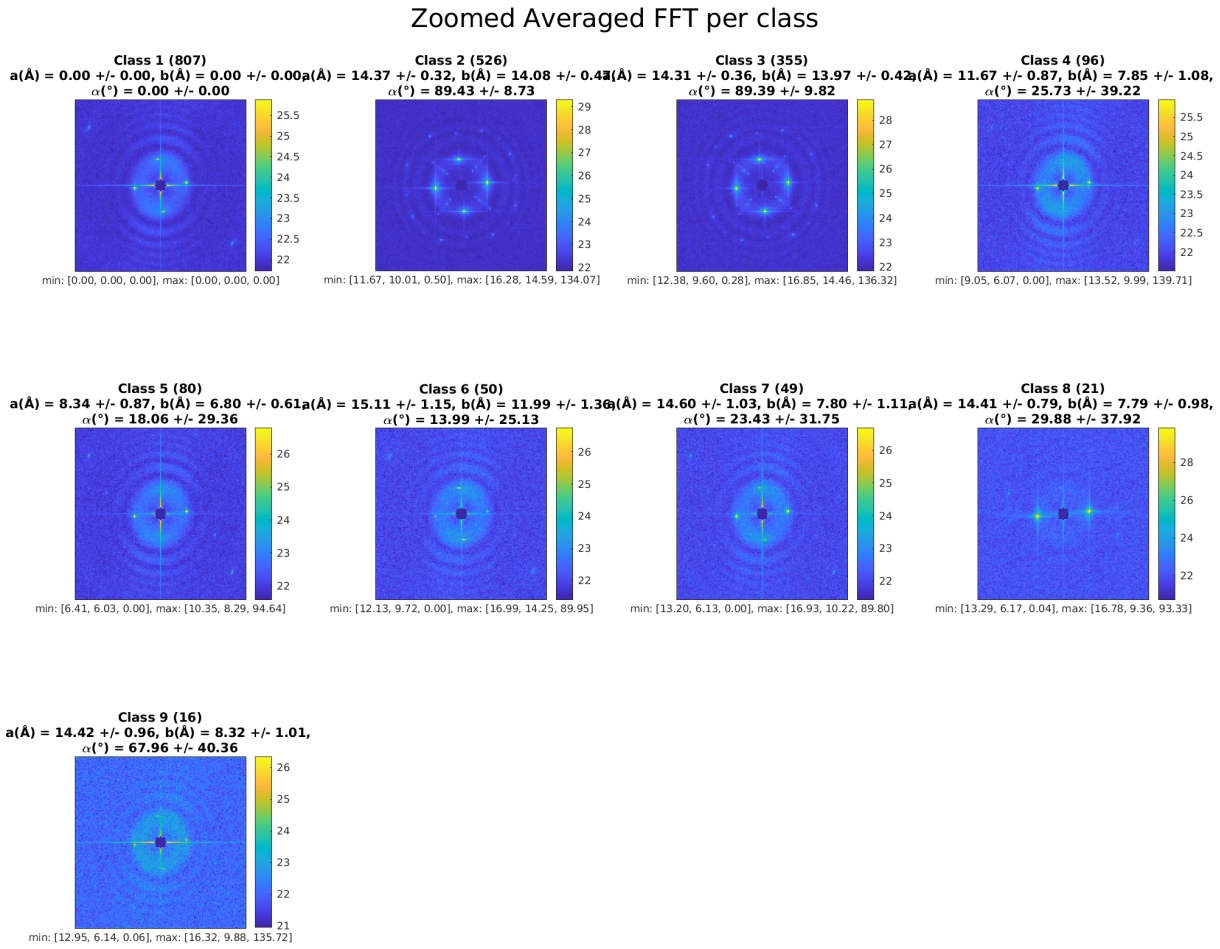


**Figure S11.** Averaged FFT from all classes found on the cryo-TEM image from figure 24.

| | Double-peak | Single-peak | Multiple sheets | Uncertain | Total |
|---|---|---|---|---|---|
| # Images | 54 | 12 | 4 | 35 | 105 |
| Percent | 82% | 18% | | | |

**Figure S12.** Analysis of the FFTs of all nanosheets collected from cryo-TEM. "Double-peak" refers to images with patch FFT showing two set of Bragg spots, while "single-peak" has only one set. "Multiple sheets" refers to the presence of two or more nanosheets in a single image.

"Uncertain" refers to images where the resolution is not good enough to obtain well-resolved FFT pattern.

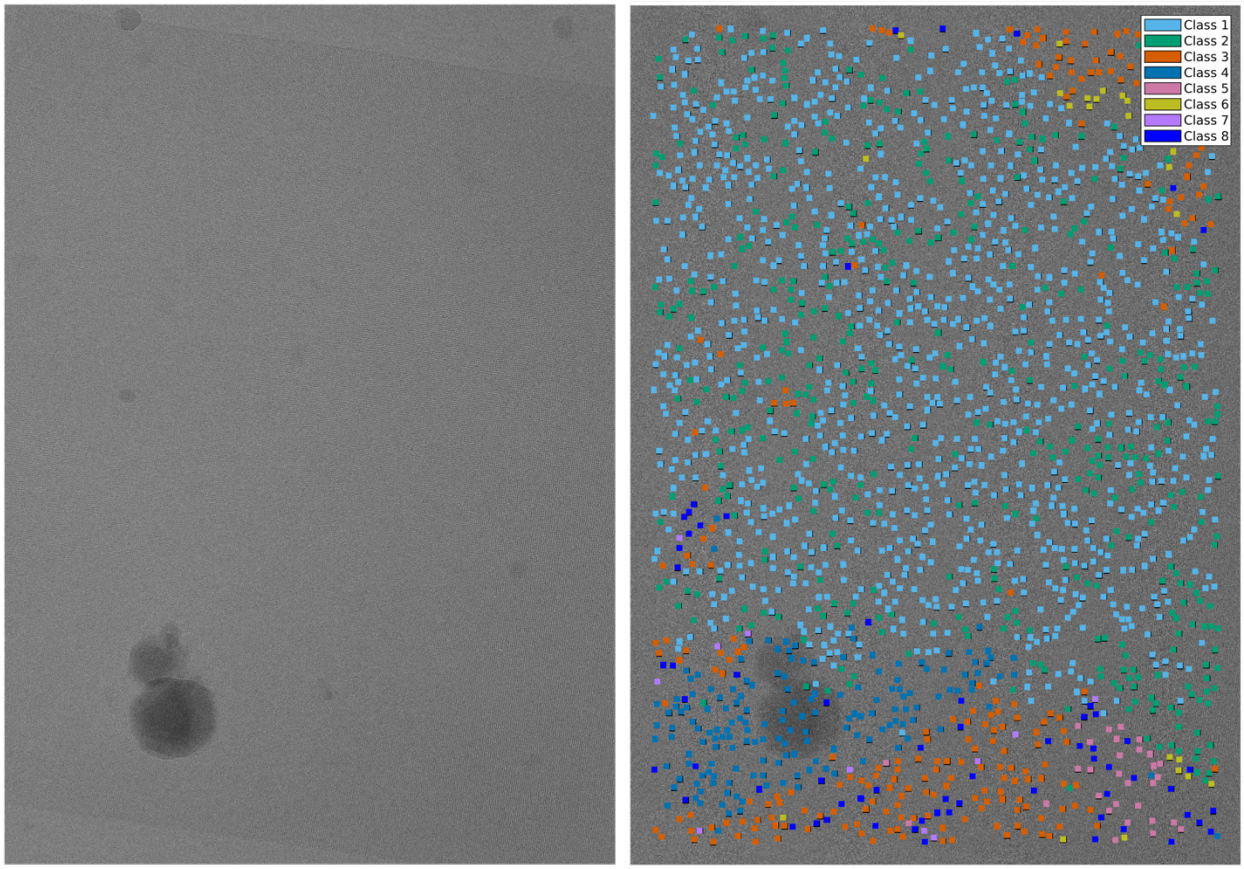


**Figure S13.** Cryo-TEM image of another 50% $4S(X)_{444}$ – 50% $4S(X)_{454}$ mixed sheet and its classification result. Class 1 and 2 represent patches in the region of the nanosheet.

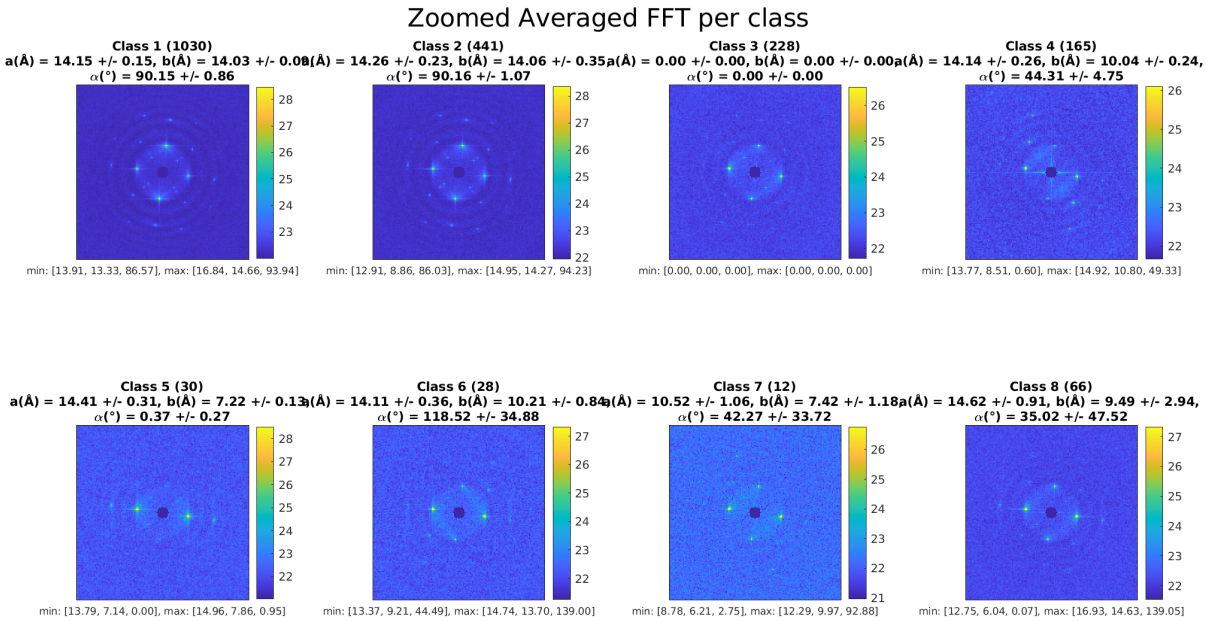


**Figure S14.** Corresponding FFTs to the classes in Figure S12. Class 1 and 2 represent the patches in the area of the nanosheet and both display the double-peak pattern.

## 2.6. Experimental methods

### Peptide synthesis and purification

Peptides were prepared using microwave-assisted synthesis on a CEM Liberty Blue automated microwave peptide synthesizer and Fmoc-Gly-HMP-Tentagel resin. Standard Fmoc protection chemistry was employed with coupling cycles based on DIC/Oxyma-mediated activation protocols and based-induced deprotection (20% piperidine in DMF) of the Fmoc group. For the biotinylated and azido-modified peptides, biotin-PEG2-acid and azido-PEG5-acid were used to cap the N-terminus of the peptide while it was stilled attached to the resin (no final deprotection step). After coupling, the DMF/resin mixture was filtered and rinsed with acetone and then air-dried. The crude peptides were cleaved for 3 hours with a cleavage solution consisting of 92.5% TFA/ 2.5% $H_2O$/ 2.5% DODT/ 2.5% TIS (TFA = trifluoroacetic acid, DODT = 3,6-Dioxa-1,8-octane-dithiol, TIS = Triisopropylsilane). After filtration, the crude peptide product in TFA was precipitated with cold ethanol and centrifuged at 4 ℃. The supernatants were discarded, and the pellets were dried under vacuum overnight.

Crude peptides were purified using a Shimadzu LC-20AP reverse-phase high-performance liquid chromatography (HPLC) instrument equipped with a preparative scale C18 column. Peptides were eluted with a linear gradient of water-acetonitrile with 0.1% TFA. The target fractions were collected and lyophilized. The lyophilized peptide was repurified via HPLC under the same protocol described above and lyophilized. Doubly pure peptides were dialyzed against HPLC-grade $H_2O$ to remove residual TFA (MWCO = 2000 Da). The resulting peptide solutions were lyophilized and stored at -30 ℃.

**Nanosheet assembly experiment**

Annealing experiments were conducted using a BioRad T-100 thermal cycler. The annealing protocol consisted of heating peptide solutions to 90 ℃ for 15 min, followed by slow cooling to 15 ℃ (1 ℃/5 min rate). To assemble the nanosheets, each pure peptide was dissolved in 20 mM 3-(N-morpholino)propanesulfonic acid (MOPS) buffer (pH 7.0) to a final concentration of 4 mg/mL. Single component nanosheets were assembled by annealing each pure peptide solution separately. The blended nanosheet assemblies were conducted by mixing the two peptide solutions in designated volume ratios (75:25, 50:50, and 25:75) such that the final mixture concentration remained 4 mg/mL. Mixed peptide solutions were then annealed 90 to 15 ℃. All assemblies were allowed to sit at room temperature for 2 weeks.

**Transmission electron microscopy**

TEM specimens were prepared by briefly mixing 2.5 $\mu$L of peptide nanosheet solution with 2.5 $\mu$L of aqueous uranyl acetate stain solution (1%) directly on a 200-mesh carbon coated copper grid from Electron Microscopy Services. After 30 s, the excess liquid was wicked away and the grids were air-dried. Electron micrographs were recorded on a Hitachi HT-7700 TEM with a tungsten filament and AMT CCD camera at an accelerating voltage of 80 kV.

**Circular dichroism spectropolarimetry**

CD measurements were conducted on a Jasco-1500 CD spectropolarimeter. These spectra were recorded and averaged from 260 to 190 nm at a scanning rate of 100 nm/min and a bandwidth of 2 nm. CD melting experiments were conducted with a 0.1 mm path length quartz cuvette from

Hellma USA Inc., in the temperature range from 5 to 85 ℃ at a heating rate of 20 ℃/h. The intensity of the CD signal at 224 nm was monitored as a function of temperature.

**Atomic force microscopy**

AFM images were collected with a Bruker Multimode 8 atomic force microscope using peak force tapping mode in air. Images were obtained using SCANASYST-AIR probe from Bruker with a spring constant of 0.4 N/m and a resonance frequency of 70 kHz. Samples were prepared by diluting 5 $\mu$L of nanosheet solution with 20 $\mu$L of HPLC-grade $H_2O$. The diluted solution was centrifuged at 3000 g for 10 min. The supernatant was removed and replaced with 5-30 $\mu$L of HPLC-grade $H_2O$ (depending on how concentrated the sample was). Subsequently, 5 $\mu$L of the re-suspended sample was drop-casted onto freshly cleaved mica and air-dried.

**Fluorescence labelling of the nanosheets**

The 90% $4S(X)_{444}$ – 10% $4S(X)_{454}$ mixture solution (mixture 1) were prepared from 85.5% $4S(X)_{444}$/ 4.5% b-$4S(X)_{444}$/ 7.5% $4S(X)_{454}$/2.5 % $N_3$-$4S(X)_{454}$. The 75% $4S(X)_{444}$ – 25% $4S(X)_{454}$ mixture solution (mixture 2) were prepared from 71.25% $4S(X)_{444}$/ 3.75% b-$4S(X)_{444}$/ 18.75% $4S(X)_{454}$/6.25% $N_3$-$4S(X)_{454}$. The samples were then annealed and incubated for two weeks at 15 ℃. Subsequently, AF647-DBCO (0.5 $\mu$L, 1 mg/mL solution in water) and Cy3B-SA (1 mg/mL solution in water, 5 $\mu$L used for mixture 1, 10 $\mu$L used for mixture 2) were added to a 10 $\mu$L solution of nanosheets. The mixtures were then further diluted with 10 $\mu$L MOPS buffer (20 mM, pH 7) and incubated for 1 h at room temperature in the dark. The solution was placed in the refrigerator overnight (4 ℃). The next day, the solution was centrifuged at 3500g for 10 min. The

supernatant was removed and replaced with fresh 20 mM MOPS buffer (pH 7.0) and the sample was vortex mixed.

**Fluorescence optical microscopy**

The Nikon Eclipse Ti microscope was equipped with an Intensilight epifluorescence source, a CFI Apo 100X NA 1.49 objective, and a TIRF launcher with three laser lines: 488 nm (10 mW), 561 nm (50 mW), and 638 nm (20 mW). All reported experiments were performed using the Quad Cube (cat. #97327) and TRITC (cat. # 96321) filter cube set supplied by Chroma.

Experiments were conducted using no. 1.5 glass sildes (25 x 75 mm) that were cleaned by sonication in Milli-Q (18.2 MΩ/cm) water for 15 min, followed by a second sonication in 200 proof ethanol for 15 min, and then dried under a stream of $N_2$. The slides were etched with piranha solution (**Caution**: since Piranha solution ($H_2SO_4$/30% $H_2O_2$, 7:3) reacts violently with many organic compounds, extreme care must be taken when handling it) for 30 min to remove residual organic material and activate hydroxyl groups on the surface. The cleaned substrates were rinsed with Milli-Q water in a 200 mL beaker at least six times and further washed with ethanol three times. Slides were then transferred to a 200 mL beaker containing 2% (3-aminopropyl)triethoxysilane (APTES) in ethanol for 1 h and then washed with ethanol three times and thermally cured in an oven (~ 110 ºC) for 1- min, The APTES-functionalized slides were mounted to a custom-made 30-well microfluidic chamber fabricated from Delrin (McMasterCarr, cat. #8573K15). The nanosheet solution was added (10 $\mu$L) to the well and was immediately subjected to a wash (3 x 100 $\mu$L) with 20 mM MOPS buffer (pH 7.0). Assembly location was determined using RICM imaging. After focusing using RICM, wide-field epifluorescence micrographs were acquired.

**Small-angle/Wide-angle X-ray scattering measurements**

Synchrotron SAXS/WAXS measurements were performed at the 12-ID-B beamline of the Advanced Photon Source at Argonne National Laboratory. The sample-to-detector distances were set such that the overall scattering momentum transfer, $q$, range was achieved from 0.005 to 0.9 $Å^{-1}$, where $q = 4\pi \sin \theta/\lambda$, with 2 $\theta$ denoting the scattering angle and $\lambda$ denoting the X-ray wavelength. The wavelength was set at 0.9322 Å during the measurements. Scattered X-ray intensities were measured using a Pilatus 2 M (DECTRIS Ltd.) detector. Measurements were conducted on aqueous solutions of CMP nanosheets at a concentration of 4 mg/mL in 20 mM MOPS buffer (pH 7.0) at 5 ºC. A quartz capillary flow cell (1.5 mm diameter) was employed to prevent radiation damage. The 2D scattering images were converted to 1D scattering curves through azimuthal averaging after solid angle correction and then normalizing with the intensity of the transmitted X-ray beam using the software package at beamline 12-ID-B. The 1D curves of the samples were averaged and subtracted with the background measured from the corresponding buffers.

**Cryogenic transmission electron microscopy**

3 $\mu$L of sample was pipetted onto a glow-discharged QuantiFoil grid 1.2 (300 mesh). Grids were blotted for 2 s with no blot force and plunge-frozen in liquid ethane using a Vitrobot with the environmental chamber set at 100% humidity. Data were acquired on a Thermo Fisher Talos Arctica electron microscope at 200 keV in nanoprobe mode, with a GIF Quantum LS Imaging filter (20 eV slit in width) and a Gatan K3 electron counting direct detection camera.

Data sets at zero tilt were collected at nominal magnifications of 79K, resulting in calibrated pixel sizes of 1.08 Å. The defocus was set at 3 $\mu$m. Every position was selected manually

by the observation of crystal-like features, and each of these positions was exposed by recording a 4 s movie with 48 frames totaling ~37 $e^{-}/\text{Å}^{2}$. Beam-induced motion was automatically corrected in Digital Micrograph (Gatan).

**2.7. References**

(1) Merg, A. D.; Touponse, G.; van Genderen, E.; Zuo, X.; Bazrafshan, A.; Blum, T.; Hughes, S.; Salaita, K.; Abrahams, J. P.; Conticello, V. P. 2D Crystal Engineering of Nanosheets Assembled from Helical Peptide Building Blocks. *Angew Chem Int Ed Engl* **2019**, *58* (38), 13507-13512. DOI: 10.1002/anie.201906214.

(2) Okuyama, K. Revisiting the molecular structure of collagen. *Connect Tissue Res* **2008**, *49* (5), 299-310. DOI: 10.1080/03008200802325110.

(3) Jiang, T.; Xu, C.; Zuo, X.; Conticello, V. P. Structurally homogeneous nanosheets from self-assembly of a collagen-mimetic peptide. *Angew Chem Int Ed Engl* **2014**, *53* (32), 8367-8371. DOI: 10.1002/anie.201403780.

(4) Merg, A. D.; van Genderen, E.; Bazrafshan, A.; Su, H.; Zuo, X.; Touponse, G.; Blum, T. B.; Salaita, K.; Abrahams, J. P.; Conticello, V. P. Seeded Heteroepitaxial Growth of Crystallizable Collagen Triple Helices: Engineering Multifunctional Two-Dimensional Core-Shell Nanostructures. *J Am Chem Soc* **2019**, *141* (51), 20107-20117. DOI: 10.1021/jacs.9b09335.

(5) Kreutzberger, M. A. B.; Wang, S.; Beltran, L. C.; Tuachi, A.; Zuo, X.; Egelman, E. H.; Conticello, V. P. Phenol-soluble modulins PSMalpha3 and PSMbeta2 form nanotubes that are cross-alpha amyloids. *Proc Natl Acad Sci U S A* **2022**, *119* (20), e2121586119. DOI: 10.1073/pnas.2121586119 From NLM Medline.

# Chapter 3. Self-assemblies of homochiral and heterochiral $\beta$-strand mimetic peptides

*Acknowledgement to LiX beamline:*

*The LiX beamline is part of the Center for BioMolecular Structure (CBMS), which is primarily supported by the National Institutes of Health, National Institute of General Medical Sciences (NIGMS) through a P30 Grant (P30GM133893), and by the DOE Office of Biological and Environmental Research (KP1605010). LiX also received additional support from NIH Grant S10 OD012331. As part of NSLS-II, a national user facility at Brookhaven National Laboratory, work performed at the CBMS is supported in part by the U.S. Department of Energy, Office of Science, Office of Basic Energy Sciences Program under contract number DE-SC0012704.*

## 3.1 Introduction

In the previous chapters, we have reported on the design of collagen mimetic peptides (CMPs) that self-assemble into crystalline nanosheets. CMP sequences comprise three sequential blocks of positively charged, neutral, and negatively charged triads. The peptides then fold into triple helices, which serve as rigid, rod-like building blocks. The electrostatic interaction between oppositely charged residues on adjacent triple helical units drives their packing into 2D crystal lattices. This straightforward scheme facilitates the formation of structurally defined 2D assemblies, which serve as an ideal platform for studying how tuning the structural properties of

the helical building blocks influences the internal packing and overall assembly architecture.[1, 2] Inspired by the relatively simple construct of CMPs, we aim to expand our design strategy to study the self-assemblies of electrostatically self-complementary peptides derived from other structural motifs.

A potential candidate is $\beta$-strand mimetic peptide (BMP) based on sequence patterns that should favor $\beta$-strand formation. In analogy to CMPs, the sequence design for BMPs is also composed of two end blocks with charged residues and a midblock that consists of a hydrophobic core. The composition of the BMP core sequence is derived from phenylalanines, which have been demonstrated to drive $\beta$-sheet self-assembly even for peptide sequences having only two Phe residues.[34, 35] For our initial investigation, we choose to study a basic sequence K2F4E2 (Figure 1).

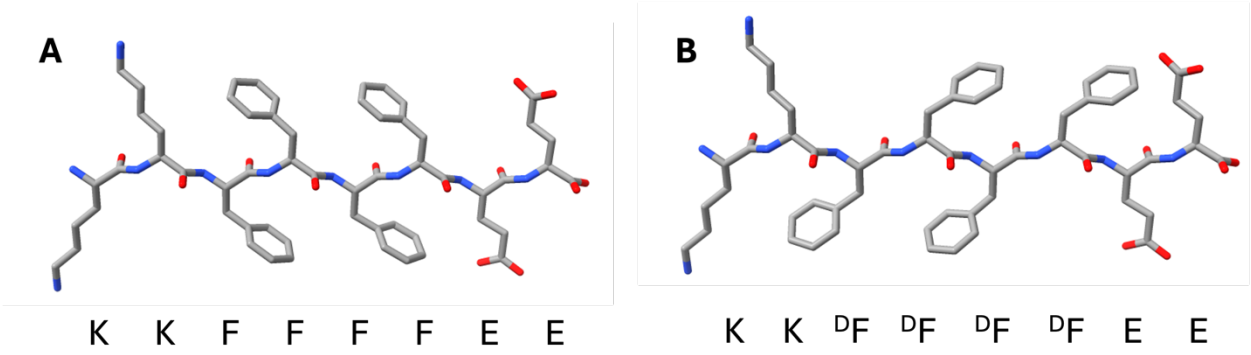


**Figure 1.** Structures of (A) Homochiral K2F4E2 and (B) block heterochiral K2($^{D}$F)4E2.

Among the strategies for regulating peptide self-assemblies, the incorporation of unnatural $_{D}$-amino acids is attracting more interest due to the many, often unexpected, effects.[36] $_{D}$-amino acids are known for their resistance against enzymatic hydrolysis and thus are expected to enhance the stability and function of the materials in biological environment.[36] At the molecular level, the incorporation of $_{D}$-amino acids can also influence the conformation of peptide secondary

structure.[36-41] Changing the chirality of just a single amino acid residue can affect the peptide assembly structures.[36, 37, 41] The substitution of $_{L}$-amino acids with their $_{D}$-enantiomers in $\beta$-turns is well known for increasing the binding affinity and/or biological stability.[36] With regards to the $\beta$-sheet structure, $_{D}$-amino acid incorporation has been reported to be capable of both distorting or promoting the peptide self-assembly.

Marchesan and coworkers addressed the chirality effects at each amino acid position on the self-assembly of a tripeptide FFV.[37] When probing the secondary structures of the assemblies with CD, all peptides exhibited the signature $\beta$-strand negative minimum or positive minimum in the region of 210-220 nm, which is expected for either $_{L}$- or $_{D}$- peptides, respectively. It should be noted that sequence with discontinuous chirality (i.e., $^{D}$FF$^{D}$V and F$^{D}$FV) displayed the weakest CD signals. With regards to the peptide self-assemblies, they found that only non-ordered nanostructures were detected in the homochiral controls (all $_{L}$- or $_{D}$- sequences). On the contrary, twisted fibers were formed from the heterochiral $^{D}$FFV and F$^{D}$FV.

Luo et al. also studied the effect of $_{D}$-amino acids on the sequence EAK16 (Ac-AEAEAKAKAEAEAKAK-$NH_2$).[38] They found that the homochiral $_{L}$- and $_{D}$- peptides self-assembled into nanofibers, while the peptide with alternating $_{D}$ - and $_{L}$ -pattern only showed non-structured aggregates. This alternating chiral configuration is thought to disrupt the typical uniform chiral backbone and interfere with the crucial non-covalent interactions, hence hindering the formation of supramolecular assembly.

Clover et al. examined another substitution pattern of $_{D}$-amino acids into the sequence of KFE8 peptide[40] In particular, a block of four consecutive residues were replaced with their $_{D}$-enantiomers. The peptide thus comprises two blocks of opposite chirality, either $_{LD}$ or $_{DL}$. They found that while the homochiral $_{LL}$ and $_{DD}$ peptides formed nanofibers, the heterochiral $_{LD}$ and $_{DL}$

analogs assembled into supramolecular helices. Molecular dynamics simulation suggested that in the $_{LD}$ analog, the amino acid backbone is unchanged while the $_{D}$-residues' side chains rotated and resulted in a kink at the $_{L}$-$_{D}$ interface. This in turn introduced an internal strain counteracting the twisting nature of the $\beta$-sheet and flattened it out more compared to the homochiral structure.

In our design of BMPs, we are also interested in studying the effect of substituting $_{D}$-enantiomers into the K2F4E2 sequence. From literature review, it appears that incorporating $_{D}$-amino acids in block pattern tends to have a more stabilizing effect on the assembly structure. Therefore, we decided to examine an analog where the four Phe residues are replaced with their $_{D}$-enantiomers (Figure 1).

### 3.2. Different secondary structure conformations and assembly morphologies between K2F4E2 and K2($^{D}$F)4E2

We first evaluate how the two peptides behave when being dissolved directly in water. Each peptide was dissolved in HPLC-grade $H_2O$ to a final concentration of 1 mg/mL. The peptides are water-soluble and measured pH's are slightly acidic (pH of 5.6 for K2F4E2 and 5.0 for K2($^{D}$F)4E2). The peptide solutions were then either annealed or unannealed. Annealed samples were heated to 90 ℃ for 30 min, followed by slow cooling to 25 ℃. Unannealed samples were kept at RT. Characterization of the assemblies by CD and negative stain TEM after 1 day and 1 week returned similar results. The K2F4E2 peptide when annealed forms large, short tapes that tend to aggregate (Figure 2A). The unannealed sample probably forms some twisted filaments and some thin tapes (very few assemblies found, and TEM resolution is limited, Figure 2B). The assemblies from K2F4E2, either annealed or unannealed, give weak CD signal that resembles random coils (Figure

2C). Compared to K2F4E2, the heterochiral K2($^{D}$F)4E2 assembles more readily. In annealed sample, straight tapes of various widths along with some nanotubes are observed (Figure 2D, Figure S1). The unannealed sample displays a formation of mostly nanotubes that appear uniform in size (Figure 2F). With regards to the CD spectra, signal from annealed K2($^{D}$F)4E2 is more indicative of random coils. Unannealed K2($^{D}$F)4E2, however, demonstrates a minimum at ~ 197 nm and a maximum at ~ 216 nm, which is mirrored of the $\beta$-strand signal from the common $_{L}$-peptide.

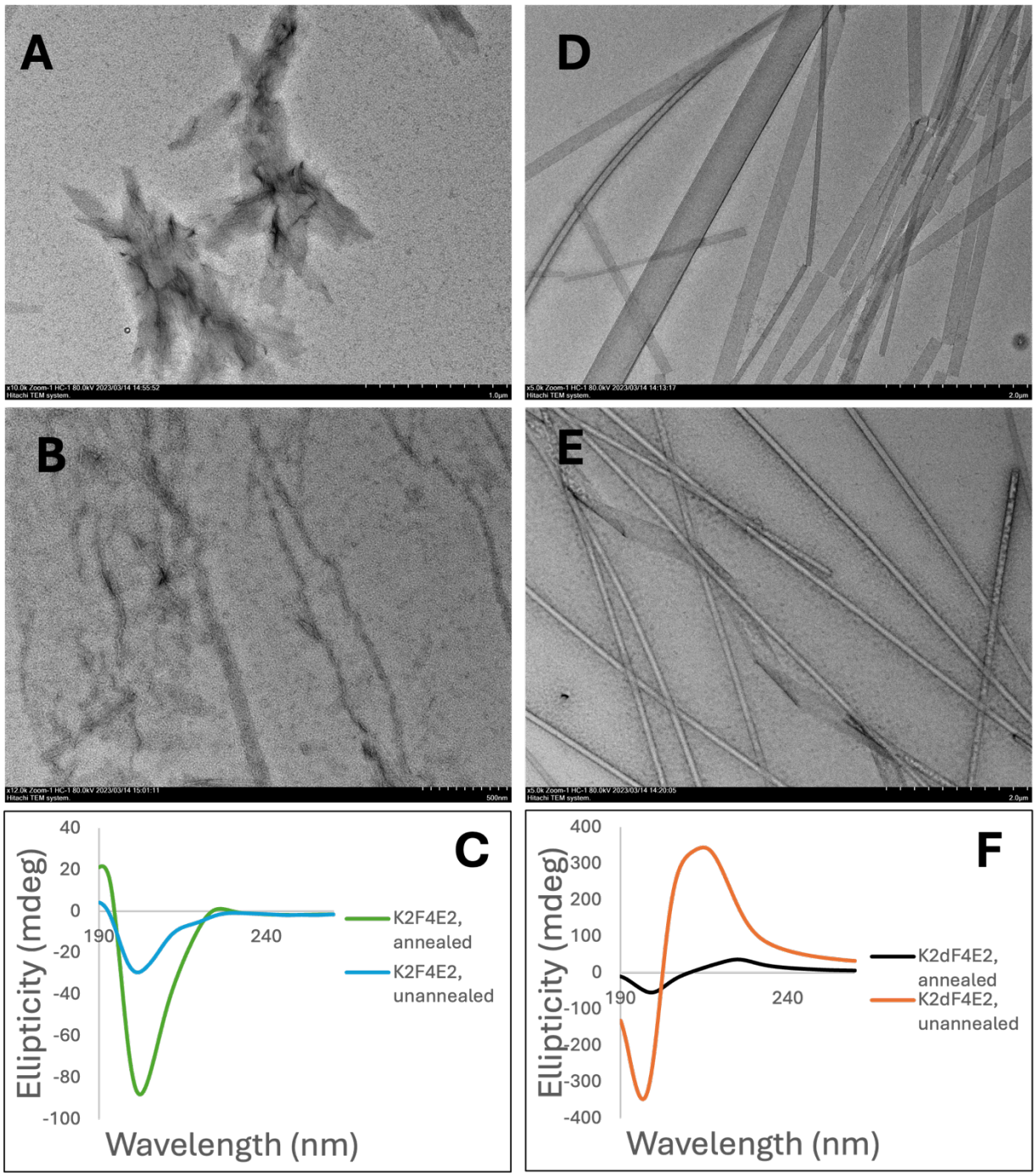


**Figure 2.** Assemblies of K2F4E2 and K2($^{D}$F)4E2 peptides in water after 1 week. (A) TEM images of annealed K2F4E2 sample; (B) TEM images of unannealed K2F4E2 sample; (C) CD spectra of K2F4E2 assemblies after 1 week. (D) TEM images of annealed K2($^{D}$F)4E2 sample; (E) TEM images of unannealed K2($^{D}$F)4E2 sample; (F) CD spectra of K2($^{D}$F)4E2 assemblies after 1 week.

The two peptides were later dissolved in hexafluoroisopropanol (HFIP), a solvent that is disruptive toward $\beta$-sheets, to preclude possible preassembled structures. HFIP-treated peptides were then frozen and lyophilized. Lyophilized materials were re-dissolved in water and allowed to assemble at RT (unannealed). The measured pH for K2F4E2 peptide solution decreases to 4.6, and pH for K2($^{D}$F)4E2 is 4.3. The HFIP-treated peptides both display stronger $\beta$-strand signal under CD measurements (Figure 3). The morphology of the assemblies also appears to be more uniform. Even though there are still not many assemblies found in the K2F4E2 sample, we could see that the peptide forms twisted filaments. The HFIP-treated K2($^{D}$F)4E2 still self-assembles into nanotubes but at a higher concentration compared to the sample without HFIP treatment.

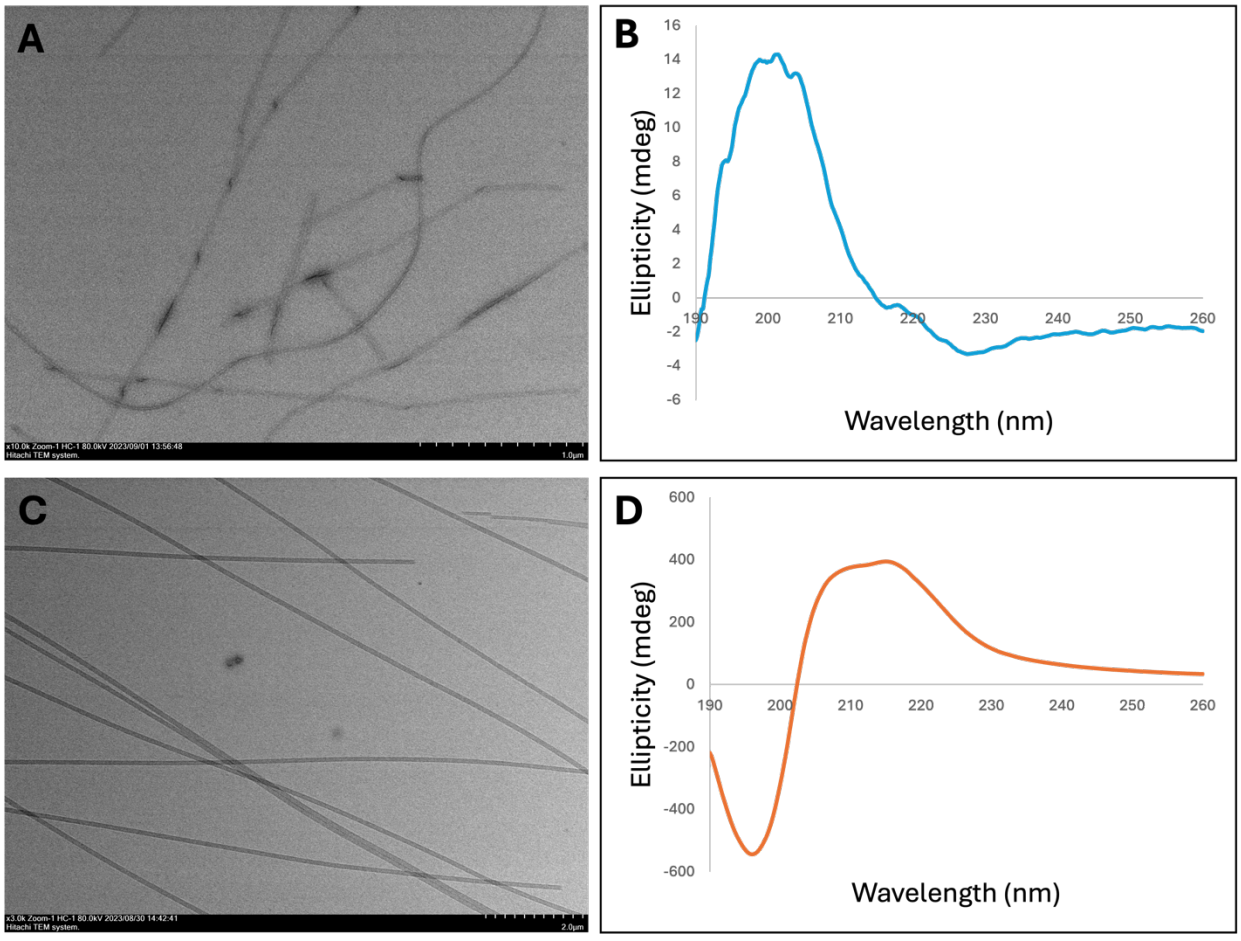

**Figure 3.** Assemblies from HFIP-treated K2F4E2 and K2($^{D}$F)4E2 peptides after 1 week. (A) TEM images of unannealed K2F4E2 assembly and (B) its corresponding CD spectrum; (C) TEM images of unannealed K2($^{D}$F)4E2 assembly and (D) its corresponding CD spectrum.

### 3.3. In-depth study on the assembly of K2($^{D}$F)4E2 in water

From our preliminary results, the most well-behaved assembly for further characterization is the HFIP-treated K2($^{D}$F)4E2 peptide being dissolved in water and unannealed. The process of assembly formation is then monitored over time with TEM (Figure 4). Only 5 minutes after the peptide being dissolved, there are already a lot of protofilaments in the background. Helical ribbons also start to form. 3 hours later, the ribbons continue to grow in length and some nanotubes can now be spotted. At the 6-hour time point, we can see that the edges of the ribbons are fusing. After 1 day, mostly long nanotubes are observed, although there are still ribbons and filaments in the background. The background essentially clears out at the 4-day time point, even though there are still some helical ribbons continuing to grow. After a week, almost no helices are detected, and the main species are nanotubes that are microns in length. The nanotubes remain intact for weeks. The average width of the matured nanotubes measured from negative stain TEM images is $72 \pm 6$ nm. It should be noted that how quickly the background filaments clear out and the ribbons grow into nanotubes also depend on the concentration of the assembly.

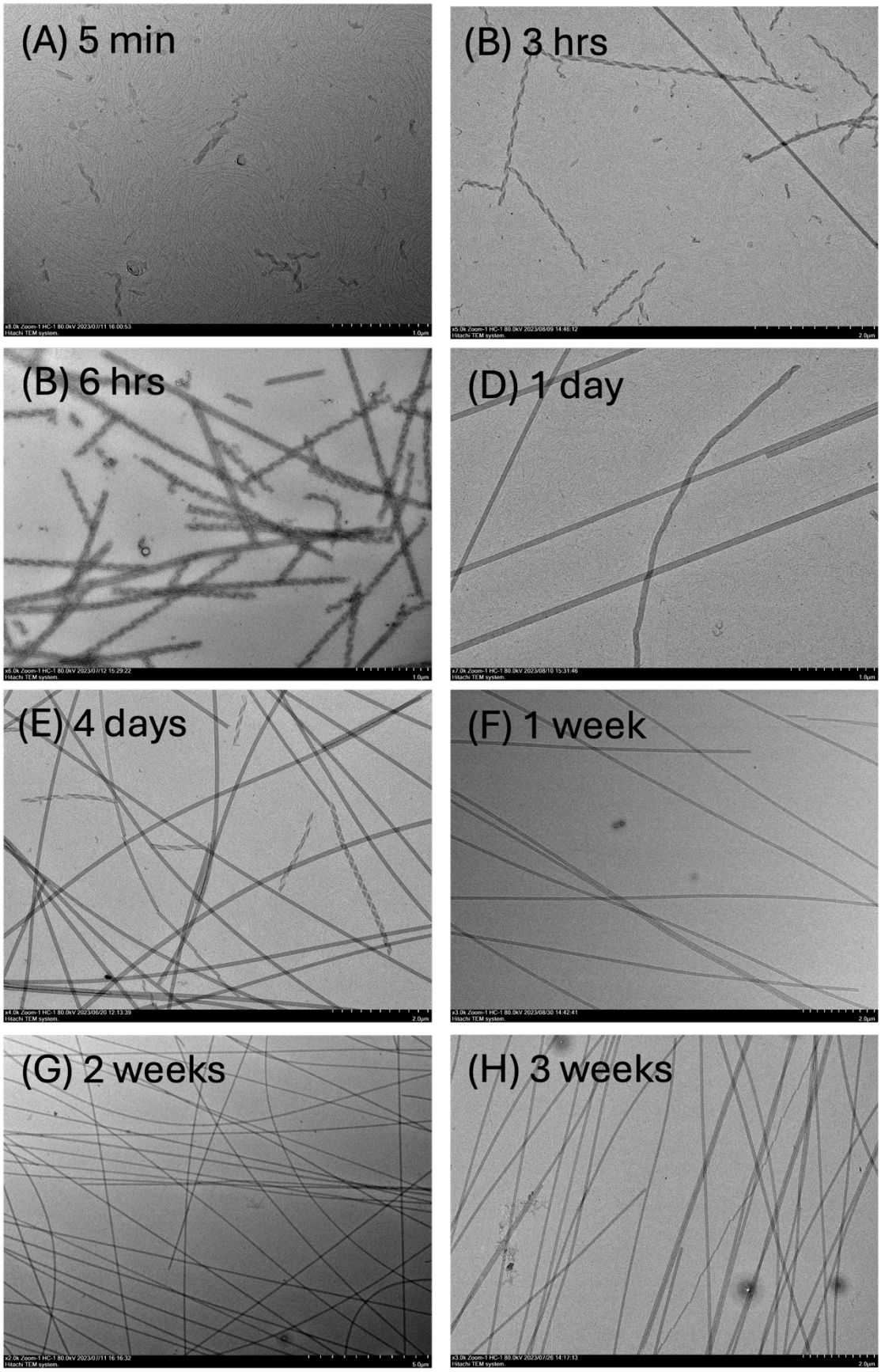
(A) 5 min
(B) 3 hrs
(B) 6 hrs
(D) 1 day
(E) 4 days
(F) 1 week
(G) 2 weeks
(H) 3 weeks

**Figure 4.** Morphology of K2($^{D}$F)4E2 peptide assembled in water monitored over time. TEM images of assemblies after (A) 5 minutes, (B) 3 hours, (C) 6 hours, (D) 1 day, (E) 4 days, (F) 1 week, (G) 2 weeks, (H) 3 weeks.

Time-point CD measurements also indicate a very robust growth of $\beta$-sheet content in the sample. The positive ellipticity at 217 nm, which is characteristic of $\beta$-strand from $_{D}$-peptide, develops almost immediately in the first hour and continues to grow steadily. (Figure 5, Figure S2). The signal growth rate in the first day is almost linear. It then slows down after day 1 and reaches a plateau at day 2 (Figure 5. Figure S3).

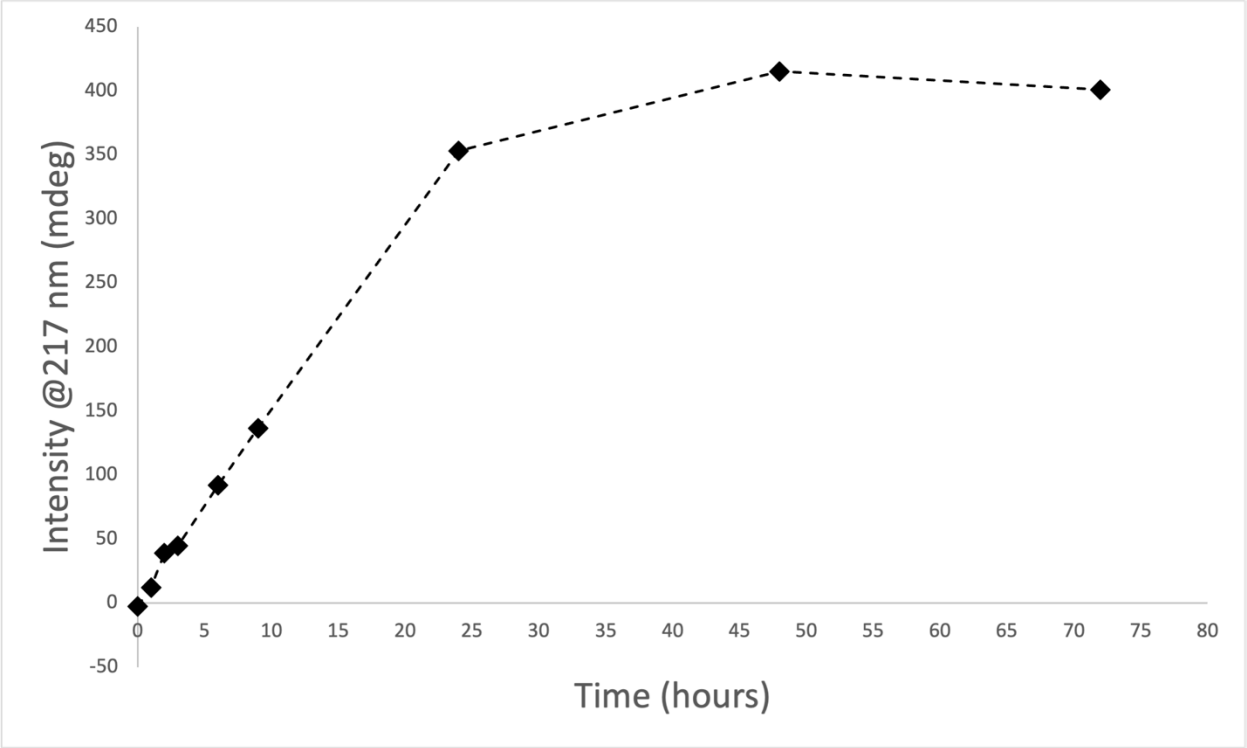


**Figure 5.** Ellipticities at 217 nm measured by CD spectroscopy for the assembly of HFIP-treated K2($^{D}$F)4E2 in water over time.

AFM analysis on the self-assembly of K2($^{D}$F)4E2 also reveals an evolution of the morphology from protofilaments to helical ribbons and eventually matured nanotubes (Figure 6). The theoretical length of K2($^{D}$F)4E2 when fully extended is 2.8 nm (3.5 Å / residue). The measured thickness for the filaments varies between 1 – 2 nm. The cross-section profiles of the ribbons show two different heights, ~2.7 nm and ~5.5 nm, which agree with the peptide monolayer and bilayer, respectively. Average height of the nanotubes is calculated to be 6.5 $\pm$ 1 nm, which is also close to the thickness of a peptide bilayer.

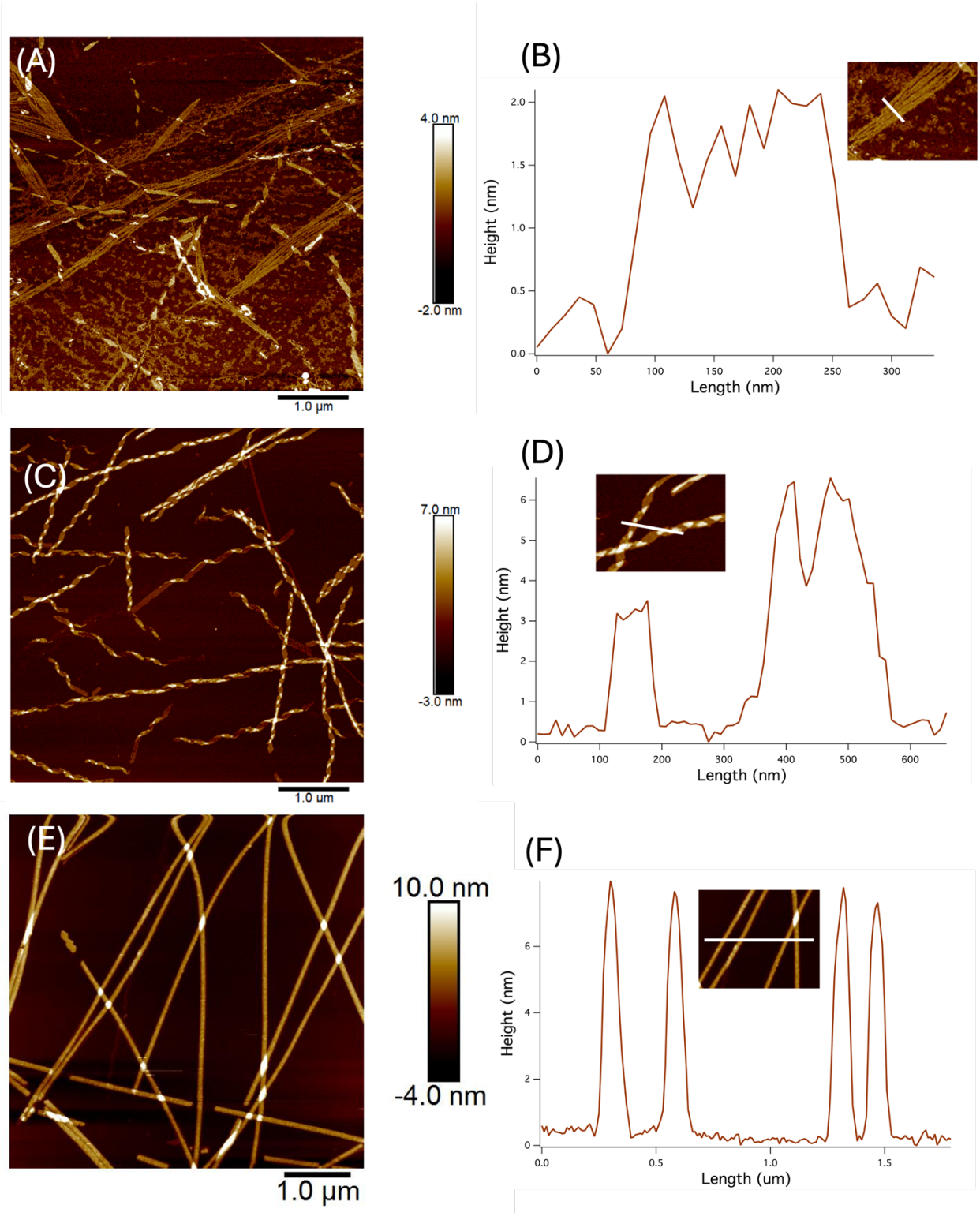
(A)
4.0 nm
-2.0 nm
1.0 µm
(B)
Height (nm)
Length (nm)
(C)
7.0 nm
-3.0 nm
1.0 µm
(D)
Height (nm)
Length (nm)
(E)
10.0 nm
-4.0 nm
1.0 µm
(F)
Height (nm)
Length (um)

**Figure 6.** AFM analysis on the self-assembly of K2($^{D}$F)4E2 indicating an evolution of morphology from (A) protofilaments to (C) helical ribbons to (E) matured nanotubes. Height traces across a section of each morphology are shown in (B), (D), and (F).

Synchrotron SAXS/WAXS analysis on the nanotubes results in a series of well-defined oscillations of intensity on the momentum transfer ($q$), which is consistent with formation of hollow cylinders (Figure 7). A Bragg diffraction peak is observed at a $q$ value of 1.33 $Å^{-1}$ ($d = 4.7$ Å), which corresponds to the $\beta$-sheet spacing. Another peak at a $q$ value of 0.51 $Å^{-1}$ ($d = 12.3$ Å) is also present that probably represents some higher-order arrangement. Analysis of the SAXS data yields a low-resolution model of a nanotube with a wall thickness of ~2.8 nm (theoretical length of the peptide) and an inner diameter of 31.0 $\pm$ 1.7 nm.

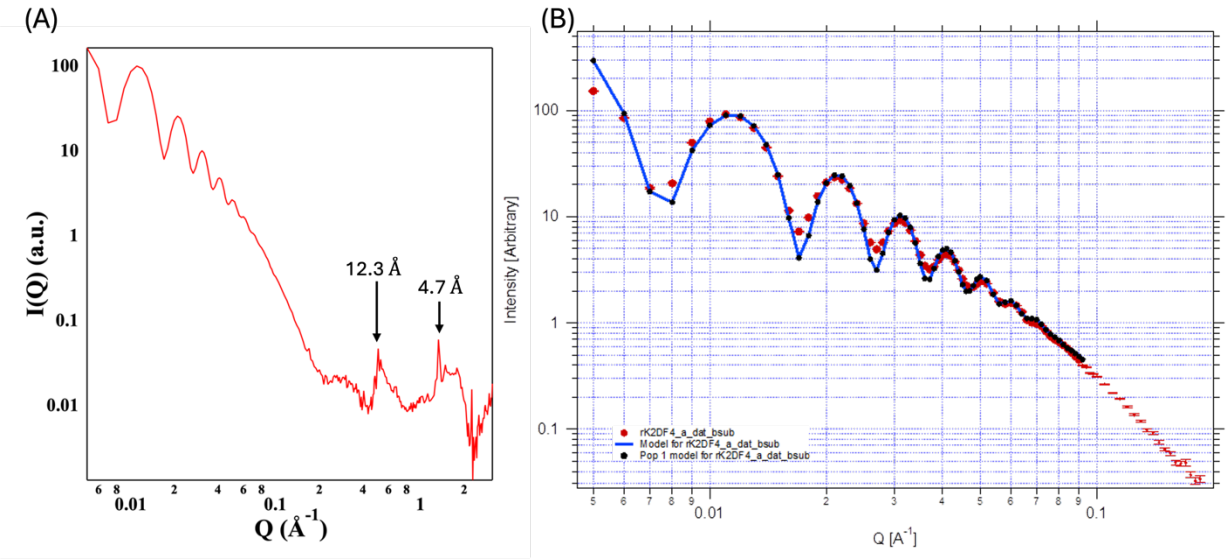


**Figure 7.** Synchrotron SAXS/WAXS scattering profile for the assembly of K2($^{D}$F)4E2 peptide. (A) Scattering curve with Bragg peaks at $q$ values of 0.51 $Å^{-1}$ ($d = 12.3$ Å) and 1.33 $Å^{-1}$ ($d = 4.7$ Å). (B) Comparison of the experimental SAXS scattering curve with a nanotube model with a wall thickness of 2.8 nm and inner diameter of 31.0 $\pm$ 1.7 nm.

Results from negative stain TEM and SAXS assume that the peptide assembles into nanotubes of homogenous size. However, initial cryo-EM imaging suggests the presence of nanotubes that subtly differ in apparent diameter (Figure 8). The three commonly measured widths are ~54 Å, 64 Å, and 72 Å, which correspond to nanotube diameters of ~34 nm, 41 nm, and 46 nm, respectively. Since polymorphism is a common problem in many peptide self-assemblies,[42] we will need to continue with two-dimensional (2D) classification and helical reconstruction to obtain a definitive answer for the structure(s) of the K2($^{D}$F)4E2 nanotubes.

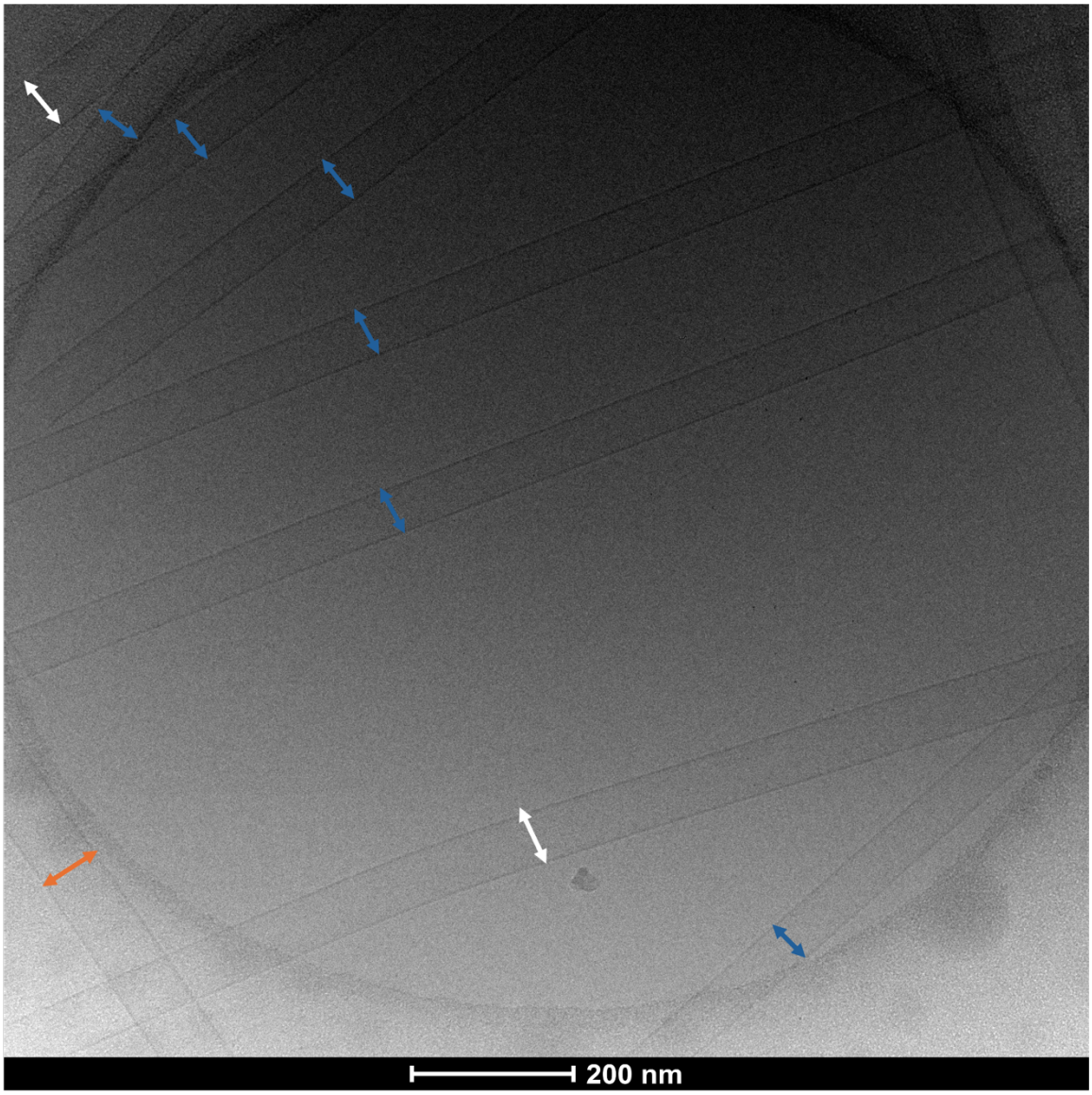

**Figure 8**. Cryo-electron micrograph of K2($^{D}$F)4E2 nanotubes of different diameters. The three different widths identified are ~54 Å (blue double arrows), 64 Å (white double arrows), and 72 Å (orange double arrow).

### 3.4. Discussion and future experiments

#### 3.4.1. Heterochirality promotes the self-assembly of BMPs

Our preliminary results agree with previous reports that block heterochiral peptides promoted the assembly structure.[37, 40] Having been assembled at the same concentration, K2F4E2 exhibits a significantly weaker $\beta$-strand signal as compared to K2F4W2. Moreover, while K2F4E2 forms only a few twisted filaments, K2($^{D}$F)4E2 assembles robustly into nanotubes of micron-length.

#### 3.4.2. A mechanistic explanation for formation of nanotubes from K2($^{D}$F)4E2 peptide

The morphological change from thin protofilaments to helical ribbons to nanotubes has been observed often for self-assembly processes involving chiral monomers.[43-47] Based on our current evidences, we propose a scheme for the formation of nanotubes from the self-assembly of K2($^{D}$F)4E2 peptide (Figure 9). Because of the salt bridges between terminal Lys and Glu residues, K2($^{D}$F)4E2 is expected to form antiparallel $\beta$-sheets. The lateral stacking of $\beta$-sheets can also be stabilized by these electrostatic interactions and by $\pi - \pi$ stacking between the Phe residues in the hydrophobic core. These laminated sheets then go through helical coiling to form ribbons that eventually fuse into nanotubes. Data from AFM measurements suggests that the wall thickness of

the nanotubes equals to a monolayer of fully extended peptide. The different populations of nanotube diameters as measured from cryo-EM micrographs may imply variations in the extent of lateral packing. This could also be the reason for fluctuations in the AFM height trace for the protofilaments. However, to obtain a definitive answer to this speculation, we will need to solve the structure of these nanotubes by cryo-EM.

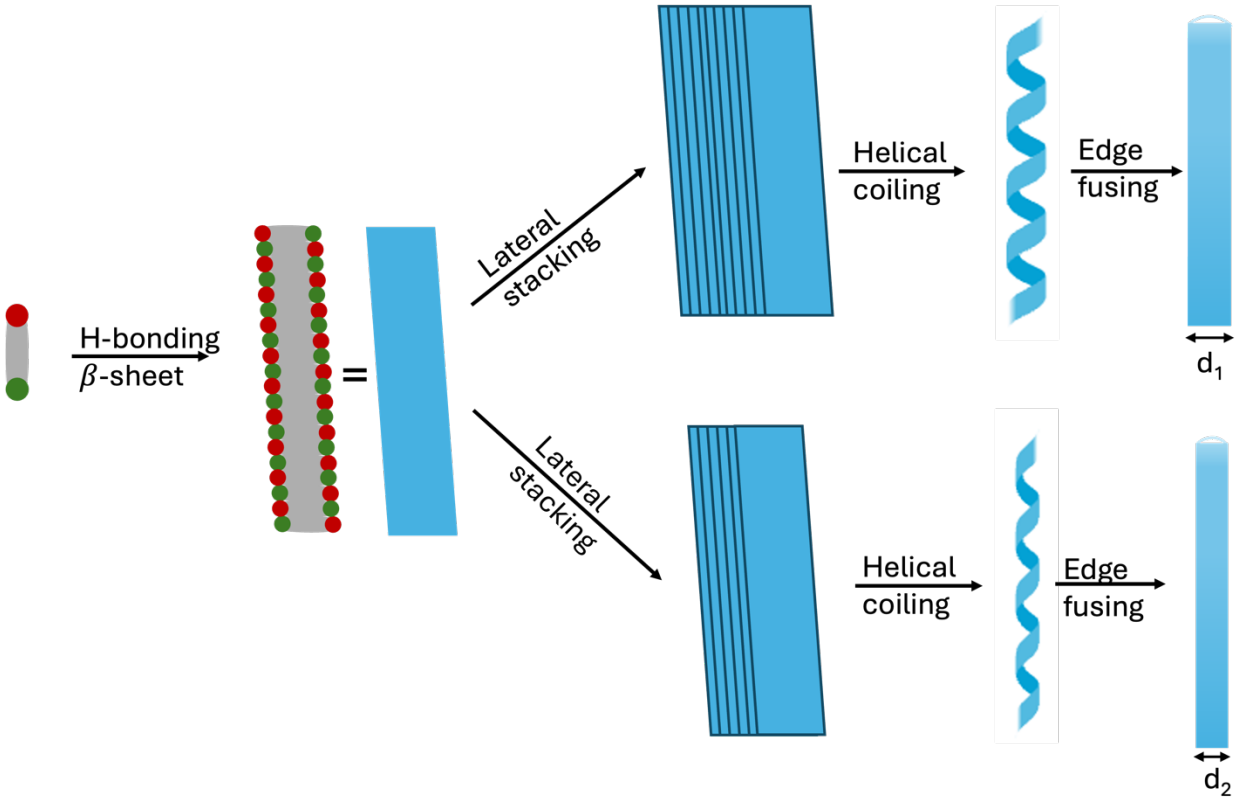


**Figure 9.** Proposed scheme for the formation of nanotubes from the self-assembly of K2($^{D}$F)4E2 peptide.

### 3.4.3. Future experiments

**Solving the structure of K2($^{D}$F)4E2 nanotubes by cryo-EM**

As mentioned above, our SAXS data can be fitted to a low-resolution model of a single population of nanotubes. However, initial cryo-EM experiment suggests the presence of nanotubes with subtle differences in diameter. Since polymorphism is a common problem in many peptide self-assembly, we will need to continue with cryo-EM analysis to obtain a definitive answer to the structure(s) of these K2($^{D}$F)4E2 nanotubes.

**Study of K2($^{D}$F)4E2 assembling behavior under different pH's**

Studies by Lynn and coworkers have reported on the assembly of a peptide sequence derived from the A$\beta$ peptide (Ac-KLVFFAE-$NH_2$) that was sensitive to environmental pH.[44, 46] At an acidic pH of 2, the negative charge of the terminal glutamic acid was neutralized and the peptide self-assembled into nanotubes. At a neutral pH of 6, Glu is charged, and formation of fibers was observed. The different protonation state of this Glu residue determined the formation of either antiparallel, in-register or antiparallel, out-of-register $\beta$-sheets.

In our case, the pH's measured for the assemblies of K2F4E2 and K2($^{D}$F)4E2 peptides (HFIP-treated samples) are 4.6 and 4.3, respectively. These values coincide with the pKa of the glutamic acid side chain (pKa = 4.3), so it is not straightforward to predict the protonation state of the two Glu residues. For future experiments, we can try to assemble the peptide in a more acidic pH and neutral pH to see if any morphological changes happen. We can also utilize isotope-edited infrared to probe the registry of our $\beta$-sheets when assembled under different pH conditions.

**Additional sequence designs to understand the effects of chirality on BMP self-assembly**

To have a more comprehensive understanding on the effect of $_{D}$-amino acid incorporation, we propose to study the assemblies of more sequences below (Table 1). First, we want to see whether the homochiral $_{D}$-analog would behave in a similar way as the homochiral $_{L}$-K2F4E2. In addition, we wonder if the block heterochiral substitution strategy still promotes self-assembly when we replace Lys and Glu with their enantiomers. Lastly, it would also be interesting to study the effects of other charged residues in place of Lys and Glu.

**Table 1.** Additional peptide sequences based on K2F4E2

| | |
|---|---|
| Homochiral | $_{D}$ – KKFFFFEE |
| Block heterochiral | $^{D}$(KKFF)FFEE |
| | KKFF$^{D}$(FFEE) |
| Different charged residues | RR$^{D}$(FFFF)EE |
| | KK$^{D}$(FFFF)DD |

### 3.5. Supplementary figures

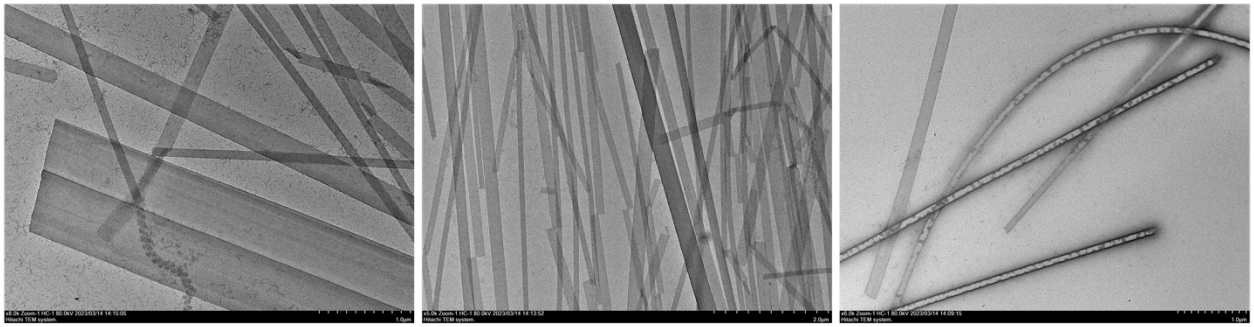

**Figure S1.** Additional TEM images from annealed K2($^{D}$F)4E2 assemblies after 1 week. Different morphologies including tapes of various widths and nanotubes are observed.

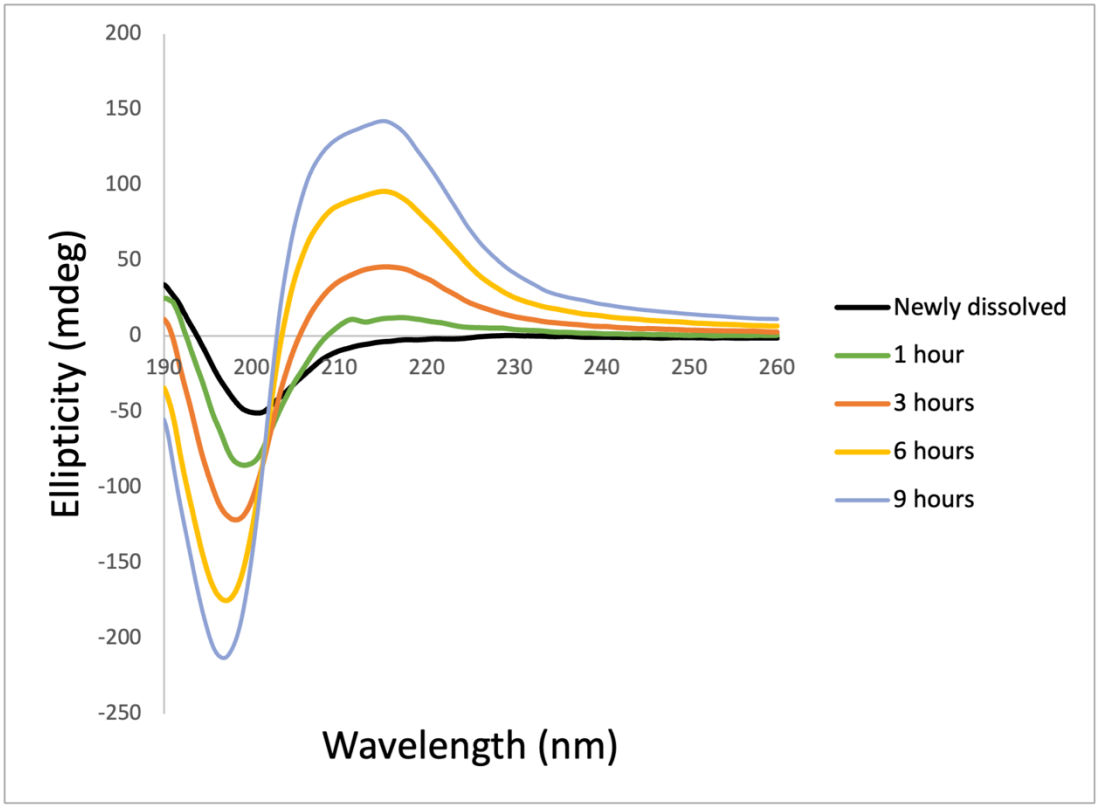


**Figure S2.** CD spectra of K2($^{D}$F)4E2 solution over the first 9 hours after experimental setup. A clear development of the $\beta$-strand signal for D-peptide can be observed.

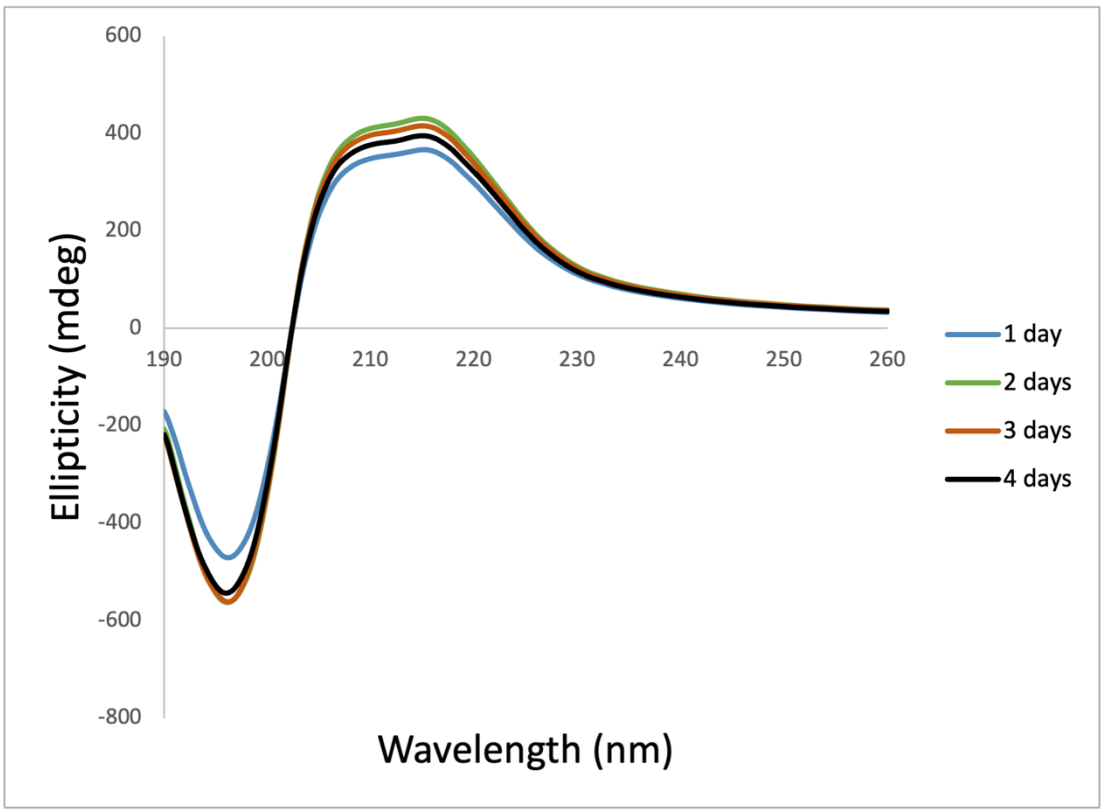


**Figure S3.** CD spectra of K2($^{D}$F)4E2 solution after 1-4 days. After a very robust growth within a day, the signal then reaches a plateau.

## 3.6. Experimental methods

### Peptide assembly experiments

Peptides were purchased commercially from GenScript USA, Inc. To prepare the peptide assemblies in water, samples were dissolved directly in HPLC-grade $H_2O$ to a final concentration of ~ 1mg/mL. For the assembly of HFIP-treated peptides, the peptides were dissolved in HFIP to (~ 1 mg/mL) and let sit at room temperature for 1 hour, followed by freezing and lyophilization of the solution. Lyophilized peptides were treated again with HFIP following the same procedure. To set up the assembly experiments, the double-lyophilized materials were then dissolved in HPLC-grade $H_2O$ (~1 mg/mL). Annealed samples were heated to 90 ℃ for 30 min, followed by slow cooling to 25 ℃. Unannealed samples were kept at RT.

### Circular dichroism spectropolarimetry

CD measurements were performed on a Jasco J-1500 CD spectropolarimeter using a 0.1-mm path length quartz cuvette from Hellma USA Inc. Three spectra were recorded and averaged in a wavelength range from 190 to 260 nm at a scanning rate of 100 nm/min and a bandwidth of 2 nm and a data pitch of 2 nm.

### Transmission electron microscopy

TEM specimens were prepared by depositing 4 $\mu$L of sample onto a 200-mesh carbon-coated copper grid from Electron Microscopy Services. After 90 s of incubation on the grid, excess liquid was wicked away, leaving a thin film of sample. Next, 4 $\mu$L of aqueous uranyl acetate stain

solution (1%) was deposited onto the thin film. After 60 s of staining, the remaining moisture was wicked away and the grids were air-dried. Electron micrographs were recorded on a Hitachi HT-7700 TEM with a tungsten filament and AMT CCD camera at an accelerating voltage of 80 kV.

**Atomic force microscopy**

AFM images were collected with a Bruker Multimode 8 atomic force microscope using peak force tapping mode in air. Images were obtained using SCANASYST-AIR probe from Bruker with a spring constant of 0.4 N/m and a resonance frequency of 70 kHz. To prepare the samples, 15 $\mu$L of the assembly solution were drop-casted onto freshly cleaved mica. After 5 min, the solution was wicked away and washed once with 30 $\mu$L of HPLC-grade $H_2O$.

**Small-angle/Wide-angle X-ray scattering measurements**

Synchrotron SAXS/WAXS measurements were performed at the LiX beamline of NSLS-II at Brookhaven National Laboratory. The X-ray wavelength was set at 0.826 Å. Two Pilatus3 detectors, 1M and 900K were employed for the simultaneous SAXS/WAXS measurements, covering the q range of 0.005-3.0 $Å^{-1}$. The solution samples were run with the house-built flow cell and the SAXS/WAXS data were processed with the beamline software.[48] The simulated SAXS curves were calculated using the program CRYSOL[49] with fitting to a model based on the form factor for a hollow cylindrical particle, as previously described for aqueous solutions of cross-$\beta$ nanotubes derived from self-assembly of the A$\beta$(16-22) peptide.[43] The wall thickness was set to 28 Å as a known parameter, which was similar to the estimated thickness of a monolayer of K2($^{D}$F)4E2.

**Cryogenic transmission electron microscopy**

3 $\mu$L of sample was pipetted onto a glow-discharged QuantiFoil grid 1.2 (300 mesh). A wait time of 5 s was set before blotting the grids. Grids were blotted for 3 s with no blot force and plunge-frozen in liquid ethane using a Vitrobot with the environmental chamber set at 100% humidity. Data were acquired on a Thermo Fisher Talos L120C 120 kV TEM equipped with a 4Kx4K Ceta detector. Images were collected at a calibrated pixel size of 3.2 Å.

### 3.7. References

(1) Jiang, T.; Xu, C.; Zuo, X.; Conticello, V. P. Structurally homogeneous nanosheets from self-assembly of a collagen-mimetic peptide. *Angew Chem Int Ed Engl* **2014**, *53* (32), 8367-8371. DOI: 10.1002/anie.201403780.

(2) Merg, A. D.; Touponse, G.; van Genderen, E.; Zuo, X.; Bazrafshan, A.; Blum, T.; Hughes, S.; Salaita, K.; Abrahams, J. P.; Conticello, V. P. 2D Crystal Engineering of Nanosheets Assembled from Helical Peptide Building Blocks. *Angew Chem Int Ed Engl* **2019**, *58* (38), 13507-13512. DOI: 10.1002/anie.201906214.

(3) Smith, A. M.; Williams, R. J.; Tang, C.; Coppo, P.; Collins, R. F.; Turner, M. L.; Saiani, A.; Ulijn, R. V. Fmoc-Diphenylalanine Self Assembles to a Hydrogel via a Novel Architecture Based on π–π Interlocked β-Sheets. *Advanced Materials* **2007**, *20* (1), 37-41. DOI: 10.1002/adma.200701221.

(4) Kuang, Y.; Xu, B. Disruption of the dynamics of microtubules and selective inhibition of glioblastoma cells by nanofibers of small hydrophobic molecules. *Angew Chem Int Ed Engl* **2013**, *52* (27), 6944-6948. DOI: 10.1002/anie.201302658 From NLM Medline.

(5) Melchionna, M. S., K. E.; Marchesan, S. The Unexpected Advantages of Using D-Amino Acids for Peptide Self- Assembly into Nanostructured Hydrogels for Medicine. *Curr Top Med Chem* **2016**, *16*, 2009-2018.

(6) Marchesan, S.; Easton, C. D.; Styan, K. E.; Waddington, L. J.; Kushkaki, F.; Goodall, L.; McLean, K. M.; Forsythe, J. S.; Hartley, P. G. Chirality effects at each amino acid position on tripeptide self-assembly into hydrogel biomaterials. *Nanoscale* **2014**, *6* (10), 5172-5180. DOI: 10.1039/c3nr06752a From NLM Medline.

(7) Luo, Z.; Wang, S.; Zhang, S. Fabrication of self-assembling D-form peptide nanofiber scaffold d-EAK16 for rapid hemostasis. *Biomaterials* **2011**, *32* (8), 2013-2020. DOI: 10.1016/j.biomaterials.2010.11.049 From NLM Medline.

(8) Garcia, A. M.; Iglesias, D.; Parisi, E.; Styan, K. E.; Waddington, L. J.; Deganutti, C.; De Zorzi, R.; Grassi, M.; Melchionna, M.; Vargiu, A. V.; et al. Chirality Effects on Peptide Self-Assembly Unraveled from Molecules to Materials. *Chem* **2018**, *4* (8), 1862-1876. DOI: 10.1016/j.chempr.2018.05.016.

(9) Clover, T. M.; O'Neill, C. L.; Appavu, R.; Lokhande, G.; Gaharwar, A. K.; Posey, A. E.; White, M. A.; Rudra, J. S. Self-Assembly of Block Heterochiral Peptides into Helical Tapes. *J Am Chem Soc* **2020**, *142* (47), 19809-19813. DOI: 10.1021/jacs.9b09755 From NLM Medline.

(10) Zheng, Y.; Mao, K.; Chen, S.; Zhu, X.; Jiang, M.; Wu, C. J.; Zhu, H. Identification of heterochirality-mediated stereochemical interactions in peptide architectures. *Colloids Surf B Biointerfaces* **2023**, *224*, 113200. DOI: 10.1016/j.colsurfb.2023.113200 From NLM Medline.

(11) Wang, F.; Gnewou, O.; Solemanifar, A.; Conticello, V. P.; Egelman, E. H. Cryo-EM of Helical Polymers. *Chem Rev* **2022**, *122* (17), 14055-14065. DOI: 10.1021/acs.chemrev.1c00753 From NLM Medline.

(12) Lu, K. J., J.; Thiyagarajan, P.; Conticello, V. P.; Lynn, D. G. Exploiting Amyloid Fibril Lamination for Nanotube Self-Assembly. *J Am Chem Soc* **2003**, *125*, 6931-6393.

(13) Mehta, A. K. C., W. S.; Liang, Y.; Dublin, S. N.; Dong, J.; Snyder, J. P.; Pingali, S. V.; Thiyagarajan, P.; Lynn, D. G. Facial Symmetry in Protein Self-Assembly. *J Am Chem Soc* **2008**, *130*, 9829-9835.

(14) Ziserman, L.; Lee, H. Y.; Raghavan, S. R.; Mor, A.; Danino, D. Unraveling the mechanism of nanotube formation by chiral self-assembly of amphiphiles. *J Am Chem Soc* **2011**, *133* (8), 2511-2517. DOI: 10.1021/ja107069f From NLM Medline.

(15) Hsieh, M. C.; Liang, C.; Mehta, A. K.; Lynn, D. G.; Grover, M. A. Multistep Conformation Selection in Amyloid Assembly. *J Am Chem Soc* **2017**, *139* (47), 17007-17010. DOI: 10.1021/jacs.7b09362 From NLM Medline.

(16) Zhao, Y.; Yang, W.; Wang, D.; Wang, J.; Li, Z.; Hu, X.; King, S.; Rogers, S.; Lu, J. R.; Xu, H. Controlling the Diameters of Nanotubes Self-Assembled from Designed Peptide Bolaphiles. *Small* **2018**, *14* (12), e1703216. DOI: 10.1002/smll.201703216 From NLM Medline.

(17) Yang, L.; Antonelli, S.; Chodankar, S.; Byrnes, J.; Lazo, E.; Qian, K. Solution scattering at the Life Science X-ray Scattering (LiX) beamline. *J Synchrotron Radiat* **2020**, *27* (Pt 3), 804-812. DOI: 10.1107/S1600577520002362 From NLM Medline.

(18) Svergun, D. B., C.; Koch, M. H. J. *CRYSOL* - a Program to Evaluate X-ray Solution Scattering of Biological Macromolecules from Atomic Coordinates. *J Appl Cryst* **1995**, *28*, 768-773.